

# On the Spectral Emission of Non-Maxwellian Plasmas

---

A THESIS SUBMITTED TO THE DEPARTMENT OF PHYSICS  
OF THE UNIVERSITY OF STRATHCLYDE  
FOR THE DEGREE OF DOCTOR OF PHILOSOPHY.

Paul Bryans

September 2005

# © Copyright 2005

The copyright of this thesis belongs to the author under the terms of the United Kingdom Copyright Acts as qualified by University of Strathclyde Regulation 3.49. Due acknowledgement must always be made of the use of any material contained in, or derived from, this thesis.

## **Abstract**

The emission from a finite-density plasma with a non-Maxwellian distribution of free-electron energies is discussed. Families of distribution functions are introduced as a method of measuring the degree of deviation from Maxwellian. It is shown how rate coefficients for electron-impact reactions must be reworked without the assumption of detailed balance at the rate coefficient level. Care is taken that the fundamental cross-section data are adequate for such a reworking, with particular emphasis on those reactions displaying resonant behaviour. With these modifications, it is demonstrated that much applied modelling and applied data can be continued almost transparently to the non-Maxwellian situation. Illustration of the effect of a non-Maxwellian distribution is provided for neutral helium emission lines and effective ionisation and recombination rate coefficients. It is also demonstrated, however, that in certain instances, the effects due to the distribution function cannot be distinguished from other causes such as density dependence.

# Contents

List of Figures	ii
Acknowledgements	iv
<b>1 Introduction</b>	<b>1</b>
<b>2 Maxwellian Atomic Modelling</b>	<b>10</b>
2.1 Reactions and Reaction Rates . . . . .	10
2.1.1 Excitation . . . . .	11
2.1.2 Ionisation . . . . .	19
2.1.3 Recombination . . . . .	24
2.2 Generalised Collisional-Radiative Modelling . . . . .	28
2.3 Dynamic Plasmas . . . . .	32
2.3.1 Li-Like Ions in the Solar Atmosphere . . . . .	33
2.3.2 Ultraviolet Explosive Events . . . . .	37
<b>3 Non-Maxwellian Modelling</b>	<b>46</b>
3.1 Distribution Functions . . . . .	46
3.1.1 Analytic Distributions . . . . .	47
3.1.2 Numerical Distributions . . . . .	51
3.2 Non-Maxwellian Rate Coefficients . . . . .	58
3.2.1 Collisional Excitation and De-Excitation . . . . .	58
3.2.2 Radiative Recombination . . . . .	68
3.2.3 Dielectronic Recombination . . . . .	76
3.2.4 Collisional Ionisation and Three-Body Recombination . . . . .	80
<b>4 Diagnostic Application</b>	<b>85</b>
4.1 Methodology . . . . .	85
4.2 Computational Implementation . . . . .	86
4.3 Illustrative Results . . . . .	89
<b>5 Conclusions and Future Work</b>	<b>98</b>
References	101

# List of Figures

1.1	Low-temperature discharge electron distribution . . . . .	2
1.2	Electron distribution in vicinity of comet Halley . . . . .	4
2.1	Collision strength of the $1s^2\ ^1S - 1s3s\ ^1S$ transition of $\text{He}^0$ . . . . .	13
2.2	Reduced electron-impact excitation collision strengths for the $1s^22s\ ^2S - 1s^22p\ ^2P$ transition in $\text{Ar}^{15+}$ . . . . .	14
2.3	Collision strength for the $1s^2\ ^1S - 1s3s\ ^1S$ transition of $\text{He}^0$ . . . . .	16
2.4	Energy scale lengths for averaged collision strength and Maxwellian distributions . . . . .	17
2.5	Energy scale lengths for averaged collision strength and $\kappa$ distributions . . . . .	18
2.6	CADW ionisation cross-sections for $\text{Kr}^{20+}$ . . . . .	21
2.7	Ionisation cross-section for $\text{C}^{2+}$ . . . . .	22
2.8	Contribution function for C IV 1548 Å, N v 1238 Å, O VI 1032 Å and Ne VIII 770 Å . . . . .	34
2.9	Ionisation coefficient of $\text{C}^{3+}$ . . . . .	35
2.10	Recombination coefficient of $\text{C}^{3+}$ . . . . .	35
2.11	Percentage difference in radiative loss function . . . . .	37
2.12	Time series image plots for O v 629 and N v 1238 . . . . .	40
2.13	N v 1238 Å line profile . . . . .	41
2.14	O v 629 Å line profile . . . . .	41
2.15	Contribution function of N v 1238 Å . . . . .	42
2.16	Contribution function of O v 629 Å . . . . .	42
2.17	Fractional abundance of $\text{O}^{4+}$ . . . . .	43
2.18	Light curves for N v 1238 and O v 629 . . . . .	45
3.1	$\kappa$ distribution . . . . .	48
3.2	Solar wind electron distribution . . . . .	49
3.3	Druyvesteyn distribution . . . . .	50
3.4	Electron velocity distribution as produced by Darwin PIC code . . . . .	55
3.5	Distribution function under influence of lower-hybrid wave field . . . . .	57
3.6	Effective collision strength for the $1s3s\ ^1S - 1s4p\ ^1P$ transition of $\text{He}^0$ . . . . .	61
3.7	Reduced collision strength for the $1s3s\ ^1S - 1s4p\ ^1P$ transition of $\text{He}^0$ . . . . .	62
3.8	Collision strength for the $1s3s\ ^1S - 1s4p\ ^1P$ transition of $\text{He}^0$ . . . . .	62
3.9	Reduced collision strength for the $1s^2\ ^1S - 1s2s\ ^3S$ transition of $\text{He}^0$ . . . . .	68
3.10	Effective collision strengths for the $1s^2\ ^1S - 1s2s\ ^3S$ transition of $\text{He}^0$ . . . . .	69
3.11	Reduced collision strength for the $1s2s\ ^3S - 1s2p\ ^3P$ transition of $\text{He}^0$ . . . . .	70

3.12	Effective collision strengths for the $1s2s\ ^3S - 1s2p\ ^3P$ transition of $\text{He}^0$ . . . . .	71
3.13	Reduced collision strength for the $1s2s\ ^3S - 1s3s\ ^3S$ transition of $\text{He}^0$	72
3.14	Effective collision strengths for the $1s2s\ ^3S - 1s3s\ ^3S$ transition of $\text{He}^0$	73
3.15	Reduced collision strength for the $1s2s\ ^3S - 1s2s\ ^1S$ transition of $\text{He}^0$	74
3.16	Effective collision strengths for the $1s2s\ ^3S - 1s2s\ ^1S$ transition of $\text{He}^0$	75
3.17	Radiative recombination coefficient for capture to $\text{He}^0$ ground state	77
3.18	Dielectronic recombination coefficient for capture to $1s2s\ ^1S$ state of $\text{He}^0$ . . . . .	80
3.19	Collisional ionisation rate coefficient from $1s2p\ ^3P$ state of $\text{He}^0$ . .	83
3.20	Three-body recombination rate coefficient to $1s2p\ ^3P$ state of $\text{He}^0$	84
4.1	Computational steps to create distribution-averaged collision strengths . . . . .	87
4.2	Variation of neutral helium populations with $\kappa$ . . . . .	91
4.3	Neutral helium line ratios as a function of electron temperature and $\kappa$ . . . . .	92
4.4	Neutral helium SCD as a function of non-Maxwellian parameter and electron temperature . . . . .	93
4.5	Neutral helium SCD as a function of non-Maxwellian parameter and electron density . . . . .	94
4.6	Neutral helium ACD as a function of non-Maxwellian parameter and electron temperature . . . . .	95
4.7	Neutral helium ACD as a function of non-Maxwellian parameter and electron density . . . . .	96

# Acknowledgements

Over the past few years I have had the pleasure of working with a large number of people, without whose help this work would not have been possible. Acknowledgement must first go to my supervisor, Hugh Summers. Dating back as far as an undergraduate summer placement, progressing to my final MSci project, and continuing through to the PhD, he has always been there to guide me in the right direction. I can only hope that some of his knowledge has rubbed off.

My second supervisor, Bob Bingham, is also thanked for his input to the project, particularly in the astrophysical application of the theoretical atomic physics and for giving me an education on the fundamental plasma physics relevant to this work. Most importantly, though, is his plethora of contacts around the globe, without which I would have been unable to visit the somewhat sunnier climes of California and New Mexico.

Perhaps the largest day-to-day help has come from Allan Whiteford. It is quite possible that my computer would have been thrown out the window (if our lab had any) a long time ago if it were not for his help in taming it. Help with science has also been always forthcoming from Allan and I have always looked up to him scientifically.

It has been a pleasure to work alongside Iain Paton and Martin Torney for the duration of this PhD, and I am glad that they are such good friends as well as colleagues. My many visits to the Rutherford Appleton Lab and JET would have been rather dull experiences were it not for the companionship of Iain and Martin as well as Allan and Adam Foster. While at Strathclyde, days have been broken up by, mostly nonsensical, conversations over coffee with Allan, Iain, Martin, and the quick wit of Cynthia Nam.

Nigel Badnell has provided a lot of help with fundamental collisional processes and computational matters. Martin O'Mullane, although based at JET, has also been ever willing in providing his assistance when required.

It has been my good fortune to have had the opportunity of visiting a number of places over the period of this work. At RAL I have had the pleasure of working with Richard Harrison, Dave Pike, Jeff Payne, Barry Kellett and Jim Lang.

I thank Kevin Quest for his hospitality during my time at the University of California in San Diego as well as his help with the running of PIC codes. I also had the pleasure of meeting Vitali Shapiro on this visit.

My time at the Armagh Observatory working with Gerry Doyle has led to a number of publications and the collaboration continues. I thank Gerry for the invite and for the introduction to the best Guinness vendors of the city.

Thanks must go to Stuart Loch for his help on collisional ionisation and the provision of data. Alessandro Lanzafame was also a great help in discussions for application to non-Maxwellian distributions in the solar atmosphere.

All the staff at the University of Strathclyde are thanked for their direct or indirect support, not least the Physics 5-a-side team including Rob Martin, Gordon Robb, John Jeffers, Neil Hunt, Craig Garvie, John Carey and Damia Gomila. Friday afternoons are always lightened with a bout of kicking the IT Crew, and I'll be forever glad not to be playing against Rob 'hard-but-fair' Martin.

The writing of the thesis itself was helped greatly by meticulous reading by Allan, Iain, Martin and Nigel. Their suggestions were all much appreciated. As deadlines grew closer in writing this thesis, I grew closer to accepting Allan's offer of '£250 per page'; any change in tone from page to page is purely stylistic, I might add.

I would like to thank my internal examiner, Alan Phelps, for his comments and helping me through the submission procedure. Particular thanks also goes to Helen Mason who took the time to read the thesis and travel up to Strathclyde to act as external examiner.

Although not any direct influence of the work itself, my parents and brother probably deserve most credit in helping me through the last few years. They have always taken an interest in my work and been supportive. In fact, it is likely that I'd be writing this a few months hence were it not for their efforts in waking and dragging me out the house each morning (although Jim deserves no mention on this score).

— Paul Bryans  
September 2005

# Chapter 1

## Introduction

The basis behind the majority of excited population and spectral emission models of ions in a plasma is the assumption that the free electrons possess an isotropic, Maxwellian distribution of speeds. This assumption is valid if energy redistribution through elastic collisions of electrons takes place on a sufficiently short time scale so as to negate slower energy selective losses to other plasma components or radiation. An examination of the lifetimes of the various states of atoms, ions and electrons in the plasma must be considered before an analysis based on such a ‘thermalised’ representation is justified (section 2.2). The work presented here is based on situations where inputs and outputs to the free-electron energy are of sufficient amplitude and frequency that thermalising collisions cannot return the distribution to Maxwellian form. The resultant non-Maxwellian electron distributions are not uncommon in both laboratory and astrophysical plasmas.

It is well known that low-density, weakly-ionised technical plasmas, such as those produced in radio frequency or microwave plasma reactors, often exhibit markedly non-Maxwellian electron distributions (Nighan, 1970; Loureiro and Ferreira, 1986, 1989; Moisan *et al.* 1991). Many authors have attempted to calculate precisely the nature of these distributions for electrically excited molecular (primarily N<sub>2</sub>, CO and CO<sub>2</sub>) and noble gases (Behringer and Fantz, 1994; Behringer and Fantz, 2000; Gudmundsson, 2001). However, most laboratory experiments do not allow a direct measurement of the distribution function; a numerical solution of the Boltzmann equation using electron-molecule cross-sections being generally used instead. The findings have shown that the deviation from Maxwellian can be such that using a Maxwellian function for plasma modelling is not a justified approximation.

Behringer and Fantz (1994), reporting on low-density glow discharge plasmas, attempt to represent the electron distribution as an analytical function

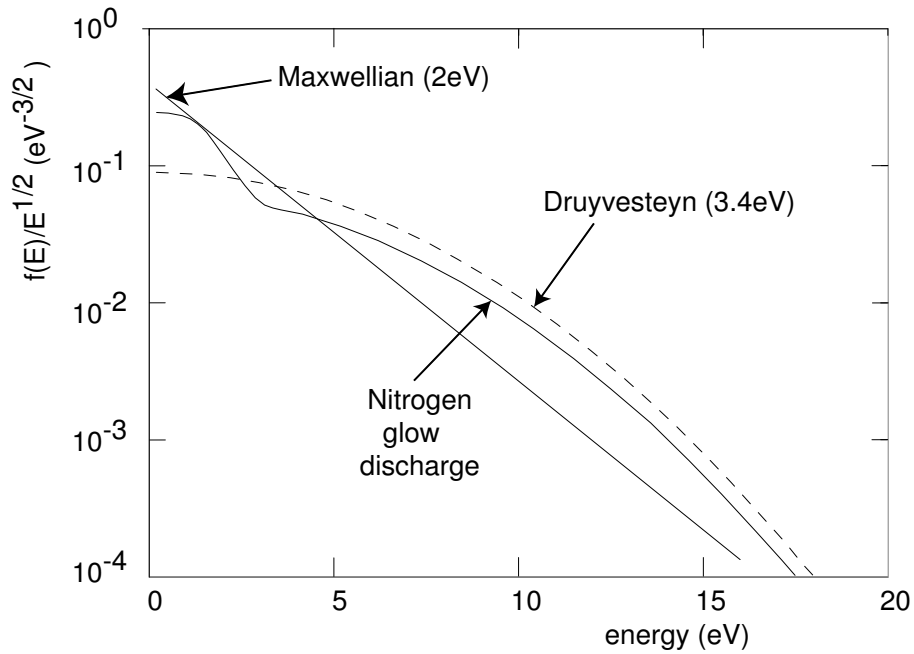


Figure 1.1: Electron distribution functions typical of low-temperature discharges. The Maxwell and Druyvesteyn patterns are shown and a modelled case for a nitrogen plasma. The kink at  $\sim 0.8$  eV reflects the energy loss to vibrational excitation of the molecule (Behringer and Fantz, 1994).

using as few parameters as possible. The fact that the electron distribution, in pure  $N_2$  and  $N_2$  mixed with noble gas plasmas, differs most significantly from a Maxwellian in the high-energy region of the distribution (see figure 1.1) led to these authors introducing an analytical formula based on the Druyvesteyn distribution (Druyvesteyn, 1930), which falls off faster than the Maxwellian in the high energy range. The so called ‘generalised Druyvesteyn’, thus introduced, is discussed further in section 3.1.1.2.

X-ray emission from the atmospheres of Mars and Venus, as observed by the Chandra spacecraft (Dennerl, 2002 and Dennerl *et al.* 2002), is believed to be the result of the interaction between the solar wind and the planetary ionosphere producing energetic electrons. Distributions showing a hot electron component are typical of the mantle region where this interaction takes place (Spenner *et al.* 1980). It has been shown through theory and simulation (Sagdeev *et al.* 1990; Quest *et al.* 1997; Dobé *et al.* 1999; etc.) that the counter-streaming of the shocked solar wind plasma and the planetary ions can lead to the modified two-stream instability (McBride *et al.* 1972), generating waves with frequencies a few times above the lower hybrid frequency, provoking significant electron acceleration. These energetic electrons can produce x-ray emission following their collision with outflowing neutral gas and heavy ions in the ionosphere (Bingham *et al.* 1997; Shapiro *et al.* 1999).

Such energisation of electrons, leading to distributions with an extended tail in comparison to the Maxwellian, has wider occurrence in the astrophysical domain. Dawson *et al.* (1997) postulate x-ray emission from comets by a similar mechanism to that pertaining to the solar wind-planetary atmosphere interaction. In this case, the solar wind interaction with the cometary plasma energises electrons and the development of a non-Maxwellian tail to the distribution function is believed to form. Measurements of the electron distribution of comet Halley by the Vega spacecraft show this to be so (Gringauz and Verigin, 1990; figure 1.2). It is suggested (Dawson *et al.* 1997; Bingham *et al.* 1997; Shapiro *et al.* 1998) that soft x-ray bremsstrahlung and highly ionised ion line emission is caused by these energised electrons. It is to be noted, though, that the bremsstrahlung part of the soft x-ray spectrum is not yet unambiguously resolved by spacecraft such as Chandra and that an alternative charge exchange process is widely believed to be the primary source of cometary x-rays (Cravens, 1997; Häberli *et al.* 1997; Wegmann *et al.* 1998; etc.). A similar mechanism, but correspondingly more energetic, is thought to occur in supernova remnants as the expanding shell meets gas clouds from earlier mass releases from the parent star (Spicer *et al.* 1990;

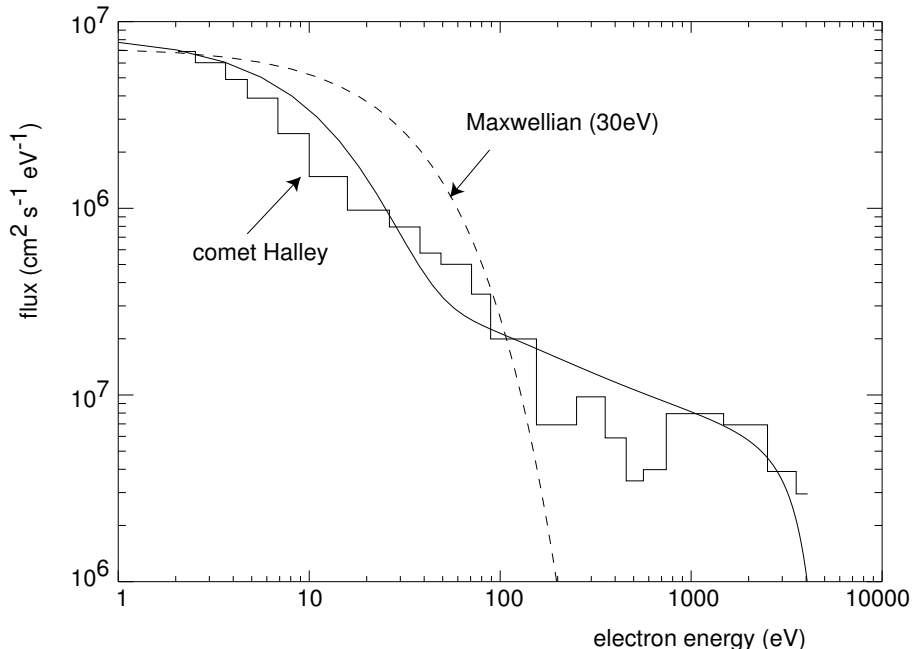


Figure 1.2: Electron flux measurements in the vicinity of comet Halley by the VEGA 1, 2 spacecraft (Gringauz and Verigin, 1990). The measurements suggest the development of a non-Maxwellian tail parallel to the magnetic field of an initial Maxwellian electron distribution function in the presence of a lower-hybrid wave field. Such fields are expected to be energised by the interaction of the solar wind with an ebullient cometary plasma and lead to x-ray emission. For comparison, a Maxwellian (dashed line) at 30 eV and a synthesised distribution (solid line) are shown. The latter comprises a Maxwellian at 10 eV combined with a 70 eV Maxwellian Landau damped with a Gaussian wave of resonant velocity 4 times the thermal speed, and half-width of twice the thermal speed (see section 3.1.2).

Hoshino *et al.* 1992; Laming, 2001; Bleeker *et al.* 2001; Bingham *et al.* 2004).

The solar atmosphere has been the subject of a large number of works on non-Maxwellian electron distributions, in particular those displaying suprathermal tails. An area where non-Maxwellian distributions have received significant attention is in the heating of the coronal plasma. Why the solar corona should be orders of magnitude hotter than the underlying chromosphere is a subject that, while investigated for decades, remains unanswered. The usual explanation is due to mechanical or wave heating (Narain and Ulmschneider, 1990; Browning, 1991; Zirker, 1993; Porter *et al.* 1994a, 1994b; Tu and Marsch, 1997) but it has been argued by Scudder (1992a, 1992b) that these mechanisms are unnecessary and the high coronal temperatures can be explained in terms of non-Maxwellian

electron distributions in the transition region.

This ‘velocity filtration’ coronal heating model postulates that the base of the corona has free electrons with a non-Maxwellian distribution. Higher regions then become hotter because the high-energy electrons can overcome gravity and enter the corona.

The model of Scudder (1992a, 1992b) does not address the question of how non-Maxwellian distributions of electrons form. Viñas *et al.* (2000) present such a mechanism based on Vlasov and PIC (particle-in-cell) numerical simulations. Their work provides evidence to support the formation and maintenance of non-Maxwellian distributions, with the energy coming from the magnetic field.

Anderson *et al.* (1996) test the velocity filtration coronal heating model by calculating predicted UV emission line intensities from the transition region, using the  $\kappa$  (‘kappa’) distribution (Vasyliunas, 1968) and Maxwellian superpositions to simulate the distribution function. They concluded that this heating does not exactly match the emission measure observations, but acknowledge that their model is incomplete.

Scudder (1994) points out that the velocity filtration model should result in the solar wind possessing a non-Maxwellian distribution of electrons and Maksimovic *et al.* (1997) have fitted  $\kappa$  distributions to measurements of the solar wind by Ulysses (Bame *et al.* 1992). They found that the fast solar wind can be fitted with  $\kappa$  in the range 2–5 (see section 3.1.1.1 for more on the  $\kappa$  distribution and the meaning of the  $\kappa$  parameter), while the slow solar wind is closer to Maxwellian.

Atomic modelling of non-Maxwellian plasmas is not without precedent. Recent work by Smith (2003) attempts to explain anomalous helium resonance line intensities in the solar transition region by considering the effect of non-Maxwellian distributions. The distributions are approximated as locally Maxwellian below a certain velocity, and with a power-law decline above this velocity. Excitation and ionisation rates are calculated based on these distributions, leading to estimates of the line intensities of interest. The paper does contain problems in that modified distributions are not re-normalised, so the handling is not generic. Also, the calculation of rate coefficients is based on analytic expressions for the cross-sections which are drawn from dated sources, primarily Mihalas and Stone (1968). Evaluation of the integrals based on more recent data is preferable.

Further examples of atomic modelling of the solar atmosphere with non-Maxwellian electron distributions include the work of MacNeice *et al.* (1991). These authors calculated the distribution function through a solution of the

Fokker-Planck equation applied to loops in the corona. Perhaps surprisingly, the results show no significant differences to the ionisation balance of O, Ne or Si in comparison with those calculated in the Maxwellian regime. This differs from the preponderance of results in the literature; in particular, a substantial amount of work has been published by Dzifčáková (1992, 2002) and Dzifčáková and Kulinová (2003) on the effects of non-Maxwellian distributions on coronal elements. Dzifčáková (1992) calculated the ionisation balance of Fe under the influence of the  $\kappa$  distribution and found considerable differences in the fractions of  $\text{Fe}^{15+}$ – $\text{Fe}^{17+}$  in the temperature range  $10^5$ – $10^8$  K with  $\kappa = 2$ . Updated values for these calculations can be found in Dzifčáková (2002). A similar analysis has been carried out for C and O (Dzifčáková and Kulinová, 2003), the ionisation peaks of these ions being found to be wider and the level populations lower (as is verified in the present work in section 4.3) for the  $\kappa$  distribution compared to Maxwellian.

Other authors (Owocki and Scudder, 1983; Doyle *et al.* 2003) have calculated the effect of non-Maxwellian electrons on the ionisation balance of coronal elements. Owocki and Scudder (1983), using the  $\kappa$  distribution, found that the high-energy tail slightly decreases the degree of ionisation of  $\text{Fe}^{11+}$  to  $\text{Fe}^{12+}$ , but can significantly increase the ionisation of  $\text{O}^{6+}$  to  $\text{O}^{7+}$ . Doyle *et al.* (2003) also used the  $\kappa$  distribution and found that the temperature at which Fe IX lines are produced in detectable quantities is lowered from  $\sim 800,000$  K to  $\sim 300,000$  K with  $\kappa = 2$ –10.

The objective of the present work is to provide a first entirely general analysis of the atomic processes pertaining to the isotropic, non-Maxwellian plasma. One must first consider the distribution functions themselves; the approach is to introduce analytic families that correspond to experimentally observed distributions. The  $\kappa$  (Vasyliunas, 1968) and generalised Druyvesteyn (Druyvesteyn, 1930) are two such families that match closely with common non-Maxwellian distributions. The  $\kappa$  distribution is a representation, often encountered in astrophysics, of a distribution with an enhanced high-energy tail compared to the Maxwellian. Contrastingly, the Druyvesteyn is an analytic form with a depleted high-energy part of the distribution. These functions are simplified representations of the actual distributions in plasmas. So, in addition, numerically tabulated distributions from sophisticated plasma modelling calculations are considered in this thesis, where the analytic functions, or a superposition of such, are inadequate to describe the plasma in question. By this means, it is sought to enable the exploration of analytic paradigms in a pedagogical manner as well as the pursuit of

high precision handling for diagnostic application in plasmas. These distributions are described further in section 3.1.2.

An area where this work is especially rigorous, and where previous studies have lacked such careful examination, is in the quadrature of the reaction cross-section with the distribution function to form the reaction rate. The cross-sections used are, where available, from the most accurate sources to date. Extensive use is made of  $R$ -matrix calculations (Burke and Robb, 1975) and there is a systematic revertive procedure whereby the next most accurate data is used if necessary. This is in marked contrast to the work of other authors (see e.g. Owocki and Scudder, 1983; Anderson *et al.* 1996; Smith, 2003) where common practice has been to use simplified analytic expressions to represent the cross-section and so simplify the evaluation of the quadratures. Using more accurate, numerically tabulated, cross-sections inhibits non-numerical solution of the integrals, so a careful numerical quadrature approach is required.

In this context, there is an important issue. Collision strengths obtained from simple analytic or parametric formulae, non-resonant calculations and from data assessment are smooth functions of energy and the forming of rate coefficients is a further smoothing procedure. It is tacitly assumed that the tabulated collision strength can sustain quadrature over an arbitrary electron distribution function. However, more precise resonance-including calculations, e.g. the  $R$ -matrix method, indicate that for incident electron energies between the excitation and ionisation thresholds, the true collision strength shows many fine, highly-peaked, resonance features. Even for a neutral target, the typical collision strength can show detailed structure (see figure 2.1 of section 2.1.1). Thus, many collision strengths available in the public domain are (unspecified) averages and therefore cannot necessarily support arbitrary non-Maxwellian averaging. It seems, therefore, that  $R$ -matrix and similar resonance-including collision strengths must be the starting point for computing rate coefficients in the general case. On the other hand, the exact delimiting of a collision strength may require tabulation at a very large number of data values — prohibitive for convenient utilisation within database structures. For example, a recent  $R$ -matrix calculation of the collision strength for the transition  $1s^2\ ^1S - 1s2p\ ^3P$  in neutral helium used  $\sim 37,000$  data points to resolve detailed resonance structure over a 2 Ryd energy range (Ballance, 2003). A more manageable tabulation of the collision strength would require a smoothing of the data. Care must then be taken that the reduction in tabulation does not cause the forming of a rate coefficient, by quadrature with the distribution function, to be unacceptable in terms of the relative variability of

the collision strength and the distribution function. A more detailed discussion of these concerns can be found in section 2.1.1 and Paton (2005). In any case, beyond the resonance region, the electron impact excitation reaction rate calculations must take into account the transition type (see Burgess and Tully, 1992) and use the appropriate high-energy limiting behaviour of Bethe (1930), Born (Burgess and Tully, 1978) and Ochkur (1964) for non-Maxwellian modelling.

A complete re-working of each of the fundamental electron-driven atomic processes is undertaken. By returning to the axiomatic relations governing the excitation and de-excitation, ionisation and recombination reactions of electron-ion systems, and parallelling the prescription leading to Maxwellian rate coefficients, rate coefficients for a general distribution function are delivered. The derived use of these coefficients is by propagation through the generalised collisional-radiative (GCR) model (Bates *et al.* 1962; Summers and Hooper, 1983; Summers *et al.* 2005) to achieve useful derived atomic data for plasma analysis. Such modelling must then be modified to accommodate non-Maxwellian parameters, although calculation of the inputs is with a view to minimising the required alterations. A major theme of the work presented here is the ease of use to the applied modeller. The practical implementation of the methods described here is part of the Atomic Data and Analysis Structure (ADAS; Summers, 1993, 2004). Existing ADAS codes generate rate coefficients for atomic processes in the Maxwellian framework and proceed from there to the production of derived atomic data such as effective ionisation and recombination coefficients, ionisation stage fractional abundances and photon emissivity coefficients. This work looks to keep the running of such codes virtually unaltered, achieved by defining the non-Maxwellian rate coefficients in such a way that they are read in to the processing codes allowing calculations to proceed as they would in the Maxwellian case.

Extension of the work to experimental applicability is examined from two different starting points. Considering the case where the electron distribution has been arrived at through measurement, one may use all of the analysis techniques previously available via ADAS in the Maxwellian context for the distribution in question by beginning from the re-evaluated reaction rate coefficients and proceeding through the GCR modelling almost transparently. Perhaps the most useful application of such calculations would be the comparison with Maxwellian conditions. An example of such a comparison is detailed in section 4.3.

However, it is unusual that the precise nature of the electron distribution is known, constraining the use of the above method. Some intimation of the form of the distribution may not be out of reach — for instance, the electron distribution

of the solar wind has been measured by Bryant (1996) and found to coincide with the  $\kappa$  distribution, although the value of the  $\kappa$  parameter is variable and dependent on solar conditions. Assuming there is some means of determining the electron temperature and density of the plasma, it is possible to determine a ‘non-Maxwellian parameter’ by analysis of line ratios, in a manner similar to the standard temperature and density diagnostic line ratios. Illustration of this can be found in section 4.3.

It is of course recognised that non-Maxwellian effects can be difficult to identify unambiguously in plasma diagnostic analysis. Effective temperature and non-Maxwellian parameters may be only weakly orthogonal. Also, aspects of generalised collisional-radiative modelling, such as finite density shifts of ionisation balance and the role of populated metastables in dynamic plasma evolution, are not always included in analysis and so mis-interpretation is possible. In this thesis, some studies are included of these GCR effects in a pure Maxwellian context for completeness and as a point of commencement.

In summary, the thesis encompasses the following: review of laboratory and astrophysical plasmas, identifying which type of non-Maxwellian distributions are important and, for the purposes of atomic modelling, dividing these into families of distributions; recalculation of the familiar Maxwellian electron-driven reaction rates for the non-Maxwellian distribution and their entry into the equations of statistical balance for the excited populations of an ion within the GCR context; and exploration of how the derived atomic data can then be used as a diagnostic tool by the spectroscopic plasma analyst.

# Chapter 2

## Maxwellian Atomic Modelling

In the advance towards non-Maxwellian modelling, it is important to clarify some issues in Maxwellian modelling. In particular, a review of the reaction rate coefficients and the generalised collisional-radiative (GCR) framework for their conversion into derived quantities for spectral analysis and plasma modelling is presented here with an emphasis given to aspects most affected by non-Maxwellian distributions (i.e. resonant processes). GCR modelling has, until now, only been carried out for Maxwellian electron distributions; it is the norm for light elements in the fusion plasma context, but is less widely used in astrophysical plasma studies. GCR modelling gives substantial attention to dynamic plasmas and the role of metastables in them. Also, it addresses fully the role of re-distributive collisions in finite-density plasmas and the modification of effective reaction coefficients. These effects can produce consequences similar to those of non-Maxwellians. So, this chapter also includes some specific application studies in the Maxwellian environment, in which dynamics and finite-density are important. This is essential to allow a safe progression on to non-Maxwellian analysis. The value of the work of this thesis is only realisable by comparison of the experimentally measurable quantities of the non-Maxwellian plasma to those of the Maxwellian plasma.

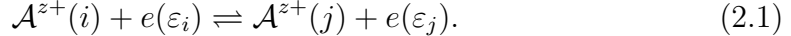
### 2.1 Reactions and Reaction Rates

The first examination is of the principal reactions and their characteristics in a Maxwellian plasma. It is necessary to understand the conditions under which approximating the free-electron distribution to a Maxwellian is justified and when not in the formation of reaction rates. The section introduces the reactions that are important in determining the emission from the plasma. Since it is deviations to the free-electron distribution that are considered here, electron-driven

processes are those that are examined. The cross-sections describing these reactions are given and there is a discussion of the methods used in calculating them. The emphasis is on the details that are important for non-Maxwellian modelling. Aspects of the fundamental data, in particular, resonance structure and smoothness, that may not be critical when analysing a Maxwellian plasma, warrant further attention in the non-Maxwellian environment.

### 2.1.1 Excitation

Consider the electron-impact excitation and de-excitation of the  $z$ -times ionised ion  $\mathcal{A}^{z+}$  between lower state  $i$  and upper state  $j$ ,



The excitation energy is  $\Delta E_{ij} = \varepsilon_i - \varepsilon_j$ , where  $\varepsilon_i$  the free-electron energy with the ion in the lower state  $i$  and  $\varepsilon_j$  the free-electron energy with the ion in the upper state  $j$ . The reaction is described by an excitation cross-section,  $\sigma_{i \rightarrow j}(\varepsilon_i)$ , and a de-excitation cross-section,  $\sigma_{j \rightarrow i}(\varepsilon_j)$ , although in practice it is most convenient to work in terms of the collision strength,  $\Omega_{ij}$ , which is dimensionless and more slowly-varying with energy than the cross-section. In addition, by introducing the statistical weight,  $\omega$ , in the definition, one ensures the collision strength to be symmetric between final and initial states. This definition, introduced by Hebb and Menzel (1940), is expressed in terms of the cross-sections as,

$$\Omega_{ij}(\varepsilon) = \omega_i \left( \frac{\varepsilon_i}{I_H} \right) \left( \frac{\sigma_{i \rightarrow j}(\varepsilon_i)}{\pi a_0^2} \right) = \omega_j \left( \frac{\varepsilon_j}{I_H} \right) \left( \frac{\sigma_{j \rightarrow i}(\varepsilon_j)}{\pi a_0^2} \right), \quad (2.2)$$

where  $a_0$  is the Bohr radius and  $I_H$  the Rydberg energy constant (i.e. ionisation energy of neutral hydrogen).

For thermal plasmas, that is plasmas for which the free electrons are Maxwellian, the Maxwell averaged collision strength  $\Upsilon_{ij}(T_e)$  is a preferred tabulation as a function of electron temperature  $T_e$  and is given by,

$$\Upsilon_{ij}(T_e) = \int_0^\infty \Omega_{ij}(\varepsilon_j) \exp\left(-\frac{\varepsilon_j}{kT_e}\right) d\left(\frac{\varepsilon_j}{kT_e}\right). \quad (2.3)$$

Concordant with  $\Omega_{ij}$ ,  $\Upsilon_{ij}$  is symmetrical between  $i$  and  $j$ . Thus, in the Maxwellian case, both the excitation and de-excitation rate coefficients (for use in the generalised collisional-radiative modelling described in section 2.2) are obtained from

$\Upsilon_{ij}$  as,

$$q_{i \rightarrow j}(T_e) = 2\sqrt{\pi}\alpha c a_0^2 \left(\frac{I_H}{kT_e}\right)^{1/2} \frac{1}{\omega_i} \exp\left(-\frac{\Delta E_{ij}}{kT_e}\right) \Upsilon_{ij}(T_e), \quad (2.4)$$

$$q_{j \rightarrow i}(T_e) = 2\sqrt{\pi}\alpha c a_0^2 \left(\frac{I_H}{kT_e}\right)^{1/2} \frac{1}{\omega_j} \Upsilon_{ij}(T_e), \quad (2.5)$$

where  $\alpha$  is the fine structure constant and  $c$  the speed of light in vacuum.

One of the most efficient and precise methods of calculating the excitation/de-excitation cross-section (and it is noted that modern pseudostate  $R$ -matrix calculations can also span ionisation cross-sections) is that of  $R$ -matrix (Burke and Robb, 1975). Where such data is available, it is used in the work here presented. The basis of  $R$ -matrix theory is the partitioning of configuration space into two distinct regions by a sphere around the nucleus. Electron interaction in the inner region requires inclusion of electron exchange and correlation. In this region, the impacting electron and target nucleus are treated as a single system using a close coupling expansion. In the outer region, the electron is considered sufficiently remote from the nucleus to reduce the interaction to a two-body, more easily solvable, problem. The connection between the two regions is described by a matrix  $R$ , which relates the wavefunction and its derivative at the boundary.

The  $R$ -matrix method is of special importance to the present work because of its correct and efficient handling of resonances. Resonances arise when the total energy of the impacting electron and target ion corresponds to the energy of a discrete, allowed state (a ‘doubly-excited’ state) of the intermediate system, i.e. the  $\mathcal{A}^{(z-1)+}$  system. This displays itself as a sharp spike, or resonance, in the cross-section across a narrow impacting electron energy. The effect of the resonance, viewed as an isolated state which breaks up again by the Auger reaction, is in general also subject to radiative damping (and possibly also Auger damping). Should the  $\mathcal{A}^{(z-1)+}$  system undergo a radiative transition, dielectronic recombination takes place rather than excitation. In an isolated resonance approximation, then the effect is that the resonance is damped by a factor,

$$\frac{A^a}{A^a + A^r}, \quad (2.6)$$

where  $A^r$  is the rate of recombination and  $A^a$  is the rate of Auger breakup. Figure 2.1 shows an  $R$ -matrix calculation by Ballance (2003) of the collision strength for the  $1s^2 1S - 1s3s^1S$  transition in neutral helium. Below the ionisation threshold value of the incident electron energy, the resonance behaviour is seen.

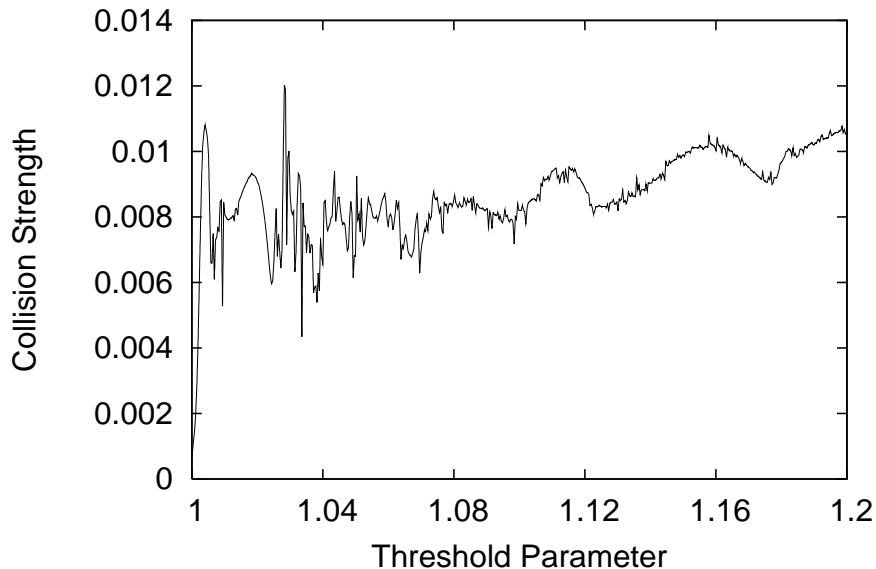


Figure 2.1: Collision strength of the  $1s^2\ ^1S - 1s3s\ ^1S$  transition in neutral helium, as calculated by Ballance (2003). The resonance structure resolved in detail using the  $R$ -matrix method is evident. The threshold parameter is defined as  $\varepsilon_i/\Delta E_{ij}$ , with the ionisation threshold at 1.07 on this scale.

Quadrature of the cross-section over a non-Maxwellian distribution will be shown to be unsafe without a proper representation of the resonant region.

Incident electrons with energy above included ionisation thresholds (that is excluding deep inner-shell loss from the  $N$ -electron configuration set in more complex ions than neutral helium) do not introduce resonances, with the cross-sections showing a smooth behaviour in this region. The latter region is therefore less critical. In practice, the  $R$ -matrix method is unsound above ionisation threshold unless pseudostates are included; the effect of pseudostates on the collision strength can be seen in figure 2.1 where there is an oscillatory nature above ionisation threshold. On going to high-energy, a larger number of basis orbitals must be included to span the continuum states and the  $R$ -matrix method becomes less efficient. There are many simpler theoretical approaches for these regions, without the error in principle of the resonance region for non-Maxwellians, but with some increased uncertainty. Of the methods made use of, the simplest is the plane wave Born approach, implemented in the Cowan code (Cowan, 1981). Improved, distorted wave, calculations include the work of Sampson and co-workers (Goett and Sampson, 1983; Sampson *et al.* 1985a, 1985b; Sampson, 1986; Zhang *et al.* 1986, 1990) and the HULLAC (Bar-Shalom *et al.* 1988) and FAC (Gu, 2003) codes. These include the highly efficient factorised method of Bar-Shalom *et al.* (1988),

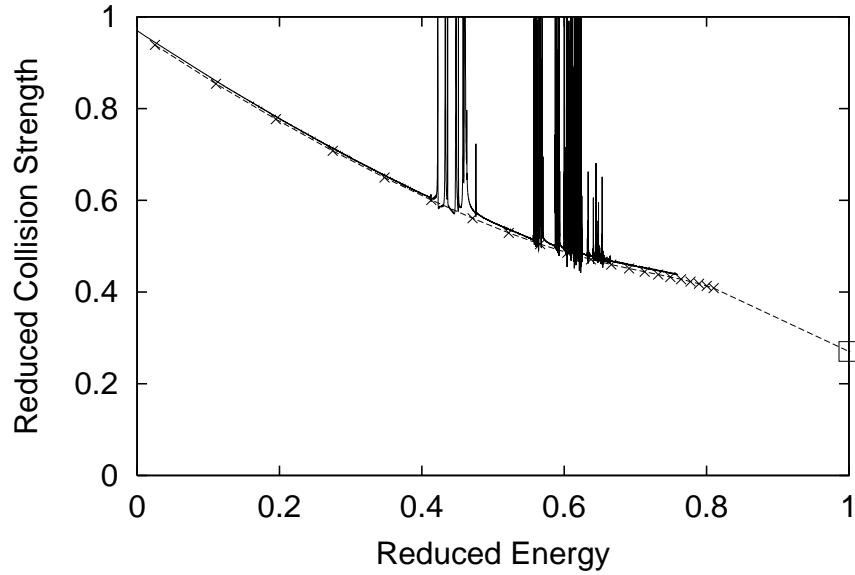


Figure 2.2: Reduced electron-impact excitation collision strengths for the  $1s^2 2s^2 \text{S} - 1s^2 2p^2 \text{P}$  transition in  $\text{Ar}^{15+}$  obtained using Burgess-Tully reduced parameter in a C-plot with  $C = 3$ . The solid curve denotes the results of Whiteford *et al.* (2002) using an  $R$ -matrix method showing the detailed resonance structure. The dashed curve and crosses denote the distorted-wave results presented by Merts *et al.* (1980). The straight line between the last point of Merts and the infinite-energy limit point (square box) shows the approach to the limit point.

which splits the angular and radial parts of the distorted-wave problem to obtain intermediate coupled cross-sections. The configuration-averaged distorted-wave (CADW) approximation of Pindzola *et al.* (1986a, 1986b) which is also used for ionisation reactions (see section 2.1.2), is also made use of. Figure 2.2 shows a comparison of  $R$ -matrix against DW for the collisional excitation cross-section for the  $1s^2 2s^2 S - 1s^2 2p^2 P$  transition in  $\text{Ar}^{15+}$ . The DW calculation is seen to trace the form of the  $R$ -matrix calculation, but without accounting for the resonance structure below ionisation threshold.

It has been mentioned that the resonance structure of the excitation cross-section is of particular relevance to non-Maxwellian modelling and justification of this is given here. Reaction cross-sections become of practical use for plasma modelling when integrated over the electron distribution function to form rate coefficients. This is examined further in section 3.2, but let us consider, here, what one requires from the cross-section data for such a quadrature to be acceptable. To take proper account of the resonance region, the collision strength must vary more slowly with energy than the distribution function. ‘Energy scale lengths’, in terms of incident electron energy, may be defined for the collision strength and distribution function, as

$$\lambda_{\Omega}^{-1} = \frac{d}{dX} \ln \Omega \quad (2.7)$$

$$\lambda_f^{-1} = \frac{d}{dX} \ln f, \quad (2.8)$$

in terms of the threshold scaled energy  $X = \varepsilon_i / \Delta E_{ij}$  (usually called the threshold parameter).  $\lambda_{\Omega}$  is the energy scale length of the collision strength, and  $\lambda_f$  that of the distribution function  $f$ .

As an illustration of smoothing through a resonance region causing a problem, consider the neutral helium transition  $1s^2 1S - 1s3p^3P$ . The resonant region of the collision strength is shown in figure 2.3 from an  $R$ -matrix calculation (Ballance, 2003), along with a reduced smoother data set of only 14 points in comparison to the  $\sim 7000$  of  $R$ -matrix. Figure 2.4 shows scale lengths of the reduced collision strength and of a Maxwellian distribution at various temperatures. This is the same transition as figure 2.3 but over an extended energy range, the original collision strength data now has  $\sim 34,000$  data points and the interval averaged has 34. It is apparent that quadrature in this representation of the collision strength with a Maxwellian below 50 eV is unsafe as the scale length of the collision strength exceeds that of the distribution at  $X \simeq 0.2$ .

For non-Maxwellian distributions, the issue can be exacerbated. Figure 2.5

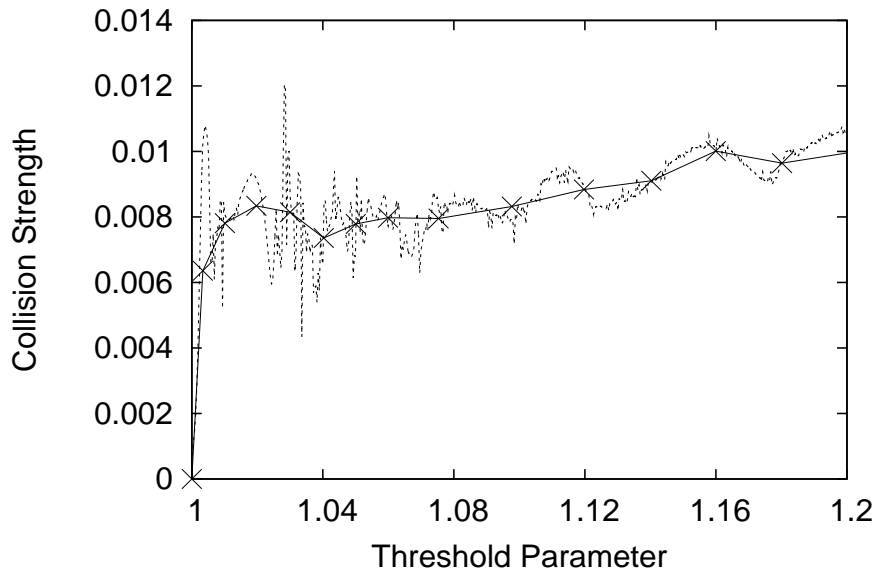


Figure 2.3: Collision strength for the  $1s^2\ ^1S - 1s3s\ ^1S$  transition in neutral helium. The dashed line shows the  $R$ -matrix results of Ballance (2003) with  $\sim 7000$  points and the solid line interval averages through this data to deliver 14 smoothed tabular points. The method of calculating this averaged data can be found in Paton (2005).

shows a similar plot to that of figure 2.4 but with a  $\kappa$  distribution (see section 3.1.1 for further detail) of effective temperature 50 eV. Quadrature over a Maxwellian at this temperature was found to be safe (figure 2.4) with this collision strength, but, on deviating from Maxwellian form, this is not so.

Detailed evaluation of  $\Upsilon$  from equation 2.3 and its non-Maxwellian equivalents is given in section 3.2.1, but attention is drawn here to the ‘ $C$ -plot’ of Burgess and Tully (1992), which is found helpful and used extensively (some of the figures of this section have already been plotted using this format). Proposed as a means of compacting and assessing data and checking high energy limit points, the collision strength is scaled to remove asymptotic energy dependence and plotted as a function of collision energy mapped onto the interval  $[0, 1)$ .

The scaling of the collision strength is determined by categorising each transition into one of four possible types. Type 1 transitions are optically allowed, with a non-zero electric dipole interaction between initial and final states. The high-energy non-relativistic limiting behaviour of such transitions is given by the Bethe approximation (1930) as,

$$\lim_{\varepsilon_i \rightarrow \infty} \Omega = A \ln \varepsilon_i, \quad (2.9)$$

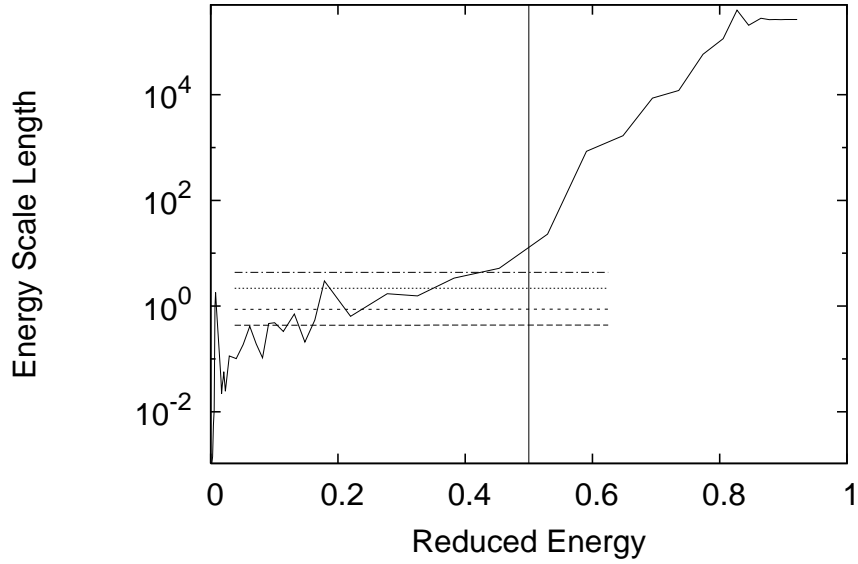


Figure 2.4: Energy scale lengths for the averaged collision strength data shown in figure 2.3 (but over an extended energy range) and for Maxwellian distributions with electron temperatures of 10 eV (long dashed line), 20 eV (short dashed line), 50 eV (dotted line) and 100 eV (dot-dashed line). The plot is against reduced energy as defined by Burgess and Tully (1992) with  $C$  chosen to place ionisation threshold at  $x = 0.5$ . Quadrature of this collision strength with a Maxwellian is seen to be unsafe below a temperature of 50 eV.

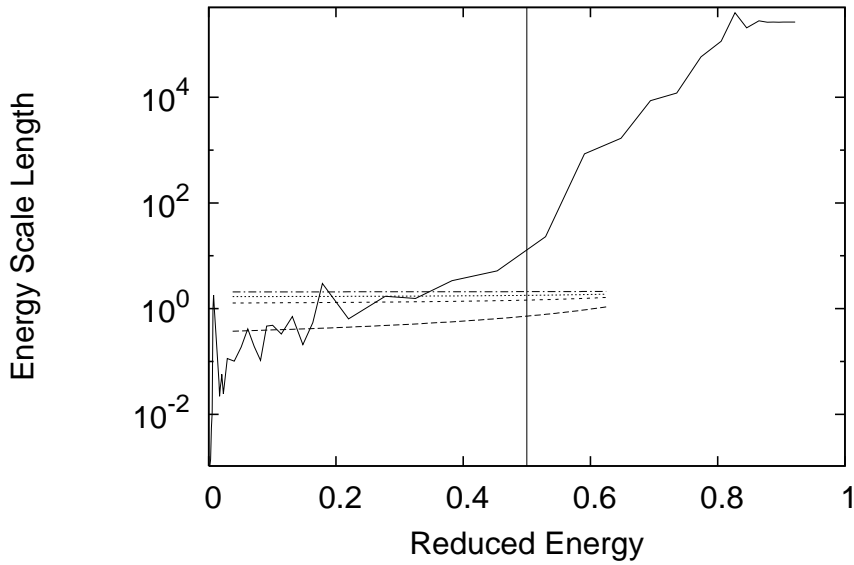


Figure 2.5: As in figure 2.4 but with various  $\kappa$  distributions in place of Maxwellians. All distributions have effective temperature of 50 eV, with  $\kappa = 2$  (long dashed line), 5 (short dashed line), 10 (dotted line), 50 (dot-dashed line).

with  $A$  a constant – the first Bethe coefficient. The reduced collision strength,  $\Omega_r$ , and reduced collision energy,  $E_r$ , are defined as,

$$E_r = 1 - \frac{\ln C}{\ln(X - 1 + C)}, \quad (2.10)$$

$$\Omega_r = \frac{\Omega}{\ln(X - 1 + e)}. \quad (2.11)$$

Optically forbidden transitions, induced by higher electric or magnetic multipole moments, are termed type 2. Limiting behaviour is given by the Born approximation (Mott and Massey, 1949) to be,

$$\lim_{\varepsilon_i \rightarrow \infty} \Omega = B, \quad (2.12)$$

where the constant  $B$  is the second Bethe coefficient. The collision strength and incident energy are  $C$ -plot scaled as,

$$E_r = \frac{X - 1}{X - 1 + C}, \quad (2.13)$$

$$\Omega_r = \Omega. \quad (2.14)$$

Type 3 transitions are those involving a change of spin of the ion through ex-

change between incident and bound electron. The Ochkur approximation (1964) gives high-energy limit behaviour as,

$$\lim_{\varepsilon_i \rightarrow \infty} \Omega = D/\varepsilon_i^2, \quad (2.15)$$

where  $D$  is a constant, leading to,

$$E_r = \frac{X - 1}{X - 1 + C}, \quad (2.16)$$

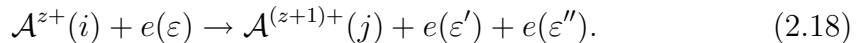
$$\Omega_r = X^2 \Omega. \quad (2.17)$$

In the above scalings, a threshold parameter,  $X$  as defined above, is used. The parameter  $C$  is selected to optimise the distribution of tabular points along the scaled ‘ $x$ ’ axis.

Burgess and Tully also specify, in a sub-distinction in type 1, a fourth, weak dipole, transition type, but this will not be discussed here.

### 2.1.2 Ionisation

The basic electron-driven ionisation reaction of an ion  $\mathcal{A}$  in charge state  $z$  is



with the ion initially in state  $i$  and the struck electron directly entering the continuum of the residual ion of charge state  $z + 1$  which is left in the state  $j$ . This is often considered as, in effect, ionisation from the ground state of the ion  $\mathcal{A}^{z+}$  to the ground state of the ion  $\mathcal{A}^{(z+1)+}$ . Collisional-radiative modelling (see section 2.2), however, requires more detailed distinctions of initial and final states. Ionisation reactions from ground and metastable states must be made distinct from true excited states, and the final state, ground or metastable or possibly excited, matters. Ionisation from excited states in collisional-radiative modelling is the last stage of a multi-step process propagating from a ground or metastable state initially. The final ionisation is dominated by the loss of the valence or Rydberg electron directly to the continuum. This is a non-resonant process, smoothly varying with incident electron energy. The greater concern, then, is with ionisation in which  $i$  and  $j$  in the above equation correspond to ground or metastable states  $\rho$  and  $\sigma$ . In this case the struck electron may be an inner shell electron as well as the valence electron, giving the possibility of the

reaction sequence,

$$\mathcal{A}^{z+}(\rho) + e(\varepsilon) \rightarrow \mathcal{A}^{z+}(k) + e(\varepsilon') \rightarrow \mathcal{A}^{(z+1)+}(\sigma) + e(\varepsilon') + e(\varepsilon''), \quad (2.19)$$

where  $\mathcal{A}^{z+}(k)$  is a resonant, doubly-excited state, which autoionises. The autoionisation may be in competition with a radiative reaction, stabilising the system back into a state of the  $\mathcal{A}^{z+}$  ion (see dielectronic recombination, section 2.1.3) as,

$$\mathcal{A}^{z+}(k) + e(\varepsilon') \rightarrow \mathcal{A}^{z+}(j) + e(\varepsilon') + h\tilde{\nu}. \quad (2.20)$$

Called ‘excitation-autoionisation’, it is a resonant process for which the ionisation cross-section is not smoothly varying with incident electron energy.

Ionisation cross-section measurements primarily come from electron cyclotron resonance (ECR) sources and from heavy-ion storage rings (e.g. CRYRING at Stockholm, Sweden and the Test Storage Ring at Heidelberg, Germany). The most common measurement technique is the crossed-beam method (Harrison, 1968; Dolder and Peart, 1976), examples of such measurements being Woodruff *et al.* (1978), Falk *et al.* (1983), Linkemann *et al.* (1995), Müller *et al.* (2000) and Fogle *et al.* (2003). Other methods include the hollow electron-beam technique (Hartnagel, 1964, 1965, 1966; Hasted and Awad, 1972; Hamdan *et al.* 1978). Such measurements, in principle, delimit the detail of the excitation-autoionisation contributions with energy, but the separation of ground and metastable initial states and resolution of the final state is difficult. In general, the source of the target ions provides an unknown mixture of ground and metastable states, with the metastable component cross-sections imperfectly resolved by examination of the near-threshold (above and below) region of the measured cross-section. The experimental database is mostly for moderate states of ionisation and can have fairly substantial error bars through the autoionising resonance region. *Ab initio* theoretical methods, which can match the quality of experiment, comprise only *R*-matrix with pseudostates (RMPS; Bartschat *et al.* 1996; Gorczyca and Badnell, 1997; see also section 2.1.1), convergent close coupling (CCC; Bray and Stelbovics, 1993) and time dependent close coupling (TDCC; Pindzola and Robicheaux, 1996). Whereas the *R*-matrix method can handle the autoionising resonances well, it must be used with a continuum-spanning pseudostate basis to give the non-resonant part correctly. Also, TDCC and CCC are, at the moment, suitable for at most two electrons outside a frozen core. These theoretical methods have been used only for a few near-neutral systems so far; recent studies include CCC calculations for neutral Li by Schweinzer *et al.* (1999), and all ionisation

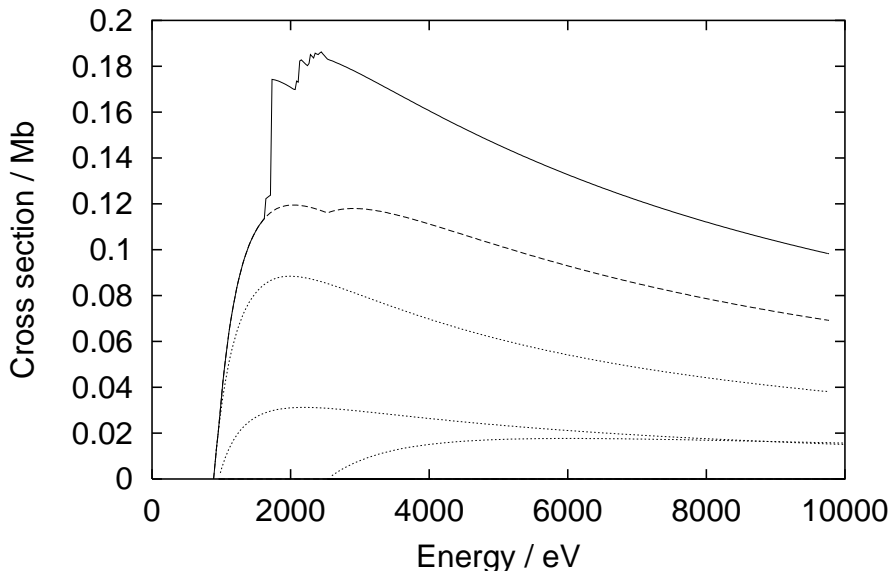


Figure 2.6: CADW cross-sections for  $\text{Kr}^{20+}$  (Loch *et al.* 2002). The dotted lines denote the contributions from the various direct ionisation routes from the 2p, 3s and 3p sub-shells, along with the total for direct ionisation (dashed line) and the total cross-section including excitation-autoionisation (solid line).

stages of Be by Colgan *et al.* (2003) using TDCC and RMPS. Of reasonable precision, but less accurate than the above, are the distorted wave methods (also used in the calculation of excitation cross-sections, see section 2.1.1) which include modelling of excitation-autoionisation via an independent processes approximation. The variant used most for the large-scale production of ionisation cross-sections is the configuration-averaged distorted-wave (CADW; Pindzola, 1986a, 1986b) method. It includes detailed splitting of autoionising configurations which span the ionisation threshold by associated intermediate coupling structure calculations. In illustration, figure 2.6 shows the CADW ionisation cross-sections for  $\text{Kr}^{20+}$  as calculated by Loch *et al.* (2002). The figure highlights direct ionisation from each of the 2p, 3s and 3p shells, as well as excitation-autoionisation. Of particular importance to the present work is the resonant region between the ionisation threshold of the 3p-shell to that of the 2p-shell.

CADW is less reliable for ionisation of neutral and near-neutral ions, often overestimating the cross-section (Colgan *et al.* 2001). Also, the approximation becomes increasingly inaccurate as the  $n$ -shell of the impacted electron increases (Colgan *et al.* 2003). Figure 2.7 shows a comparison of a cross-section as calculated by CADW (Loch *et al.* 2005) with experimental results for ionisation of  $\text{C}^{2+}$ .

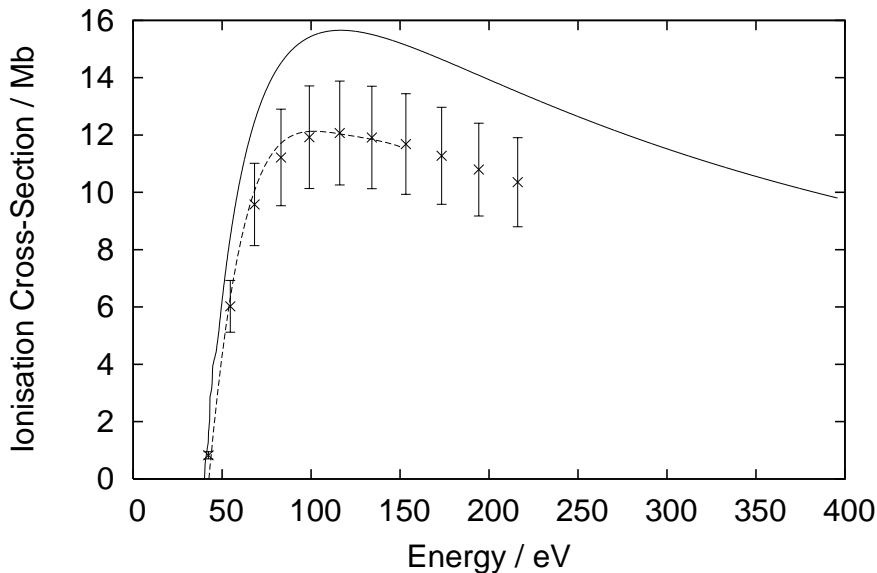


Figure 2.7: The ionisation cross-section of  $C^{2+}$  as calculated by the CADW method (Loch *et al.* 2005; solid line) and the RMPS method (Loch *et al.* 2005; dashed line). The experimental results, with error bars, of Fogle *et al.* (2003) show CADW to overestimate the cross-section.

CADW is seen to significantly exceed the results of experiment. The main delivered results from CADW in the international databases are as Maxwell averaged ionisation rate coefficients.

There has been a substantial investment of effort in simple analytic and semi-empirical expressions of ionisation cross-sections. These have their origin in the early classical expression of the cross-section for ionisation directly to the continuum given by Thomson (1912),

$$\sigma_{i \rightarrow +}(\varepsilon) = 4\zeta\pi a_0^2 \frac{I_H}{I_i} \frac{I_H}{\varepsilon} \left(1 - \frac{I_i}{\varepsilon}\right). \quad (2.21)$$

$\zeta$  in the above expression signifies the number of equivalent electrons in the valence shell of the target ion and  $I_i$  is the ionisation potential of state  $i$ . Note that the expression is a function only of the incoming electron energy; it is a total ionisation cross-section in that it has been summed over all energies of the ejected electrons.

The wide class of relatively simple, but practical ionisation expressions, beyond Thomson, have been produced by focusing on the shell structure of the target (for example Lotz, 1968) with further improvements once the categorising of excitation-autoionisation situations took place. The most successful of the

latter is that of Burgess and Chidichimo (1983). They express the cross-section as,

$$\sigma^{\text{bchid}}(z, \varepsilon) = C \sum_i \zeta_i \left( \frac{I_{\text{H}}}{I_i} \right)^2 \frac{I_i}{\varepsilon} \ln \left( \frac{\varepsilon}{I_i} \right) W \left( \frac{\varepsilon}{I_i}, z \right) \pi a_0^2, \quad (2.22)$$

where the summation is over states  $i$  of the initial ion and the function  $W(x, z)$  is given by,

$$W(x, z) = \begin{cases} 0 & (x \leq 1) \\ [\ln(x)]^{\beta(z)/x} & (x > 1) \end{cases} \quad (2.23)$$

where

$$\beta(z) = \frac{1}{4} \left[ \left( \frac{100z + 91}{4z + 3} \right)^{1/2} - 5 \right]. \quad (2.24)$$

Experimental measurements, at the time of publication by Burgess and Chidichimo (1983), suggested  $C = 2.3$ .

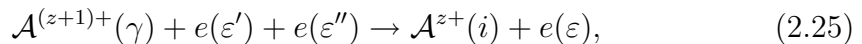
Analogous to the arguments made in section 2.1.1 concerning smoothing through resonance regions of excitation cross-sections, special attention need be drawn to the level of data of this reaction. Burgess and Chidichimo (1983) address this issue by a flexible representation of  $I_i$  and  $\zeta_i$  for the different shells of the ionising configuration. Two distinct cases, labelled (i) and (ii) as introduced by Burgess *et al.* (1977), are used. The case (i) representation holds when the lowest autoionising level of an inner-shell excitation lies above the ionisation potential of the outer-shell. In this case, excitation-autoionisation is incorporated into the direct shell ionisation by lowering the ionisation potential of the inner-shell electron to the energy to excite to the lowest autoionising level. Should the excitation energy of the lowest autoionising level of the inner-shell electron lie below the ionisation potential of the outer-shell electron, the case (ii) representation is used. Here, the densely lying autoionising levels extend from below the ionisation potential of the outer-shell electron through to the continuum. Excitation-autoionisation is then incorporated by lowering the ionisation potential of the inner-shell electron to that of the outer-shell electron, so that one now has a cross-section determined by the ionisation potential of the outer-shell electron but with the number of equivalent electrons equal to the sum of those in the inner and outer shells. This representation holds if the autoionising levels are considered to have unit probability of autoionising, i.e.  $A^{\text{a}} \gg A^{\text{r}}$ . It is, therefore, unsound without further adjustment for higher charge states as radiative decay becomes comparable to the Auger processes. It is also to be noted that while the semi-empirical formulation of Burgess and Chidichimo takes into account excitation-autoionisation routes,

it does not fully resolve the resonance structure due to these paths. The semi-empirical formulae of Burgess and Chidichimo provide both the cross-section and the Maxwell averaged rate coefficient. The Maxwell averaged formula may be treated as a parametric form to be fitted to best available ionisation rate coefficient data. As such, it can be viewed as a ‘support function’ which gives a reasonable representation also of the cross-section. Such support functions can enable exploitation of the legacy of Maxwellian ionisation rate coefficients in the international databases in the non-Maxwellian environment. This is addressed in section 3.2 in reference to both ionisation and dielectronic recombination.

Stepwise excitation followed by ionisation from true excited states becomes dominant in high-density, low-temperature plasmas. There is almost no high-precision experimental or theoretical data for such cross-sections (apart from neutral hydrogen — see Bray and Stelbovics, 1993; Bray, 2002). The most suitable simple theoretical formulation of the excited state ionisation is the Exchange Classical Impact Parameter method (ECIP; Burgess, 1964). Although not a full quantum mechanical treatment, it represents an approach beyond the simple classical binary encounter of Thomson. A properly symmetrised classical encounter including orbital motion of the atomic electron and the possibility of electron exchange is used for low values of the impact parameter. For large values, compared with the atomic radius, a semi-classical perturbation treatment is used to give the correct high energy behaviour. It provides the cross-section as well as the Maxwell averaged rate coefficient.

### 2.1.3 Recombination

An electron recombining with an ion  $\mathcal{A}^{(z+1)+}$  to form  $\mathcal{A}^{z+}$  can do so by three processes: radiative recombination, dielectronic recombination and three-body recombination. Three-body recombination,



with the initial ion  $\mathcal{A}^{(z+1)+}$  in the state  $\gamma$  and  $i$  the final captured state of the ion  $\mathcal{A}^{z+}$ , requires two incoming electrons to impact the ion and so is separate from dielectronic and radiative recombination. It is the inverse process to collisional ionisation, of which more detail was given in section 2.1.2 and where the cross-sections governing the reaction were discussed. The relation between the three-body recombination coefficient,  $\alpha_{\gamma^+ \rightarrow i}^{(3)}$ , and the ionisation rate coefficient,  $q_{i \rightarrow \gamma^+}$ ,

is obtained from detailed balance in the Maxwellian case as,

$$\alpha_{\gamma^+ \rightarrow i}^{(3)} = 8 \left( \frac{\pi a_0^2 I_H}{kT_e} \right)^{3/2} \frac{\omega_i}{2\omega_\gamma} e^{I_i/kT_e} q_{i \rightarrow \gamma^+}. \quad (2.26)$$

The notation  $\gamma^+$  in  $\alpha_{\gamma^+ \rightarrow i}^{(3)}$  and  $q_{i \rightarrow \gamma^+}$  is used to denote the state  $\gamma$  of the ion  $\mathcal{A}^{(z+1)+}$ . The process is negligible unless the electron density is high. In the non-Maxwellian case, it may be obtained from the differential ionisation cross-section by detailed balance (see section 3.2) and is not considered further here.

However, quantum mechanically, dielectronic and radiative recombination are indistinguishable processes which interfere with each other. Pindzola *et al.* (1992) have shown that this interference is a very small effect and can safely be neglected for GCR modelling. This gives the independent processes approximation whereby dielectronic and radiative recombination can be considered separately.

Radiative recombination is essentially the non-resonant capture, equivalent to spontaneous emission in bound states in which the electron spontaneously emits a photon, but in a free-bound transition,

$$\mathcal{A}^{(z+1)+}(\gamma) + e(\varepsilon l) \rightarrow \mathcal{A}^{z+}(i) + h\tilde{\nu}. \quad (2.27)$$

The final state  $i$  is of the form  $\gamma, n'l'$ . The latter notation indicates that the parent ion state  $\gamma$  is passive in the process. The conversion of radiative recombination from Maxwellian to non-Maxwellian distributions does not incur the same difficulties as resonant reactions. The non-resonant nature of this process means that cross-sections are smoothly varying, with no immediate danger involved by representing the cross-section on a sparse energy grid or by invoking simpler approximations.

Cross-section relations are determined by considering the inverse photoionisation reaction (the  $\gamma, n'l'$  notation is now used),

$$\mathcal{A}^{z+}(\gamma, n'l') + h\tilde{\nu} \rightarrow \mathcal{A}^{(z+1)+}(\gamma) + e(\varepsilon l), \quad (2.28)$$

and the stimulated recombination process,

$$\mathcal{A}^{(z+1)+}(\gamma) + e(\varepsilon l) + h\tilde{\nu} \rightarrow \mathcal{A}^{z+}(\gamma, n'l') + h\tilde{\nu} + h\tilde{\nu}. \quad (2.29)$$

We thus have the capture cross-section  $Q_c(\tilde{\nu})$ , the photoionisation cross-section  $a(\tilde{\nu})$ , and the stimulated capture cross-section  $\sigma(\tilde{\nu})$ . These are connected by the

Milne relations,

$$Q_c(\tilde{\nu}) = \left( \frac{h\tilde{\nu}}{mvc} \right)^2 \frac{\omega_i}{\omega_\gamma} a(\tilde{\nu}), \quad (2.30)$$

and

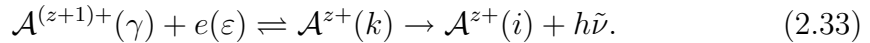
$$\sigma(\tilde{\nu}) = \frac{c^3}{8\pi h\tilde{\nu}^3} Q_c(\tilde{\nu}), \quad (2.31)$$

where  $m$  and  $v$  are the mass and speed of the impacting electron. As in the excitation case of section 2.1.1, the Maxwell averaged recombination coefficient is formed by integrating over the Maxwellian distribution to give,

$$\alpha_{\gamma^+ \rightarrow i}^{(r)}(T_e) = 8 \left( \frac{\pi a_0^2 I_H}{kT_e} \right)^{3/2} \frac{\pi \alpha^4 c}{3\sqrt{3}\pi a_0} z_1^4 \left( \frac{2}{\nu_i^3} \right) e^{I_i/kT_e} \int_{I_i/kT_e}^{\infty} \frac{g^{\text{II}} e^{-x}}{x} dx, \quad (2.32)$$

where  $\nu_i$  is the effective principal quantum number of the Rydberg electron in state  $i \equiv \gamma, n'l'$ , and the free-bound Gaunt factor  $g^{\text{II}}$  has been introduced. For more detail on Gaunt factors and their calculation, see section 3.2.2.

Dielectronic recombination is the electron capture via resonances of the target ion and incident electron system. This part dominates the non-resonant radiative recombination in low-density, high-temperature plasmas, but can also dominate at low-temperature in photoionised plasmas. In the isolated resonance approximation, it can be viewed as two discrete stages; namely, resonance capture of an electron, followed by radiative stabilisation:



The continuum electron energy  $\varepsilon \simeq E_c$  within an Auger width where  $E_c = E(k) - E(\gamma) \simeq E(\gamma') - E(\gamma) + z^2/\nu^2$ .  $\nu$  is the effective principal quantum number of the Rydberg electron  $nl$  in the notation  $\gamma', nl$  for the doubly excited resonance state  $k$  and  $\gamma'$  is the promoted parent state. There are two primary factors that determine the importance of this process. Firstly, the resonance capture can undergo its inverse Auger breakup reaction before the recombination process can be completed by the stabilisation reaction. The so-called branching ratio for radiative stabilisation  $A^r/(A^a + A^r)$ , where  $A^a$  is the Auger transition rate and  $A^r$  the stabilising radiative transition rate, is important since it determines the effective contribution of the isolated resonance to the net dielectronic recombination. A second determining factor is the central resonant energy of the transition,  $E_c$ , which manifests itself as an exponential factor in the Maxwellian situation. Taking this into account, the partial dielectronic recombination rate

coefficient  $\alpha_{\gamma^+ \rightarrow i}^{(d)}$  from an initial metastable state,  $\gamma$ , into a resolved final state,  $i$ , of the ion  $\mathcal{A}^{+z}$  is given by

$$\alpha_{\gamma^+ \rightarrow i}^{(d)}(T_e) = \left( \frac{4\pi a_0^2 I_H}{kT_e} \right)^{3/2} \sum_k \frac{\omega_k}{2\omega_\gamma} e^{-E_c/kT_e} \times \frac{\sum_l A_{k \rightarrow \gamma, E_{cl}}^a A_{k \rightarrow i}^r}{\sum_h A_{k \rightarrow h}^r + \sum_{m,l} A_{k \rightarrow m, E_{cl}}^a}, \quad (2.34)$$

where  $\omega_k$  is the statistical weight of the  $(N+1)$ -electron doubly-excited resonance state  $k$ , and  $\omega_\gamma$  is the statistical weight of the  $N$ -electron target state.  $A^a$  and  $A^r$  are in inverse seconds and  $E_c$  is fixed by the position of each resonance. As the process is inherently resonant in energy, it poses the greatest likelihood of sensitivity when considering non-Maxwellian distributions.

There has been substantial work done on evaluating and tabulating state-selective dielectronic recombination in Maxwellian electron plasmas. The most recent (and an introduction to a series of papers on different iso-electronic sequences) is described by Badnell *et al.* (2003). The primary data is very extensive and tabulated according to the format (*adf09*) of the ADAS Project. At issue is whether this Maxwellian data remains useful in the non-Maxwellian electron case. It matters whether a given state selective dielectronic recombination coefficient depends on a single or on multiple resonances. The latter situation can occur when more than one parent transition is possible and if an outer electron as well as an inner electron may make the stabilising transition. The single contributing resonance is straightforward for the non-Maxwellian case since only a single free-electron energy is sampled from the distribution function and the Maxwellian data can be exploited. The multiple case is more difficult since there is not one unique energy. The problem will be examined in detail in section 3.2. However, it is noted that for dielectronic recombination, a support function, equivalent to that used for ionisation, can be prepared. This is the ‘Burgess–Bethe general program’ (BBGP; Badnell *et al.* 2003). In that work, it was demonstrated that BBGP could be determined from relatively simple atomic energy level and transition probability data of the type generated for low-level collisional-radiative calculations (format *adf04* in ADAS) and that BBGP could be used with adjustable parameters to fit best available Maxwellian dielectronic recombination data at zero density. BBGP was then used to step off from the zero density situation to finite density (with respect to collisional redistribution of the doubly excited intermediate resonance populations). It can be used in a like manner to step off into the non-Maxwellian dielectronic recombination situation.

## 2.2 Generalised Collisional-Radiative Modelling

As previously stated, the present work seeks to be as general in applicability as possible; generalised collisional-radiative (GCR) theory is introduced for this purpose. The basic collisional-radiative model was introduced by Bates *et al.* (1962) in an attempt to model correctly a plasma which could not be described adequately by the low-density approximation nor by the high-density local thermodynamic equilibrium scenario. The generalised extension to include dynamic treatment of metastable states was introduced by Summers and Hooper (1983).

Central to such a model is an understanding of the lifetimes of atoms in the plasma. These lifetimes are divided into two groups based on their relaxation timescales: the extrinsic collisional group and the intrinsic atomic group. The collisional timescales, which depend on plasma conditions, comprise free-electron thermalisation,  $\tau_{ee}$ ; positive-ion thermalisation,  $\tau_{ii}$ ; ion-electron equilibration,  $\tau_{ie}$ ; and ionisation,  $\tau_{ion}$ . The intrinsic group are purely atomic parameters, comprising metastable radiative decay,  $\tau_m$ ; ordinary excited state radiative decay,  $\tau_o$ ; and autoionising state decay,  $\tau_a$ .

The rank order of the plasma particle thermalisation timescales can be determined from the particle self-collision time (Spitzer, 1956),

$$\tau = \frac{0.12}{\alpha c a_0^2} \left( \frac{m}{m_e} \right)^{1/2} \left( \frac{kT_e}{I_H} \right)^{3/2} \frac{1}{N z^4 \ln \Lambda}, \quad (2.35)$$

to give relative collision times,

$$\tau_{ee} : \tau_{ii} : \tau_{ie} = 1 : \frac{1}{z^4} \left( \frac{m_i}{m_e} \right)^{1/2} \left( \frac{T_i}{T_e} \right)^{3/2} : \frac{1}{z^2} \left( \frac{\pi}{6} \right)^{1/2} \frac{m_i}{m_e}. \quad (2.36)$$

$\ln \Lambda$  is the Coulomb logarithm, where  $\Lambda$  is the ratio of the Debye length to the distance of closest approach in Coulomb collisions. This short timescale assumption for energy redistribution in electron-electron collisions is the basis behind Maxwellian modelling of the free-electron distribution. The relatively low mass of the electrons does also facilitate their participation in the flow of energy from input and output sources, however. Such sources can be sufficiently large and rapid that energy re-distribution amongst electrons is incomplete, non-Maxwellian distributions being the result.

For a typical astrophysical or magnetically confined fusion plasma, the order-

ing of the atomic timescales is,

$$\tau_a \ll \tau_o \ll \tau_m, \quad (2.37)$$

where typical values for the solar atmospheric conditions of section 2.3 are,

$$\tau_o \sim \frac{10^{-8}}{z_1^4} \text{ s} \quad (2.38)$$

$$\tau_m \sim \frac{10}{z_1^8} \text{ s} \quad (2.39)$$

$$\tau_a \sim 10^{-12} \text{ s}. \quad (2.40)$$

It follows that there is a natural separation of the metastable and excited and autoionising states of the atom. Each ionisation stage is partitioned into the ground and metastable states, which must be treated dynamically, and the excited and autoionising states, treated as in quasi-static equilibrium with the metastables. The GCR model provides a connection between the dynamic and quasi-static populations.

When modelling a plasma, comparison of the timescales of the plasma to atomic parameters is made. It is essential in determining which processes to model dynamically that these timescales are also related to those of the transient plasma phenomena under study,  $\tau_p$ . Section 2.3 considers situations in the solar atmosphere where the plasma evolves on a timescale of the order of the metastables and ionisation,

$$\tau_p \sim \tau_m \sim \tau_{\text{ion}} \gg \tau_o \gg \tau_{ee}. \quad (2.41)$$

It is the common assumption that electron-electron collisional timescales are shorter than the other timescales of interest, and the free electrons have a Maxwellian distribution. The bulk of the work presented here is of situations where equation 2.41 does not hold, rather,

$$\tau_p \sim \tau_m \sim \tau_{\text{ion}} \sim \tau_{ee}. \quad (2.42)$$

The population equations of a state  $i$  of the ion  $\mathcal{A}^{z+}$  are determined by considering the populating and de-populating processes of the said state. Writing

ordinary levels with Roman indices and metastables with Greek, we have,

$$\begin{aligned}
\frac{dN_i}{dt} = & \sum_{\gamma} N_e N_{\gamma}^+ \left( \alpha_{\gamma \rightarrow i}^{(r)} + \alpha_{\gamma \rightarrow i}^{(d)} + N_e \alpha_{\gamma \rightarrow i}^{(3)} \right) + \sum_{\gamma} N_H N_{\gamma}^+ \alpha_{\gamma \rightarrow i}^{(\text{cx})} \\
& + \sum_{j < i} N_j N_e q_{j \rightarrow i} + \sum_{j > i} N_j (N_e q_{j \rightarrow i} + A_{j \rightarrow i}) \\
& - N_i \left[ \sum_{j > i} N_e q_{i \rightarrow j} + \sum_{j < i} (N_e q_{i \rightarrow j} + A_{i \rightarrow j}) \right. \\
& \left. + \sum_{\gamma} (N_e S_{i \rightarrow \gamma} + A_{i \rightarrow \gamma}^a) \right], \tag{2.43}
\end{aligned}$$

where the notation  $N$  and  $N^+$  refers to the populations of  $\mathcal{A}^{z+}$  and  $\mathcal{A}^{(z+1)+}$  respectively. The final term of equation 2.43 refers to secondary autoionisation, and only applies to excited states built on a metastable parent. By introducing the collisional-radiative matrix,  $C_{ij}$ , equation 2.43 reduces to,

$$\frac{dN_i}{dt} = N_e r_{i\gamma} N_{\gamma}^+ + N_H r_{i\gamma}^{(\text{cx})} N_{\gamma}^+ - C_{ij} N_j, \tag{2.44}$$

with a populating term,

$$C_{ij} = \begin{cases} -(A_{j \rightarrow i} + N_e q_{j \rightarrow i}) & i < j \\ N_e q_{j \rightarrow i} & i > j \end{cases} \tag{2.45}$$

a loss term,

$$C_{ii} = \sum_{i > j} A_{i \rightarrow j} + N_e \sum_{i \neq j} q_{i \rightarrow j} + \sum_{\gamma} N_e S_{i \rightarrow \gamma} + \sum_{\gamma} A_{i \rightarrow \gamma}^a, \tag{2.46}$$

a composite recombination coefficient,

$$r_{i\gamma} = \alpha_{\gamma \rightarrow i}^{(r)} + \alpha_{\gamma \rightarrow i}^{(d)} + N_e \alpha_{\gamma \rightarrow i}^{(3)}, \tag{2.47}$$

and a charge-exchange recombination coefficient,

$$r_{i\gamma}^{(\text{cx})} = \alpha_{\gamma \rightarrow i}^{(\text{cx})}. \tag{2.48}$$

Then, using the quasi-static equilibrium postulate,

$$\frac{d}{dt} N_{\sigma} \neq 0, \tag{2.49}$$

for metastables and,

$$\frac{d}{dt}N_i = 0, \quad (2.50)$$

for ordinary states. The equations for the metastable populations are usually given in terms of the ‘collisional dielectronic’ effective ionisation and recombination coefficients,  $S_{cd}$  and  $\alpha_{cd}$  respectively, such that,

$$\begin{aligned} \frac{d}{dt}N_\sigma &= -(C_{\sigma\rho} - C_{\sigma j}C_{ji}^{-1}C_{i\rho})N_\rho + (r_{\sigma\gamma} - C_{\sigma j}C_{ji}^{-1}r_{i\gamma})N_eN_\gamma^+ \\ &\quad + \left(r_{\sigma\gamma}^{(cx)} - C_{\sigma j}C_{ji}^{-1}r_{i\gamma}^{(cx)}\right)N_{\text{H}}N_\gamma^+ \\ &= -N_eN_\sigma S_{cd} + N_eN_\gamma^+ \alpha_{cd} + N_{\text{H}}N_\gamma^+ \alpha_{cd}^{(cx)}. \end{aligned} \quad (2.51)$$

Populations of ordinary levels can be written,

$$\begin{aligned} N_j &= -C_{ji}^{-1}C_{i\sigma}N_\sigma + C_{ji}^{-1}r_{i\gamma}N_\gamma^+N_e + C_{ji}^{-1}r_{i\gamma}^{(cx)}N_\gamma^+N_e \\ &= \mathcal{F}_{j\sigma}^{(\text{exc})}N_eN_\sigma + \mathcal{F}_{j\gamma}^{(\text{rec})}N_eN_\gamma^+ + \mathcal{F}_{j\gamma}^{(cx)}N_eN_\gamma^+, \end{aligned} \quad (2.52)$$

where  $\mathcal{F}$  is the effective contribution to  $N_j$  from excitation, recombination, charge exchange and ionisation. Note that the metastables of stage  $z$  are labelled  $\sigma$  and  $\rho$ , while those of stage  $z + 1$  are labelled  $\gamma$ .

In spectroscopic studies of a plasma, the line emissivity is of central importance. Widely used in astrophysical application, the method of differential emission measure (DEM) utilises the intensities of given lines to deduce plasma parameters. The intensity of a spectral line from a column of optically thin plasma of cross-sectional area  $A$ , due to transition from upper level  $j$  to lower level  $i$ , is given as,

$$I_{j \rightarrow i} = \frac{1}{4\pi A} \iiint A_{j \rightarrow i} N_j \, dx \, dy \, dz, \quad (2.53)$$

where the integral is over the volume of plasma viewed.

In DEM analysis, it is assumed that only contributions to the population of the excited state by excitation from the metastables from the same ionisation stage need be considered, so that equation 2.52 reduces to,

$$N_j = \mathcal{F}_{j\sigma}^{(\text{exc})}N_eN_\sigma. \quad (2.54)$$

The further assumption of ionisation balance is used, such that,

$$N_\sigma = \frac{N_\sigma}{N_{\text{tot}}} \frac{N_{\text{tot}}}{N_{\text{H}}} \frac{N_{\text{H}}}{N_e} N_e, \quad (2.55)$$

where it is assumed that the elemental abundance,  $N_{\text{tot}}/N_{\text{H}}$ , does not vary with depth in the line of sight. The spectral line intensity can then be written as,

$$I_{j \rightarrow i} = \frac{N_{\text{tot}}}{N_{\text{H}} 4\pi A} \iiint G_{j \rightarrow i}(T_e, N_e) N_e^2 dx dy dz, \quad (2.56)$$

where

$$G_{j \rightarrow i}(T_e, N_e) = A_{j \rightarrow i} \frac{N_{\text{H}}}{N_e} \mathcal{F}_{j\sigma}^{(\text{exc})} \frac{N_{\sigma}}{N_{\text{tot}}}, \quad (2.57)$$

usually called the contribution function, which embodies all of the relevant atomic physics and is highly peaked in temperature. It is convenient to change the variable of integration to electron temperature. To do this, the assumption that electron density is constant over the relatively small range of temperatures where  $G_{j \rightarrow i}(T_e, N_e)$  is significant is also made, reducing  $G$  to purely a function of  $T_e$ . This gives

$$I_{j \rightarrow k} = \frac{N_{\text{tot}}}{N_{\text{H}} 4\pi} \int G(T_e) \phi(T_e) dT_e, \quad (2.58)$$

where  $\phi(T_e)$  is the differential emission measure (DEM), defined by

$$\phi(T_e) = \frac{N_e^2}{A} S \frac{dh}{dT_e}, \quad (2.59)$$

where  $S$  is the projected area of the emitting volume and  $h$  is the column depth. The DEM relates to the amount of material in the temperature interval  $[T_e, T_e + dT_e]$  and the temperature gradient along the line of sight.

The reduction of  $G(T_e, N_e)$  to purely a function of temperature is not always appropriate. The following section investigates this in application to emission lines from Li-like ions abundant in the solar atmosphere.

## 2.3 Dynamic Plasmas

Continuing from the introduction to GCR modelling in section 2.2, two areas of interest from the upper solar atmosphere are examined. First, the well-known discrepancy between the intensity of Li-like lines to those of a similar formation temperature (Doyle and Raymond, 1984; Del Zanna *et al.* 2002) is analysed using the GCR approach; and, secondly, there is an investigation into ultraviolet explosive events, where evidence pointing to chromospheric origin is given.

### 2.3.1 Li-Like Ions in the Solar Atmosphere

The analysis of UV and EUV lines is essential for a proper understanding of high-temperature plasma, e.g. that found in the upper solar/stellar atmospheres. Data from spectrographs aboard the Solar and Heliospheric Observatory (SOHO; Domingo *et al.* 1995) has led to a wealth of observations of small-scale dynamic events observed from the Sun's chromosphere to the transition region and corona. On the stellar side, data from the International Ultraviolet Explorer (IUE), Space Telescope Imaging Spectrograph (STIS/HST) and the Far Ultraviolet Spectroscopic Explorer (FUSE) have all provided high quality data which have been used to diagnose properties of the atmospheres in a range of objects. Interpretation of these data is highly dependent on many atomic physics parameters, one of these being the ionisation fractions of the ion under consideration — see Young *et al.* (2003) for a discussion of some of these within the CHIANTI database.

It has been known for many years that lines from Li-like ions can, in some instances, give very different emission intensities from other isoelectronic sequences. Following on from work by Burgess and Summers (1969), Vernazza and Raymond (1979) showed that a significant increase in intensity can occur at high electron densities if one considers electron-density-dependent dielectronic recombination. In the vast majority of published ionisation fractions, the low-density assumption is used, and therefore use of these calculations to produce a differential emission measure (DEM) curve using a range of lines including Li-like ions can produce discrepant results (Doyle and Raymond, 1984; Del Zanna *et al.* 2002). In many instances, due to the limitation in the number of available spectral lines from IUE data, emission measure curves for stellar atmospheres have been derived based on data from Li-like ions, e.g. C IV 1548/50, N v 1328/42, etc.

The usual practice when considering atomic processes in high-temperature, low-density plasmas, such as discussed here, is to adopt the coronal approximation. The turbulent nature of the solar atmosphere often results in regions of relatively high density, however, so this approximation is not always valid. The work here, also published in Doyle *et al.* (2005b), considers the emission from a few diagnostically significant lines using a full density-dependent GCR treatment. The focus is on functions appropriate to solar observations: the contribution function and the radiative loss function, described in section 2.2.

The contribution function was determined at four values of the electron density corresponding to different solar regimes:  $10^6 \text{ cm}^{-3}$ , representing the low-density limit;  $10^9 \text{ cm}^{-3}$  for a typical quiet Sun electron density;  $10^{11} \text{ cm}^{-3}$  an active region; and  $10^{12} \text{ cm}^{-3}$  for a flare. These were calculated for four lines from

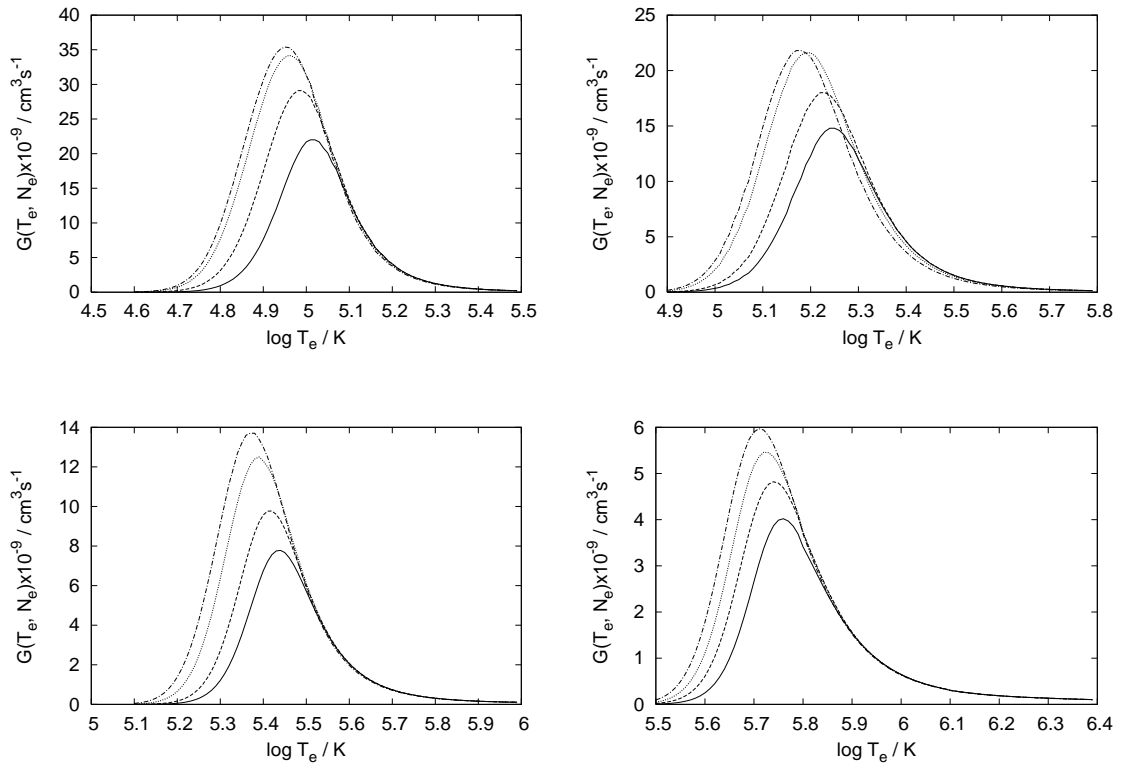


Figure 2.8: The contribution function for C IV 1548 Å, upper left; N V 1238 Å, upper right; O VI 1032 Å, lower left; and Ne VIII 770 Å, lower right. The solid line shows an electron density of  $10^6 \text{ cm}^{-3}$ ; the dashed line,  $10^9 \text{ cm}^{-3}$ ; the dotted line,  $10^{11} \text{ cm}^{-3}$ ; and the dot-dashed line,  $10^{12} \text{ cm}^{-3}$ .

Li-like ions (that are used for diagnostic application in SUMER (Solar Ultraviolet Measurements of Emitted Radiation; Wilhelm *et al.* 1995), namely C IV 1548 Å, N V 1238 Å, O VI 1032 Å and Ne VIII 770 Å. Results are shown in figure 2.8. It can be clearly seen that, with increasing density,  $G(T_e, N_e)$  shows a significant increase and the lines have their peak contribution shifted to lower temperature.

The variation of  $G(T_e, N_e)$  with density is a result of the shift in fractional abundance; the photon emissivity coefficient shows no significant density dependence over this range. Figures 2.9 and 2.10 show the ionisation and recombination coefficients, again for the C IV case although the results are applicable to each of the lines. It is clear that  $G(T_e, N_e)$  is affected more by recombination than ionisation, with the recombination coefficient showing a factor 4 reduction on going from  $10^6 \text{ cm}^{-3}$  to  $10^{12} \text{ cm}^{-3}$  while the ionisation coefficient shows only a factor 1.5 increase. The reduction of the recombination coefficient with density is due to dielectronic recombination being suppressed as collisional depopulation of the

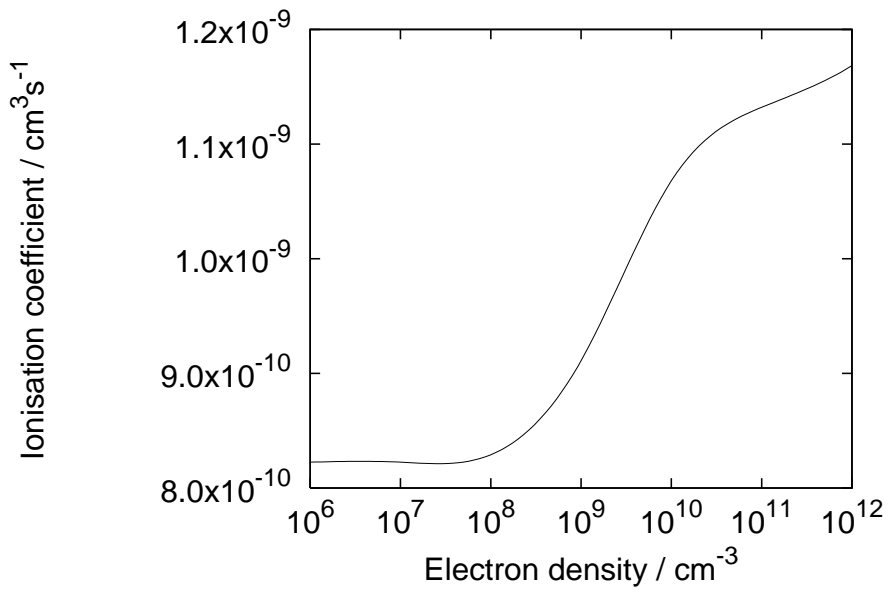


Figure 2.9: Ionisation coefficient for the ionisation of  $C^{2+}$  forming  $C^{3+}$  at an electron temperature of 100,000 K.

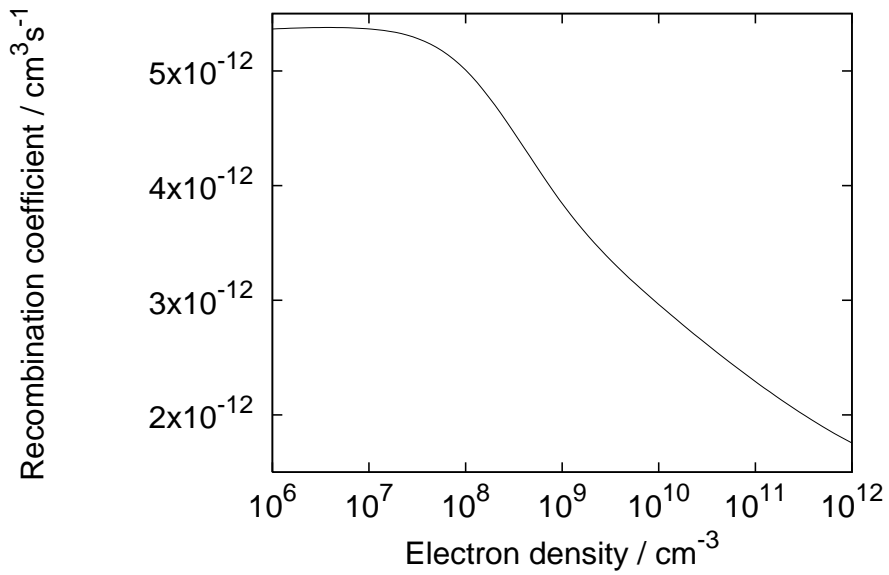


Figure 2.10: Recombination coefficient for the recombination of  $C^{3+}$  forming  $C^{2+}$  at an electron temperature of 100,000 K.

Line	$N_e = 10^6$	$N_e = 10^9$	$N_e = 10^{11}$	$N_e = 10^{12}$
C IV 1548 Å	1.00	1.59	2.93	3.45
N V 1238 Å	1.00	1.17	1.38	1.37
O VI 1032 Å	1.00	1.28	1.52	1.59
Ne VIII 770 Å	1.00	1.14	1.27	1.30

Table 2.1: The enhancement factor for the intensities of four lines from Li-like ions relative to the low-density value at  $N_e = 10^6 \text{ cm}^{-3}$ .

high  $n$ -shells, formed after stabilisation, takes effect. This results in the ionisation fractional abundance being shifted to lower temperature, and is reflected in the  $G(T_e, N_e)$  function.

Folding in the Raymond and Doyle (1981) DEM, the enhancement in intensity is calculated for the 4 lines at the given densities; table 2.1 shows the results. For C IV 1548 Å, a 60% enhancement is found for a density of  $10^9 \text{ cm}^{-3}$  as compared to  $10^6 \text{ cm}^{-3}$ , leading to over a factor of three enhancement for  $10^{12} \text{ cm}^{-3}$ . The increase is lower for the higher temperature lines, but still in the range of 30—60%.

The DEM analysis has been an important tool in the study of solar and stellar plasma over the past few decades. However, such an analysis can be suspect if the selection of lines are affected by opacity, inaccurate atomic coefficients (Lanzafame *et al.* 2002), or inappropriate assumptions concerning the calculation of the ionisation fractions (Vernazza and Raymond, 1979). It has been shown here that ignoring the density dependence of Li-like ions is unsound in the dynamic upper solar atmosphere.

Doyle and Raymond (1984) noted that N V and, to a lesser extent, O VI implied much larger values for the emission measure during the early stages of a large solar flare. For N V this amounted to a factor of 2 to 3. The present results go a long way to correcting this, with perhaps the remaining difference being due to temporal variability (i.e. there was a 2 minute time difference between the observation of the N V and the O V lines used in this particular study). From the results presented here, using the Raymond and Doyle (1981) DEM, the assumption that the low-density limit applies to Li-like ions leads to errors of up to factors of 2–3.

Focus is now turned to the radiated power as a function of density. With the exception of Landi and Landini (1999), all published radiative loss functions, in connection with the solar atmosphere, were calculated in the zero-density limit.

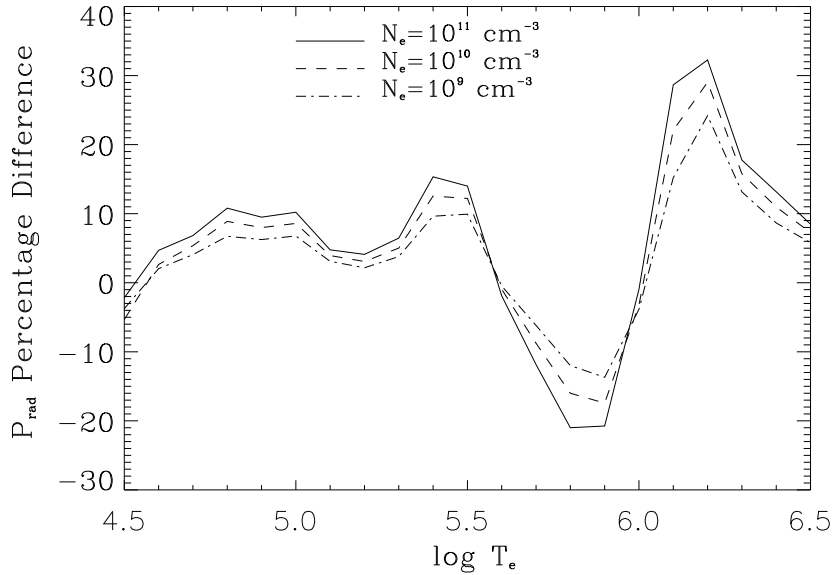


Figure 2.11: The percentage difference in the radiative loss function assuming different electron densities:  $10^6$  versus  $10^{11} \text{ cm}^{-3}$  (solid line)  $10^6$  versus  $10^{10} \text{ cm}^{-3}$  (dashed line),  $10^6$  versus  $10^9 \text{ cm}^{-3}$  (dot-dashed line).

Figure 2.11 shows the percentage difference,

$$\text{Diff} = \frac{P_{\text{rad}}(T_e, 10^6 \text{ cm}^{-3}) - P_{\text{rad}}(T_e, N_e)}{P_{\text{rad}}(T_e, 10^6 \text{ cm}^{-3})}, \quad (2.60)$$

for the radiative loss function at various densities. In the transition region, the difference is 10–20% while above  $10^6 \text{ K}$  the difference is around 30%. Although the detail of figure 2.11 differs from that of Landi and Landini (1999), the general result is similar. The differences are within the errors of the atomic data and, as pointed out by Landi and Landini, larger differences can arise from an incorrect treatment of the level populations or the use of different ionisation fractions, with the largest variation being due to elemental abundance.

### 2.3.2 Ultraviolet Explosive Events

Ultraviolet (UV) explosive events (EEs), often called bi-directional jets, were first discovered and classified as turbulent events by Brueckner and Bartoe (1983). They are characterised by highly non-Gaussian line profiles, showing Doppler shifts up to  $250 \text{ km s}^{-1}$  (Dere *et al.* 1989). Their average lifetime ranges from  $\sim 60$  to  $350 \text{ s}$  (Innes *et al.* 1997; Chae *et al.* 1998; Pérez *et al.* 1999), although

Dere (1994) observed bursts of up to 30 minutes in regions undergoing magnetic cancellation. Teriaca *et al.* (2004) estimate an average size of 1800 km. Birthrates over the entire Sun have been reported as  $600 \text{ s}^{-1}$  (Dere *et al.* 1989),  $3300 \text{ s}^{-1}$  (Ryutova and Tarbell, 2000) and  $2500 \text{ s}^{-1}$  (Teriaca *et al.* 2004).

Despite the many observations, there is still no firm understanding of UVEEs. In particular, there is dispute over where they form in the upper atmosphere. There have been a number of works that attempt to link transition region and coronal manifestations of the events. Madjarska and Doyle (2002) observed, using SUMER, the chromospheric Ly 6 (20,000 K) line and the transition region line S VI (200,000 K). They found a time delay in the response of the S VI line with respect to the Ly 6 line, suggesting the process that generates the event first occurs in the low chromosphere and is subsequently observed in transition region lines. There have also been attempts to observe the coronal counterparts to the jets (Dere, 1994; Moses and Cook, 1994; Teriaca *et al.* 2001). The latter work obtained data for an event in the transition region line N v 1238 Å, which also showed a small enhancement in the coronal line Mg x 625 Å. They conclude, however, that the enhancement in Mg x is due to the presence of a blend from a Si II line and that there is no obvious connection to the upper corona.

Doyle *et al.* (2003) have used non-Maxwellian electron distributions to explain EE observations by the TRACE (Transition Region and Coronal Explorer) imager (Handy *et al.* 1999). This work focuses on observations of an EE from SUMER, CDS (Coronal Diagnostic Spectrometer; Harrison *et al.* 1995) and TRACE, ranging from chromospheric to coronal temperatures. The EE is detected in the chromospheric and transition region lines of SUMER, but not the coronal line. There is, however, detection of lines of coronal temperature by the TRACE imager with the 171 Å filter. These authors explain this apparent discrepancy by suggesting that a non-Maxwellian electron distribution could result in the emission detected by TRACE being derived from a plasma at temperature  $\sim 800,000 \text{ K}$  as opposed to  $\sim 300,000 \text{ K}$ . Basing their study on the  $\kappa$  distribution, they find that distributions with  $\kappa = 2 - 10$  have the effect of lowering the temperature at which Fe IX lines are produced in detectable quantities from  $\sim 800,000 \text{ K}$  to  $\sim 300,000 \text{ K}$ .

The present analysis is concerned with a region showing prolonged EE activity in the transition region line N v 1238 Å, yet little evidence of such activity in another transition region line, O v 629 Å, observed simultaneously.

The observational data comes from part of a joint SUMER, CDS and TRACE study on 1999 June 1. The SUMER data set consists of Mg x 624.95 Å, O v 629.73 Å, N v 1238.82 Å, N v 1242.80 Å, C I 1249 Å and Si II 1251.16 Å, taken

between 09:13 UT and 11:01 UT with a 25 s exposure time. The data from CDS is of O v 629.73 Å, with two observations of 55 minutes each starting at 07:56 UT and 12:14 UT. The TRACE images discussed here were obtained starting at 09:02 UT and finishing at 12:00 UT. In addition to spectrographic data, three full-disc MDI (Michelson Doppler Interferometer; Scherrer *et al.* 1995) magnetograms were available, showing the EEs to appear in regions of mixed polarity weak fields.

From the data provided by these instruments, possible EEs are identified by examining in detail regions exhibiting large line widths, indicating Doppler broadening. Figure 2.12 shows images of the O v 629 Å and N v 1238 Å lines, where enhanced regions are those with larger widths. Highlighted, are five temporal locations, labelled (a), (b), (c), (d) and (e), that are distinguishable from the quiet Sun in terms of their line widths. Assuming the emission of the quiet Sun to be represented by a single Gaussian fit to its line profiles, Teriaca *et al.* (2004) identified potential EEs as areas where one of the fitting parameters deviates by more than  $3\sigma$  from its average distribution; this method is used here. In the N v profiles, these times indicated EE activity, with several of them indicating mass flows in excess of  $150 \text{ km s}^{-1}$  and increases in the line intensity sometimes exceeding the normal quiet Sun component. With exception of event (a), the O v line profiles fail to show similar evidence of large-scale EE activity. Instead, we see either none or, in some instances, only a minor indication of mass flows. Figures 2.13 and 2.14 show the profiles of event (b) in greater detail, where the N v profile shows a peak of over 600 cts/pixel in the blue-shifted plasma, compared to the 130 cts/pixel of the stationary component of the quiet Sun. The peak count rate is similar in the O v profile for both the quiet Sun and the EE.

Ionisation balance calculations, at a typical solar electron density of  $10^9 \text{ cm}^{-3}$ , give a peak formation temperature of  $\text{N}^{4+}$  at 200,000 K and  $\text{O}^{4+}$  at 250,000 K. The similar formation temperatures would suggest similar activity in these lines; an examination of the density dependence of these lines is used in an attempt to solve the discrepancy.

The  $G(T_e, N_e)$  functions, as described in section 2.2, are calculated for the O v 629 Å line — the  $1s^22s^2^1S - 1s^22s2p^1P$  transition — and for the N v 1238 Å line — the  $1s^22s^2S - 1s^22p^2P$  transition. Results are shown in figures 2.15 and 2.16. Three values of electron density are chosen:  $10^6 \text{ cm}^{-3}$  representing the zero density limit;  $10^9 \text{ cm}^{-3}$  for a typical quiet Sun electron density; and  $10^{11} \text{ cm}^{-3}$  for an active region.

With increasing electron density, both lines are seen to shift to lower temperatures. This is the effect of dielectronic recombination suppression, as discussed

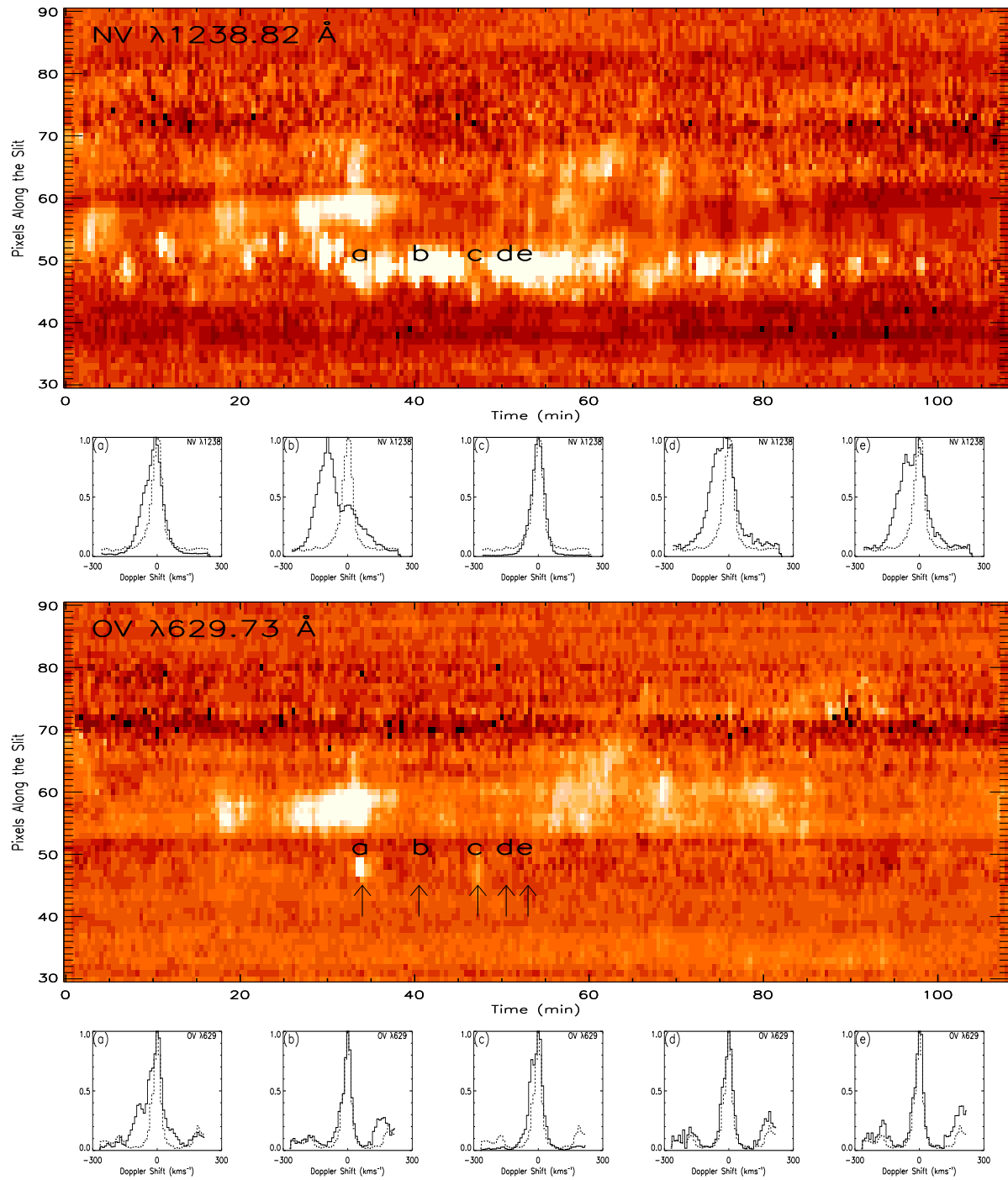


Figure 2.12: Time series image plots for O v 629 and N v 1238 over the whole duration of the dataset showing the variation in the line width assuming a single Gaussian fit. The data set was taken on 1999 June 1 starting at 09:13 UT. Below each image is shown the resulting line profile for both O v and N v taken at the same time for five different temporal locations (09:47, 09:53, 10:00, 10:03 and 10:05 UT) labelled (a), (b), (c), (d) and (e), normalised to unity. The quiet Sun profile is over-plotted for comparison (dashed line).

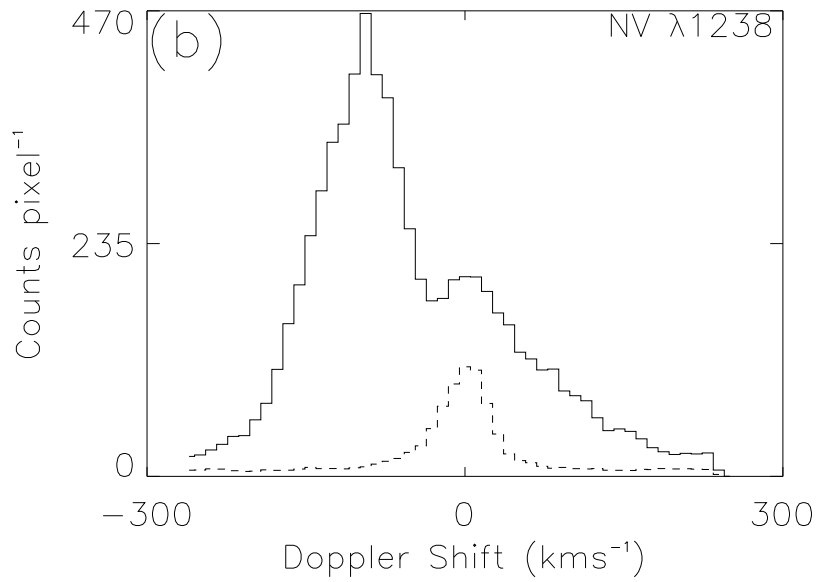


Figure 2.13: The N v 1238 Å line profile at 09:53 UT, i.e. event (b). The quiet Sun profile is over-plotted for comparison (dashed line).

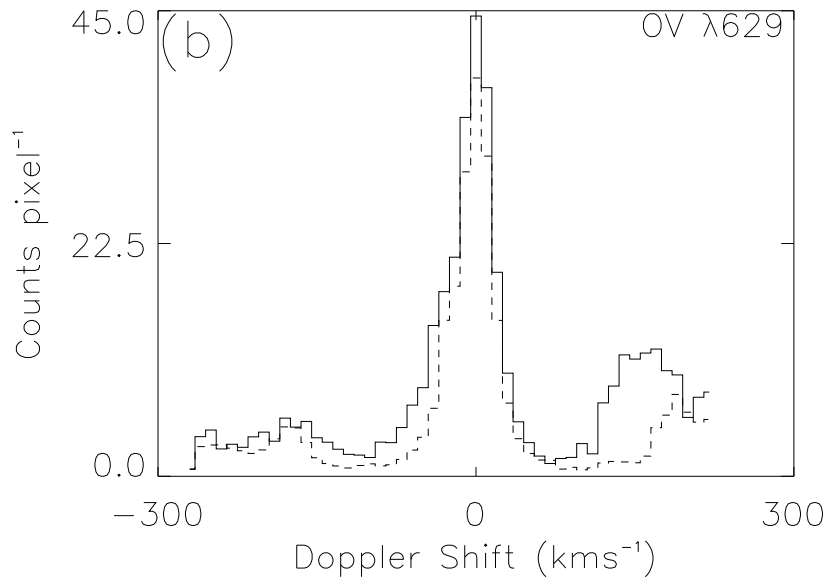


Figure 2.14: The O v 629 Å line profile at 09:53 UT, i.e. event (b). The Si II 1251 Å line can be seen to the red of the O v line. The quiet Sun profile is over-plotted for comparison (dashed line).

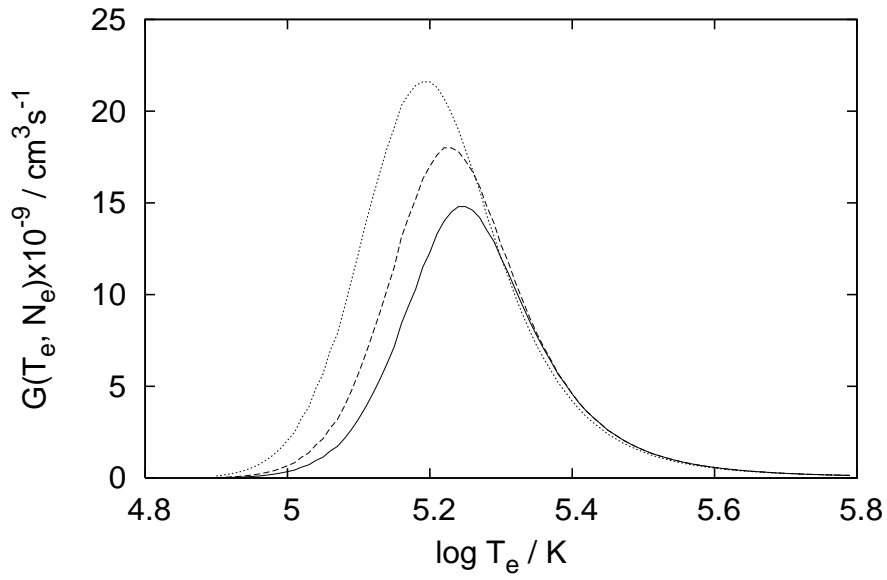


Figure 2.15: Contribution function of N v 1238 Å. The solid curve shows an electron density of  $10^6 \text{ cm}^{-3}$ ; the dashed curve,  $10^9 \text{ cm}^{-3}$ ; and the dotted curve,  $10^{11} \text{ cm}^{-3}$ .

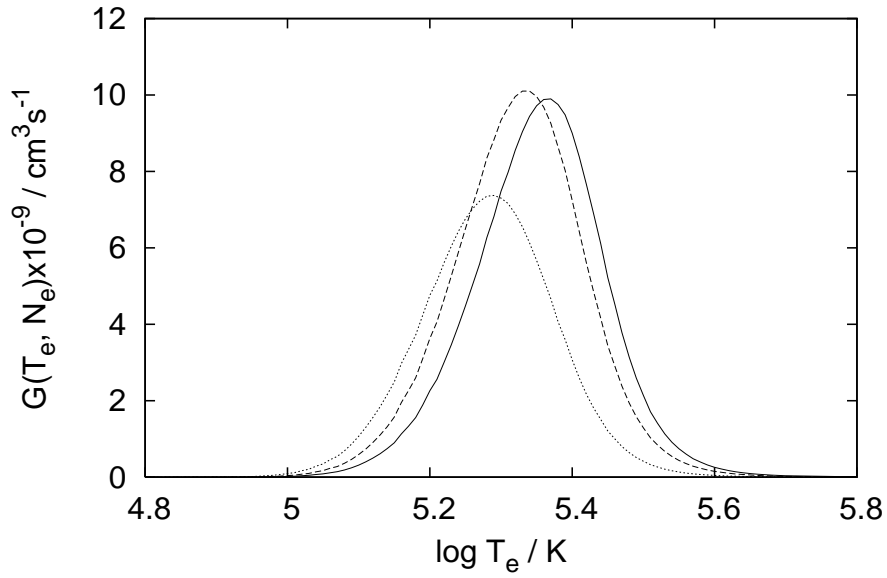


Figure 2.16: Contribution function of O v 629 Å. The solid curve shows an electron density of  $10^6 \text{ cm}^{-3}$ ; the dashed curve,  $10^9 \text{ cm}^{-3}$ ; and the dotted curve,  $10^{11} \text{ cm}^{-3}$ .

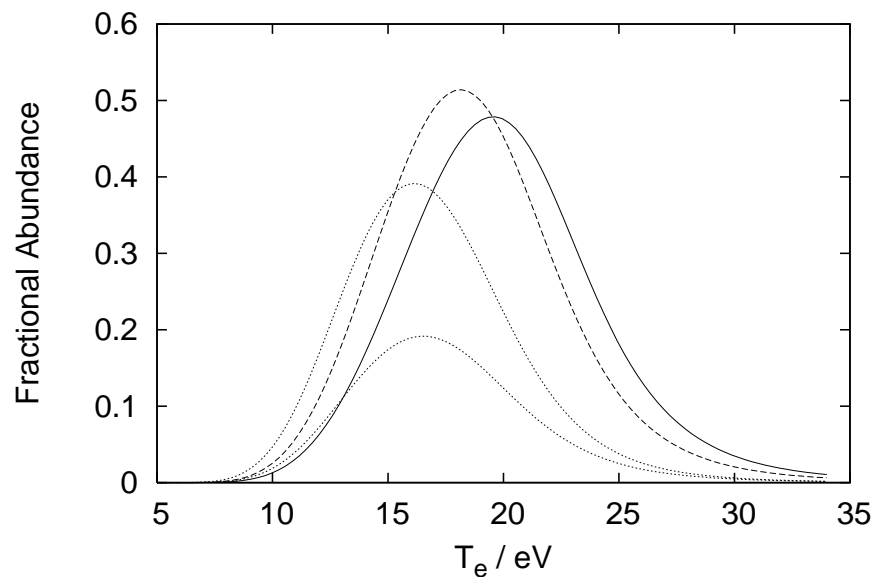


Figure 2.17: Fractional abundances of  $O^{4+}$  in the metastable term-resolved GCR picture. The solid line shows an electron density of  $10^6 \text{ cm}^{-3}$ ; the dashed line,  $10^9 \text{ cm}^{-3}$ ; and the dotted lines,  $10^{11} \text{ cm}^{-3}$ . The  $2s^2 \ ^1S$  ground and  $2s2p \ ^3P$  metastable terms are shown, although the metastable is completely suppressed at the lower two densities. For the electron density of  $10^{11} \text{ cm}^{-3}$ , the upper curve shows the ground term and the lower curve shows the metastable.

in section 2.3.1. The more interesting difference, however, is the variation in line flux with density. For N v, increasing the density from  $10^6$  to  $10^{11}$   $\text{cm}^{-3}$  results in a 60% increase in the line flux, while the O v line shows a 30% decrease. This decrease in the line flux can be explained by considering the relative populations of the metastable and ground terms of the  $\text{O}^{+4}$  ion. At low densities the metastable population is negligible, but, on increasing the density, the population becomes significant and acts as a sink to higher levels, thus causing the 629 Å transition to be depleted. Figure 2.17 shows the fractional abundance of the metastables of  $\text{O}^{4+}$  as a function of density. Li-like ions have no significant metastable, so similar behaviour is not displayed by the N v line.

A possible explanation for the lack of major activity in the O v line for events (b), (d) and (e) could be that EE (a) occurred in the lower chromosphere, thereafter, following an increase in the local electron density, the EEs are less visible in the O v line. This is consistent with the findings of Madjarska and Doyle (2002), who found time delays between the chromospheric and transition region lines in some EEs using high-cadence observations (10 s exposure time) obtained with the SUMER spectrometer in the Ly 6 (20,000 K) and S VI (200,000 K). This suggested that the process that generates these jets first occurs in the low chromosphere, although they are best observed in transition region lines.

Further evidence for the chromospheric nature of these events comes from the observed increase in the Si II 1251 Å line to the red of O v (see figures 2.12 and 2.14). Furthermore, as shown in figure 2.18, the chromospheric C I line also shows a peak in flux at these events. It is apparent that single temperature line profile information is not sufficient to clarify the nature of these events, and consideration of a full atomic model, including adequate representation of long-lived metastable states, is important.

The work presented in this section is published in Doyle *et al.* (2005a).

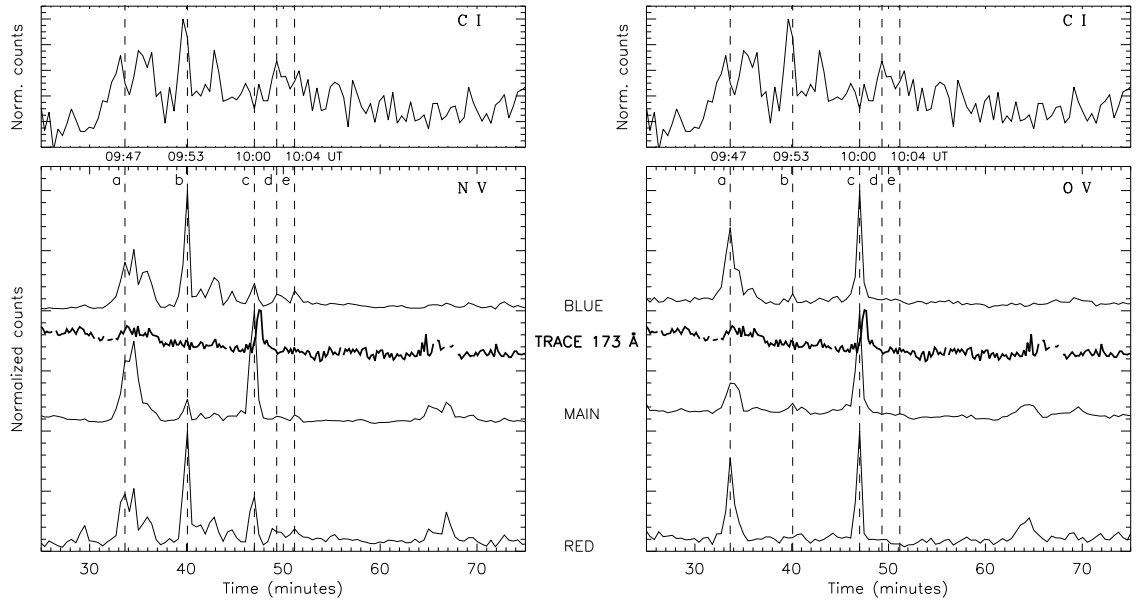


Figure 2.18: Normalised light curves for N v 1238 and O v 629 for the blue wing, red wing and main component, plus the corresponding TRACE 173 Å band and the weak C I 1249 line. The gaps in the TRACE light curve are missing data due to the presence of cosmic rays.

# Chapter 3

## Non-Maxwellian Modelling

The following chapter revisits the reaction rates described in section 2.1 from a non-Maxwellian viewpoint. Issues addressed in section 2.1 regarding resonant behaviour in collisional data are borne in mind. Application of the reaction rates (chapter 4) will be through the GCR model of section 2.2. Each of the free-electron-driven processes will be examined in turn, focusing on both the analytic formalisms and the nuances of numerical techniques involved in their solution. Consideration is also given to the distribution functions, which will be the starting point for calculation of the non-Maxwellian rates.

### 3.1 Distribution Functions

The primary goal of this work is to investigate the possibility of providing diagnostic measurements of the non-Maxwellian character of a plasma. By spectral analysis it is possible (for certain plasmas) to deduce the degree to which the distribution deviates from Maxwellian. Predictive modelling of the effects of a given distribution can also be explored by examination of how the degree of non-Maxwellian character influences spectral emission. For both of these purposes, it is helpful to introduce families of distribution functions with a parameter determining the deviation from Maxwellian. Not every plasma is adequately represented by one of these analytic families, so numerical distributions are also considered for predictive modelling, although the feasibility of deductive spectral analysis is hindered.

Whatever representation of the distribution is used, the present work considers only isotropic situations. This is acknowledged as a limitation of applicability, with many electron acceleration processes being directional — electrons in the atmospheres of Mars and Venus, for example, are believed to be accelerated par-

allel to the magnetic field direction (Shapiro *et al.* 1995; Bingham *et al.* 1997). Even in such cases, an isotropic approximation can often give insight into the primary effects of modified distribution function since electron isotropising (collisions primarily with ions) and thermalising (collisions primarily with electrons) have different timescales. While the techniques described here for generating non-Maxwellian distribution functions and processing them through to rate coefficients hold for any distribution, progression to such deliverables as photon emissivity coefficients and ionisation balance would require considerable alteration of the GCR modelling to allow for anisotropic distributions.

### 3.1.1 Analytic Distributions

Distribution functions,  $f(E)$ , as implemented here, will be defined in terms of electron kinetic energy and will be normalised such that  $\int f(E) dE = 1$ . The mean energy,  $\bar{E}$ , and variance,  $\sigma_f$ , of the distribution are given by,

$$\bar{E} = \int E f(E) dE, \quad (3.1)$$

and

$$\sigma_f = \int (E - \bar{E})^2 f(E) dE. \quad (3.2)$$

The concept of temperature is only valid for a Maxwellian distribution. The extension of this notion to non-Maxwellian distributions is by defining an ‘effective’ temperature,  $T_{\text{eff}}$ , whereby  $kT_{\text{eff}} = 2\bar{E}/3$ . The Maxwellian distribution is written as,

$$f_{T_e}(E) = \frac{1}{kT_e} \frac{2}{\sqrt{\pi}} \left( \frac{E}{kT_e} \right)^{1/2} \exp \left( -\frac{E}{kT_e} \right), \quad (3.3)$$

where the effective temperature is equivalent to the well-recognised electron temperature,  $T_e$ . Note also that  $\bar{E} = 3kT_e/2$  and  $\sigma_f = kT_e$ .

#### 3.1.1.1 The $\kappa$ Distribution Family

Common non-Maxwellian situations, particularly of astrophysical plasmas, are over-population of a high-energy Maxwellian tail. Vasyliunas (1968) introduced the  $\kappa$  distribution (also known as the generalised Lorentzian) as an analytical representation of the electrons in the magnetosphere as measured by satellites OGO 1 and OGO 3.

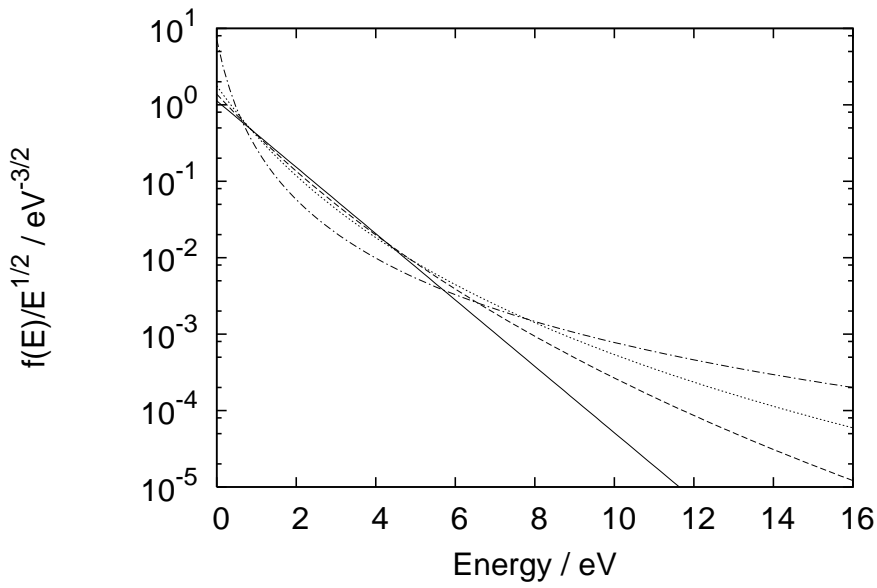


Figure 3.1:  $\kappa$  distribution for various  $\kappa$  values, and a comparison to a Maxwellian for an (effective) electron temperature of 1 eV. The solid line denotes the Maxwellian distribution ( $\kappa \rightarrow \infty$ ), the dashed line  $\kappa = 10$ , the dotted line  $\kappa = 5$  and the chained line  $\kappa = 2$ .

The  $\kappa$  family takes the form,

$$f_{\kappa, E_\kappa}(E) = \frac{1}{E_\kappa} \frac{2}{\sqrt{\pi}} \left( \frac{E}{E_\kappa} \right)^{1/2} \kappa^{-3/2} \frac{\Gamma(\kappa + 1)}{\Gamma(\kappa - \frac{1}{2})} \left( 1 + \frac{E}{\kappa E_\kappa} \right)^{-(\kappa+1)}. \quad (3.4)$$

The distribution is parameterised by  $\kappa$  and has a characteristic energy  $E_\kappa$ , such that the mean energy is given by,

$$\bar{E} = \frac{3}{2} \frac{\kappa E_\kappa}{\kappa - 3/2}, \quad (3.5)$$

and the variance by,

$$\sigma_f = \frac{\kappa E_\kappa}{\kappa - 3/2}. \quad (3.6)$$

The parameter  $\kappa$  takes values in the range  $(3/2, \infty)$  and determines the deviation from a Maxwellian of temperature  $T_{\text{eff}}$ , with the  $\kappa$  distribution tending to Maxwellian as  $\kappa \rightarrow \infty$ . Figure 3.1 illustrates the behaviour of the function for various  $\kappa$  values at an effective temperature of 1 eV, with the limiting Maxwellian shown for comparison.

The  $\kappa$  distribution has been used extensively to analyse spacecraft data since its inception by Vasyliunas (1968). The magnetospheric plasma sheet is an area

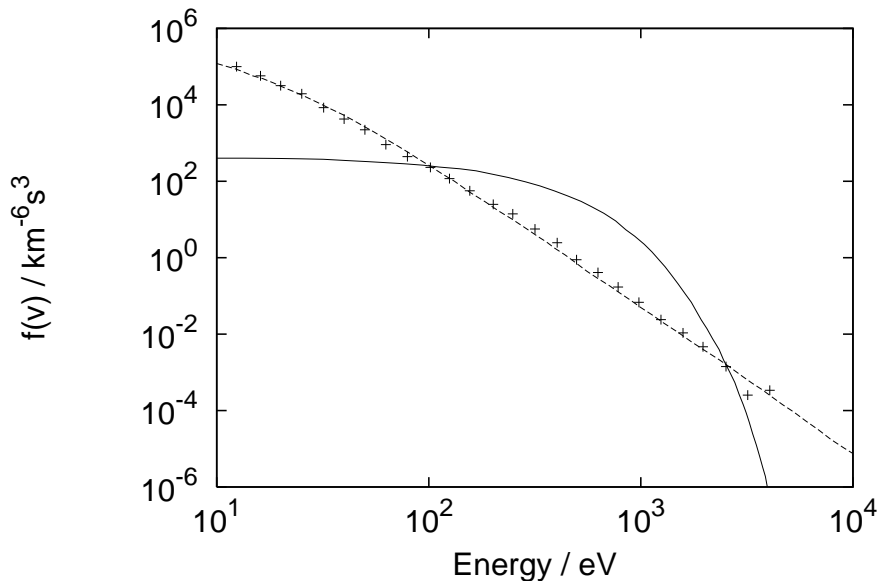


Figure 3.2: Solar wind electron velocity distribution as measured at 1000 UT on 21 October 1984 by the AMPTE UKS spacecraft (Bryant, 1996; crosses). Also shown is the best-fitting  $\kappa$  distribution ( $\kappa = 2.9$ ; dotted line) and a Maxwellian for comparison (solid line). Both curves are at an effective temperature of 7.5 eV.

that has received particular interest over the years; Vasyliunas found distributions with  $\kappa$  ranging from 2 to 6, leading other authors (Lui and Krimigis, 1981; Williams *et al.* 1988; Christon *et al.* 1988; etc.) to use a similar representation of the distribution. Bryant (1996) found values of  $\kappa$  in the range 2.5–4.5 matched the solar wind observations from the AMPTE UKS spacecraft, and others have used the  $\kappa$  distribution when modelling atmospheres of Jupiter (Leubner, 1982) and Saturn (Armstrong *et al.* 1983). Leubner (2001) has also shown, through Fokker-Planck simulations (see also, section 3.1.2.2), that the  $\kappa$  distribution can occur in auroral electrons. Other studies, e.g. by Hasegawa *et al.* (1985), show that such a distribution can result in plasmas immersed in a suprathermal radiation field. Figure 3.2 shows an example of observations of the solar wind electron distribution being well matched by a  $\kappa$  distribution (Bryant, 1996).

### 3.1.1.2 Druyvesteyn Distribution Family

If the  $\kappa$  distribution is the analytical paradigm of distributions displaying an increase of the high-energy tail compared to a Maxwellian, then the equivalent of distributions with a depleted high-energy tail is the generalised Druyvesteyn distribution. The Druyvesteyn (1930) distribution was derived from elastic scat-

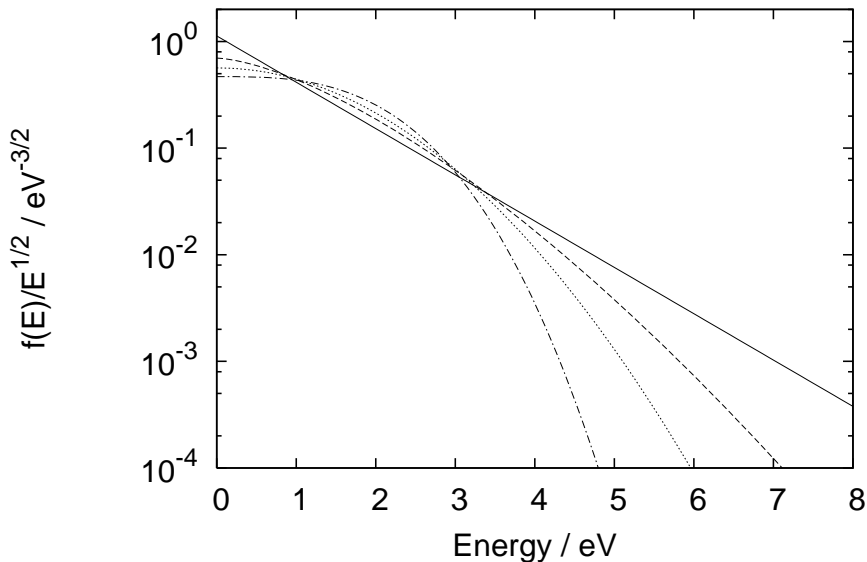


Figure 3.3: Druyvesteyn distribution for various values of characterising parameter  $x$ , and a comparison to a Maxwellian for an (effective) electron temperature of 1 eV. The solid line denotes the Maxwellian distribution ( $x = 1$ ), the dashed line denotes  $x = 1.5$ , the dotted line  $x = 2$  and the chained line  $x = 3$ .

tering models of the electrons in a low-pressure gas discharge. Generalisation to include inelastic processes (Behringer and Fantz, 1994) has led to the generalised Druyvesteyn family,

$$f_{x,E_x}(E) = \frac{x}{E_x^{3/2}} \frac{\Gamma(5/2x)^{3/2}}{\Gamma(3/2x)^{5/2}} E^{1/2} \exp\left(-\left[\frac{E\Gamma(5/2x)}{E_x\Gamma(3/2x)}\right]^x\right). \quad (3.7)$$

The characteristic energy of the distribution is  $E_x = \bar{E}$ . The distribution is equivalent to a Maxwellian when the characterising parameter  $x = 1$  and the original Druyvesteyn distribution is with  $x = 2$ . Figure 3.3 illustrates the behaviour of the function for various  $x$  values at an effective temperature of 1 eV, with the limiting Maxwellian shown for comparison.

Electron distribution functions in gas discharges have been studied by many authors. For example: Nighan (1970), Winkler and Pfau (1973) and Loureiro and Ferreira (1986, 1989) for nitrogen, Gudmundsson *et al.* (2000) for oxygen, Gudmundsson *et al.* (1999) for an Ar/O<sub>2</sub> mixture, while Winkler (1993) and Capitelli *et al.* (1993) provide a general overview. Energetic electrons in the discharge are lost rapidly by diffusion to the walls, resulting in a distribution function that typically displays a depleted high-energy tail. The Druyvesteyn

distribution family has been used to fit measurements of electron distribution functions in gas discharges by Behringer and Fantz (1994). For a discharge of molecular nitrogen, they found that the distribution is best represented by a sum of two Druyvesteyn distributions so as to adequately match both high- and low-energy behaviour. The high-energy part of the distribution is well represented by a Druyvesteyn with parameter  $x$  in the range 1.6–2.2. The low-energy part is closely matched by a Druyvesteyn with  $x = 3.5$ . Behringer and Fantz (1994) also represented the distribution measured in a discharge of a noble gas mixture with similar results. For a discharge comprised of helium, argon and nitrogen they suggest  $x = 1.8$  at a pressure of 1000 Pa and  $x = 2.9$  at 200 Pa.

Gudmundsson (2001) also modelled discharge plasmas (of argon) using the Druyvesteyn distribution. This work begins by postulating values of  $x$  likely to characterise distributions of the plasma and investigates the effect varying  $x$  has on the plasma parameters. The effective electron temperature is found to increase and the electron density decrease as the distribution varies from Maxwellian to Druyvesteyn with  $x = 2$ .

### 3.1.2 Numerical Distributions

The analytic distribution functions described above are simplified representations of the actual distributions of real plasmas, allowing consequential analysis to proceed smoothly. It can be the case, however, that the distribution function cannot be satisfactorily approximated by any of the analytic expressions; one then resorts to numerically tabulated distributions. Described here are two methods used to generate non-Maxwellian distributions with application to astrophysical plasmas. The practical implementation is discussed in section 4.2.

#### 3.1.2.1 Darwin Particle-In-Cell Method

The evolution of particle distributions in a plasma can be described by the Vlasov equation,

$$\frac{\partial}{\partial t} f(\mathbf{r}, \mathbf{v}, t) + \mathbf{v} \cdot \nabla f(\mathbf{r}, \mathbf{v}, t) + \frac{q}{m} (\mathbf{E} + \mathbf{v} \times \mathbf{B}) \cdot \nabla_v f(\mathbf{r}, \mathbf{v}, t) = 0, \quad (3.8)$$

where the distribution is a function of position  $\mathbf{r}$ , velocity  $\mathbf{v}$ , and time  $t$ ; and is influenced by the Lorentz force, where  $q$  and  $m$  are the particle charge and mass,  $\mathbf{E}$  is the electric field, and  $\mathbf{B}$  the magnetic field. The Vlasov equation is a simplification in that the effects of collisions due to nearby particles are ignored. Rather, the limit as the number of particles in a Debye sphere tends to infinity

is taken and the distribution of particles is a smooth function of phase space. Further simplification to the model considers the electrons to display collective behaviour and neglects the individuality of the particles. Taking moments of the Vlasov equation yields the fluid equations describing density, average velocity and average energy. Note that there is no longer information on these quantities as a function of phase space.

In theory, computer simulations of plasmas would numerically integrate the equations of motion of all the particles moving in fields governed by Maxwell's equations. In practice, the large number of particles prohibits such a treatment and simplifying assumptions must be made. There exist several methods of reducing the complexity of the problem, the choice of which is driven by the phenomena under study. The numerical plasma simulation codes discussed here rely on two approximations, namely the PIC (particle-in-cell) approximation and the Darwin approximation (a comprehensive overview of all the methods discussed here can be found in Birdsall and Langdon, 1985).

The essence of PIC modelling (introduced by Yu *et al.* 1965 and Hockney, 1965, 1966) is the discretisation of space and time. The particles are modelled individually, each having its own position and velocity at every time step, which change according to the electromagnetic forces on the particles. The magnetic and electric fields are stored on the spatial grid and advanced according to Maxwell's equations.

The time cycle follows four basic stages at each time step:

- the charge and current densities are found at the discrete grid points from the particle positions and velocities (which may take all values in phase space)
- using these sources, integrate the field equations on the grid
- interpolate the fields from the grid to the particles, applying a force at each particle
- calculate resultant position and velocity of the particle by integrating the equations of motion.

Examination of the physical manifestations of the model will almost always require a large number of these cycles; at issue is how to make the time step as large as possible without causing the numerics to break down.

The 'standard' hybrid code (Thomas and Birdsall, 1980) uses the PIC approximation for ions but treats the electrons as a fluid. It also treats the electrons

as massless, reducing the number of terms in the Vlasov equation that need be considered. Low-frequency plasma modes have been eliminated by the approximations enabling a large time step to be used. Extensions to this method have included massive electrons, which reduce the time step but gives better insight to certain physical phenomena. Assuming fluid electrons implies an unchanging Maxwellian distribution, a prohibited simplification for the present work where electron acceleration systems are of concern. A PIC representation of both ions and electrons must be included.

As well as methods of representing particles and following their orbits, one must also be concerned with the electromagnetic field evolution. The present work implements the Darwin approximation (Darwin, 1920; Kaufman and Rostler, 1971; Nielson and Lewis, 1976; Busnardo-Neto *et al.* 1977; Hewett and Nielson, 1978; Hewett, 1985), which splits the electric field into transverse and longitudinal parts and neglects the transverse part since it is only significant for high-frequency waves, which are of little interest. Maxwell's equations, in this limit, reduce to,

$$\nabla \cdot \mathbf{E}_l = 4\pi\rho \quad (3.9)$$

$$\nabla \times \mathbf{E} = -\frac{1}{c} \frac{\partial \mathbf{B}}{\partial t} \quad (3.10)$$

$$\nabla \cdot \mathbf{B} = 0 \quad (3.11)$$

$$\nabla \times \mathbf{B} = \frac{4\pi}{c} \mathbf{J}_t, \quad (3.12)$$

where  $\rho$  is the charge density,  $\mathbf{J}_t$  is the transverse part of the current density and  $\mathbf{E}_l$  is the longitudinal part of the electric field. The physical significance of this magnetoinductive limit is that purely electromagnetic modes are eliminated while electrostatic and low-frequency inductive electric fields are retained. The benefit of this is realised by considering the CFL (Courant-Friedrichs-Levy) condition (Richtmyer and Morton, 1967) on the discretisation of space and time. This constraint implies that explicit integration of Maxwell's partial differential equations will be stable as long as electromagnetic waves do not propagate more than the smallest grid spacing in a time step. By eliminating electromagnetic modes, the Darwin limit permits a large time step.

Presented here are the results of a PIC Darwin code as applied to the interaction between the ionospheres of Mars and Venus and the solar wind. Because Mars and Venus do not possess a significant intrinsic magnetic field, the solar wind impinges directly on the planetary ionospheres. The counter-streaming plasmas of the solar wind and the plasma mantle result in the modified two-stream instability (MTSI; Sagdeev *et al.* 1990; Shapiro *et al.* 1995), exciting waves to a

few times above the lower hybrid frequency. These waves can cause significant electron acceleration and heating. It is postulated (Bingham *et al.* 1997; Shapiro *et al.* 1999) that these fast electrons can result in strong x-ray emission by colliding with ionospheric ions. Indeed, x-ray emission has been observed from the atmospheres of both Mars and Venus by the Chandra satellite (Dennerl, 2002; Dennerl *et al.* 2002).

Models with relative motion between two sets of charged particles date as far back as Pierce (1948) and Haeff (1949), and were followed by a detailed study of the nonlinear effects of streaming instabilities by Dawson (1962). Previous simulations (Quest *et al.* 1997; Szegö *et al.* 1997; Dobé *et al.* 1999), using a hybrid code with a fluid description of electrons, showed that nonlinear development of the MTSI within the plasma mantle can effect strong coupling between the ion species. Extension of these codes (Quest, unpublished), with a PIC representation of electrons, allowed the kinetic evolution of the electrons to be followed. The code simulates the interaction as a solar wind comprising of protons streaming through an ionosphere consisting of oxygen ions; plasma measurements at Mars by Phobos 2 record oxygen as the most abundant element (Sagdeev and Zakharov, 1989; Dubinin *et al.* 1997). Electrons are also present in the model with two initial temperatures, 33 eV to represent the solar wind and 1 eV to represent the ionosphere (Krasnopolsky, 1975; Cloutier *et al.* 1993; Spenner *et al.* 1995). The simulation typically consists of  $4 \times 10^6$  particles,  $6 \times 10^5$  time steps and 512 spatial cells, although this depends on the proton to electron mass ratio. As a proper ratio of 1836 was not possible due to computational time constraints, a ratio of 100 was used for an initial run. Figure 3.4(a) shows the evolution of the electron distribution function in this case. The accelerated electrons for this run do not possess energies high enough to coincide with the theoretical predictions, nor to contribute to the observed x-ray emission. A larger mass ratio of 400 produced the results of figure 3.4(b), showing accelerated electrons of sufficient energy to fit predictions (Bryans *et al.* 2003).

### 3.1.2.2 Fokker-Planck Method

It is apparent that PIC codes, as described above, can be computationally demanding. An alternative numerical plasma simulation method is to monitor the evolution of the electron distribution function as a whole rather than integrating the effects of each individual particle. Focus here, is on Landau damping of lower-hybrid waves (Fisch, 1978; Fisch and Boozer, 1980), of which there is considerable interest in astrophysical regimes (Bingham *et al.* 1984, 1988; Retterer *et al.* 1986;

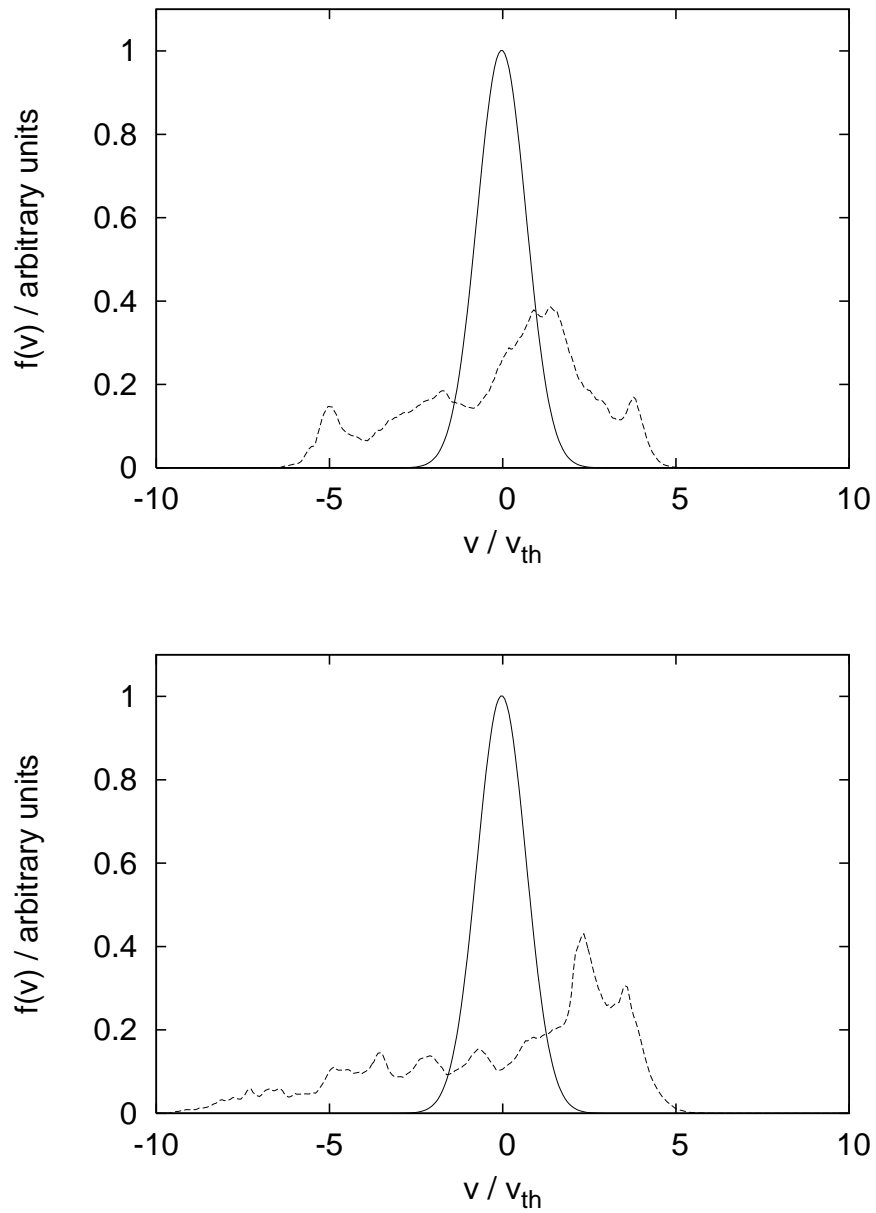


Figure 3.4: Electron velocity distribution (dashed curve) in the direction of the magnetic field as generated by PIC Darwin code. The upper plot shows the results with a proton to electron mass ratio of 100, and the lower with a ratio of 400. Velocity is in units of original electron thermal velocity. The original Maxwellian distribution function (solid curve) is plotted for reference.

Bryant *et al.* 1991; Bryant, 1992). Such electrostatic waves propagate parallel to a magnetic field and, if moving with a velocity  $v = \omega/k$  in a plasma, will be travelling at the same velocity as some of the electrons. It is possible for the wave to transfer energy to these electrons and vice versa. The direction of energy transfer depends on the first derivative of the electron distribution function with respect to velocity in the direction parallel to the magnetic field. If  $\partial f/\partial v_{\parallel} < 0$ , electrons will be energised and the waves will be damped, and if  $\partial f/\partial v_{\parallel} > 0$ , the waves will grow and the electrons decelerate. If  $\partial f/\partial v_{\parallel} = 0$  then there is no energy transfer. Therefore, in the absence of electron collisions, the lower-hybrid waves will cause a plateau region to be formed in the electron velocity distribution in one direction. This can be described by the Fokker-Planck equation:

$$\left(\frac{\partial f}{\partial t}\right)_{\omega} = \frac{\partial}{\partial v_{\parallel}} \left( G(v_{\parallel}) \frac{\partial f}{\partial v_{\parallel}} \right), \quad (3.13)$$

where  $G(v_{\parallel})$  is a normalised wave diffusion operator. Dendy *et al.* (1995) solved equation 3.13 for the case of a Gaussian power spectrum,

$$G(v_{\parallel}) = \frac{\pi^{1/2}}{\omega \nu_{ei}} \left| \frac{eE}{mv_{th}} \right|^2 \frac{v_{\parallel}}{\Delta} \exp \left[ -\frac{(v_{\parallel} - v_0)^2}{\Delta^2} \right], \quad (3.14)$$

where  $\omega$  is the wave frequency,  $\nu_{ei}$  is the electron-ion collision rate,  $v_{th}$  is the thermal speed,  $\Delta$  is the half-width of the wave power spectrum, centred at  $v_0$ . The work of Dendy *et al.* has been continued here using Maxwellian and other initial distribution functions. Figure 3.5 shows a contour plot of the evolved distribution function from an initial Maxwellian, after 3 ms, in the  $v_{\perp}$  and  $v_{\parallel}$  plane with respect to a magnetic field in the parallel direction. Parameters used in the calculation of figure 3.5 are typical of electrons in the auroral zone as measured by Mozer *et al.* (1980) and Pottellette *et al.* (1992). It is assumed that the plasma is collisionless. The resulting distribution is non-isotropic: the symmetry in the  $v_{\parallel}$  direction has been broken, although the distribution is still symmetrical around all azimuthal angles. For calculating atomic collision rates one should properly use differential cross sections, but here the distribution function is integrated over the pitch ( $\phi$ ) and azimuthal ( $\theta$ ) angles to give a simple distribution over speed (energy), which is then tabulated (see section 4.2).

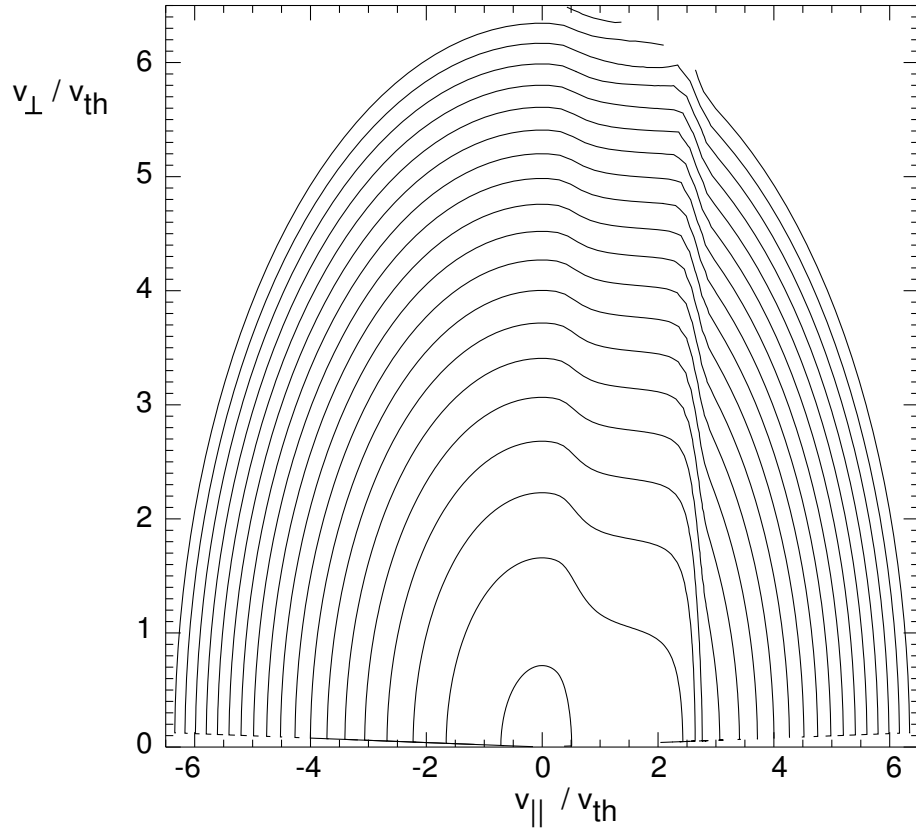


Figure 3.5: Contour plot of an initial Maxwellian at  $T_e = 1$  keV evolving for 3 ms in a lower-hybrid Gaussian wave field of strength 40 mV/m centred on wave velocity  $v_0 = 1.5v_{th}$  with half-width of  $\Delta = 0.5v_{th}$ .

## 3.2 Non-Maxwellian Rate Coefficients

### 3.2.1 Collisional Excitation and De-Excitation

For Maxwellian electron distributions, the collision strength describing electron impact excitation between lower state  $i$  and upper state  $j$  (equation 2.1) averaged over the distribution is the usual tabulation, given by  $\Upsilon_{ij}(T_e)$  (see equation 2.3).  $\Omega_{ij}$  is symmetric between  $i$  and  $j$  from microreversibility and, likewise, in the Maxwellian case, so is  $\Upsilon_{ij}$  from detailed balance. Thus, both the excitation and de-excitation rate coefficients can be obtained from  $\Upsilon_{ij}$  via equations 2.4 and 2.5.

For the non-Maxwellian case, equation 2.3 must be replaced by an average over a general distribution function, defined such that the conversion to rate coefficient remains as it was in the Maxwellian case. Lack of detailed balance breaks the symmetry of the Maxwellian effective collision strength, leading to the requirement of an effective collision strength for excitation and also, separately, for de-excitation. We call these effective collision strengths *Upsilon* and *Downsilon* respectively. On generalising equations 2.4 and 2.5, they are given by,

$$\Upsilon_{i \rightarrow j}(T_{\text{eff}}) = \frac{\omega_i}{2\sqrt{\pi}\alpha c a_0^2} \left( \frac{kT_{\text{eff}}}{I_{\text{H}}} \right)^{1/2} \exp\left(\frac{\Delta E_{ij}}{kT_{\text{eff}}}\right) q_{i \rightarrow j}(T_{\text{eff}}), \quad (3.15)$$

and

$$\mathcal{J}_{j \rightarrow i}(T_{\text{eff}}) = \frac{\omega_j}{2\sqrt{\pi}\alpha c a_0^2} \left( \frac{kT_{\text{eff}}}{I_{\text{H}}} \right)^{1/2} q_{j \rightarrow i}(T_{\text{eff}}). \quad (3.16)$$

For a general electron energy distribution,  $f(\varepsilon)$ , the excitation and de-excitation rate coefficients are given by,

$$q_{i \rightarrow j}(T_{\text{eff}}) = \sqrt{\frac{2}{m_e} \frac{\pi a_0^2}{\omega_i}} I_{\text{H}} \int_0^{\infty} \Omega_{ij}(\varepsilon_i) \varepsilon_i^{-1/2} f(\varepsilon_i) d\varepsilon_j, \quad (3.17)$$

and

$$q_{j \rightarrow i}(T_{\text{eff}}) = \sqrt{\frac{2}{m_e} \frac{\pi a_0^2}{\omega_j}} I_{\text{H}} \int_0^{\infty} \Omega_{ij}(\varepsilon_j) \varepsilon_j^{-1/2} f(\varepsilon_j) d\varepsilon_j, \quad (3.18)$$

which leads to

$$\Upsilon_{i \rightarrow j}(T_{\text{eff}}) = \frac{\sqrt{\pi}}{2} \exp\left(\frac{\Delta E_{ij}}{kT_{\text{eff}}}\right) \int_0^{\infty} \Omega_{ij}(\varepsilon_i) \left(\frac{\varepsilon_i}{kT_{\text{eff}}}\right)^{-1/2} f(\varepsilon_i) d\varepsilon_j, \quad (3.19)$$

and

$$\mathcal{J}_{j \rightarrow i}(T_{\text{eff}}) = \frac{\sqrt{\pi}}{2} \int_0^{\infty} \Omega_{ij}(\varepsilon_j) \left( \frac{\varepsilon_j}{kT_{\text{eff}}} \right)^{-1/2} f(\varepsilon_j) d\varepsilon_j. \quad (3.20)$$

As described in section 3.1.1, two analytic functional forms and a numerical distribution function are considered. The solution of equations 3.19 and 3.20 are treated separately for these cases.

For the  $\kappa$  distribution, equations 3.19 and 3.20 become,

$$\begin{aligned} \Upsilon_{i \rightarrow j}^{\kappa}(T_{\text{eff}}) &= \sqrt{\frac{2\kappa}{2\kappa-3}} \kappa^{-3/2} \frac{\Gamma(\kappa+1)}{\Gamma(\kappa-\frac{1}{2})} \exp\left(\frac{\Delta E_{ij}}{kT_{\text{eff}}}\right) \\ &\times \int_0^{\infty} \Omega_{ij} \left[ 1 + \frac{\varepsilon_j + \Delta E_{ij}}{\kappa E_{\kappa}} \right]^{-(\kappa+1)} d\left(\frac{\varepsilon_j}{E_{\kappa}}\right), \end{aligned} \quad (3.21)$$

and

$$\begin{aligned} \mathcal{J}_{j \rightarrow i}^{\kappa}(T_{\text{eff}}) &= \sqrt{\frac{2\kappa}{2\kappa-3}} \kappa^{-3/2} \frac{\Gamma(\kappa+1)}{\Gamma(\kappa-\frac{1}{2})} \\ &\times \int_0^{\infty} \Omega_{ij} \left[ 1 + \frac{\varepsilon_j}{\kappa E_{\kappa}} \right]^{-(\kappa+1)} d\left(\frac{\varepsilon_j}{E_{\kappa}}\right). \end{aligned} \quad (3.22)$$

For the Druyvesteyn distribution one arrives at,

$$\begin{aligned} \Upsilon_{i \rightarrow j}^D(T_{\text{eff}}) &= \sqrt{\frac{\pi}{6}} x \frac{\Gamma(5/2x)^{3/2}}{\Gamma(3/2x)^{5/2}} \exp\left(\frac{\Delta E_{ij}}{kT_{\text{eff}}}\right) \\ &\times \int_0^{\infty} \Omega_{ij} \exp\left(-\left[\frac{(\varepsilon_j + \Delta E_{ij})\Gamma(5/2x)}{E_x \Gamma(3/2x)}\right]^x\right) d\left(\frac{\varepsilon_j}{E_x}\right), \end{aligned} \quad (3.23)$$

and

$$\begin{aligned} \mathcal{J}_{j \rightarrow i}^D(T_{\text{eff}}) &= \sqrt{\frac{\pi}{6}} x \frac{\Gamma(5/2x)^{3/2}}{\Gamma(3/2x)^{5/2}} \\ &\times \int_0^{\infty} \Omega_{ij} \exp\left(-\left[\frac{\varepsilon_j \Gamma(5/2x)}{E_x \Gamma(3/2x)}\right]^x\right) d\left(\frac{\varepsilon_j}{E_x}\right). \end{aligned} \quad (3.24)$$

Since we have an analytic description of the distribution function and the collision strength tabulated as a function of energy, only the form of the collision strength need be approximated. The collision strength is locally fitted, within each tabulation interval, to a function that makes the integrand of equations 3.19 and 3.20 integrable analytically. The nature of the form of the collision strength

has been given significant consideration. Quadrature with  $\kappa$  and Druyvesteyn distributions is analytic, with the collision strength represented by a first or second order power series; the integrals between tabulated energy points  $\varepsilon_i$  and  $\varepsilon_{i+1}$  then take the form,

$$\int_{\varepsilon_i}^{\varepsilon_{i+1}} \Omega (1+u)^{-(\kappa+1)} du = \left[ \frac{1}{\kappa} (1+u)^{-\kappa} (w_1 u + w_0) + \frac{1}{\kappa(\kappa-1)} (1+u)^{1-\kappa} w_1 \right]_{\varepsilon_i}^{\varepsilon_{i+1}}, \quad (3.25)$$

for the  $\kappa$  distribution and,

$$\int_{\varepsilon_i}^{\varepsilon_{i+1}} \Omega \exp(-u^x) du = \left[ \frac{w_1}{x} \gamma\left(\frac{2}{x}, u^x\right) + \frac{w_0}{x} \gamma\left(\frac{1}{x}, u^x\right) \right]_{\varepsilon_i}^{\varepsilon_{i+1}}, \quad (3.26)$$

for the Druyvesteyn, where  $\gamma$  is the incomplete gamma function and the collision strength has been approximated linearly as,

$$\Omega = w_1 u + w_0. \quad (3.27)$$

Equivalent expressions for the second order power series are found similarly. Note that, as a simplification,  $u$  has been introduced, although it is not equivalent in the case of  $\kappa$  and Druyvesteyn distributions. For the  $\kappa$  distribution,

$$u = \frac{\varepsilon}{\kappa E_\kappa}, \quad (3.28)$$

and for the Druyvesteyn distribution,

$$u = \frac{\varepsilon \Gamma(3/2x)}{E_x \Gamma(5/2x)}. \quad (3.29)$$

In testing the validity of these approximations, it was found that quadratic interpolation can be unsafe for certain tabulations of the collision strength. Figure 3.6 shows  $\Upsilon$  of a Druyvesteyn distribution of  $x = 2$  for the  $1s3s\ ^1S - 1s4p\ ^1P$  transition in neutral helium, for both linear and quadratic fits to the collision strength.  $\Upsilon$  displays a smooth variation with effective temperature for the linear fit, but there is a hump in the  $\Upsilon$  from the quadratic fit that seems unphysical. Further investigation of the behaviour of  $\Upsilon$  is gleaned by examination of the collision strength itself. Figure 3.7 shows the collision strength plotted in

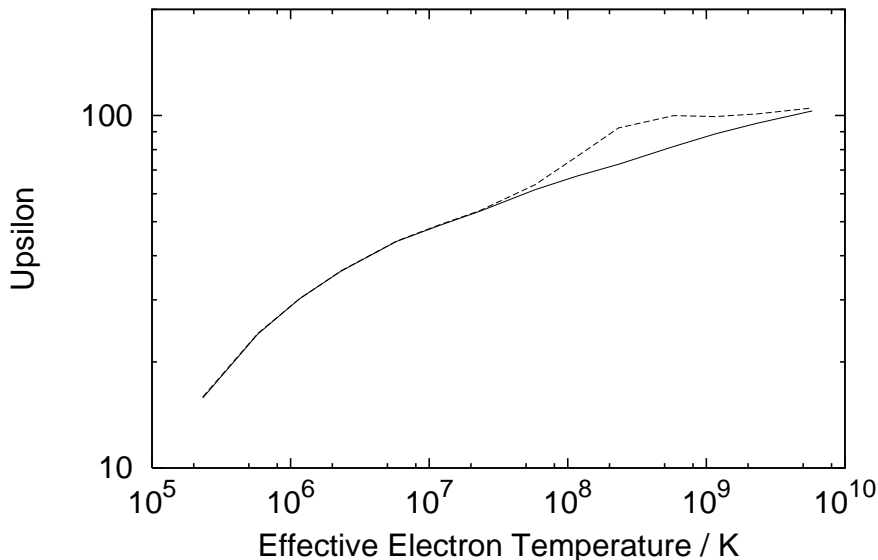


Figure 3.6: Effective collision strength for a Druyvesteyn distribution of  $x = 2$  for the  $1s3s\ ^1S - 1s4p\ ^1P$  excitation transition of neutral helium. The solid line shows the results where the collision strength has been fitted linearly between tabulated points. The dashed line shows the results where the collision strength has been fitted quadratically.

Burgess–Tully space, with  $C = 5$  to highlight the high energy behaviour. The maximum deviation between the linearly and quadratically generated effective collision strengths is in the effective temperature range  $10^8 - 10^9$  K. This corresponds to the most significant contribution from the collision strength coming from  $\sim 0.8$  on the reduced energy scale of figure 3.7. The collision strength is seen to be slowly varying in this energy range, showing no behaviour similar to the hump seen in the effective collision strength as calculated by quadratic interpolation. Thus, it is likely that the hump is an unphysical result of the numerical technique rather than any physical significance.

Figure 3.7 also indicates that, in this high-energy range, the tabulated data is close to the high-energy limiting behaviour, as is indicated by the extension of the curve to the Bethe limit point. Thus, it is useful to fit the data on a logarithmic scale for the last tabulated points, as in figure 3.8. The figure shows the final three collision strength tabulations along with fits between them. If one considers the logarithmic fit to best follow the data in this energy range, the linear fit is shown to underestimate the collision strength by 4% while the quadratic fit overestimates by 25%. It is apparent that a quadratic fit is unsound for these points, manifesting itself as the hump of figure 3.6.

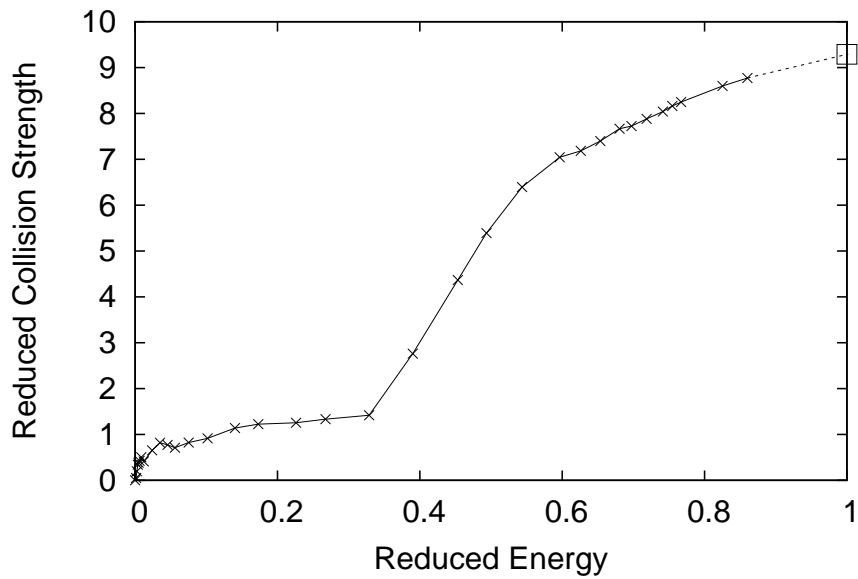


Figure 3.7: Reduced collision strength for the  $1s3s\ ^1S - 1s4p\ ^1P$  transition of neutral helium, obtained using a reduced-energy parameter of  $C = 5$  (see text for details). The solid line and crosses denote preferred ADAS data, and the dashed line links the highest energy point to the infinite-energy limit point (square box).

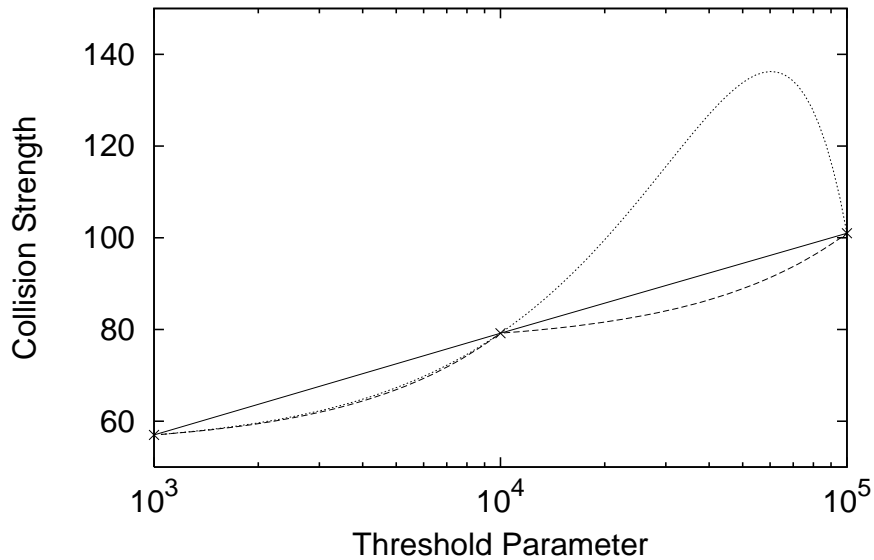


Figure 3.8: Collision strength for the  $1s3s\ ^1S - 1s4p\ ^1P$  transition of neutral helium. The solid lines denote a straight line in logarithmic threshold parameter space between tabulated points, the dashed line shows a linear fit between points, and the dotted line shows a quadratic fit between the points.

A further problem with quadratic interpolation is that there is the possibility of a negative collision strength should the tabulated data be decreasing with energy. The collision strength data used in the present work is tabulated finely enough in energy that there is no discernible advantage in using quadratic interpolation over linear. On moving to the high-energy region, the energy tabulation becomes coarser but, as shown, this does not necessarily mean that a quadratic fit will track the collision strength any more accurately than a linear fit. It is recommended that linear interpolation be used as the standard method, with quadratic interpolation available should the resultant effective collision strengths be questionable. In such cases, it is prudent to examine the behaviour of the collision strength and how the different fits match with what is expected.

Quadrature of the collision strength with a numerically tabulated distribution function requires functional fitting of both collision strength and distribution function. Again, the collision strength is fitted by a polynomial of first or second order, with first order being regarded preferential for the same reasons as highlighted above. Functional fitting of the distribution function is not as obvious as the collision strength; the exact nature of the distribution can vary dramatically from situation to situation. The methods employed here are intended for use on an arbitrary distribution, so a form that is best suited to the preponderance of distributions, whilst being portable to others, is sought. Outwith specially contrived experiments, electron distribution functions tend to be perturbations from Maxwellian in the low- or high-energy range, but maintaining the general form of the Maxwellian distribution. The tabulated distribution functions are thus fitted locally as,

$$f(\varepsilon) = a\sqrt{\varepsilon}e^{-b\varepsilon}. \quad (3.30)$$

The effective collision strength integrals then take the form,

$$\int_{\varepsilon_i}^{\varepsilon_{i+1}} \frac{1}{\sqrt{\varepsilon}} f(\varepsilon) \Omega \, d\varepsilon = \left[ \frac{a}{b} e^{-b\varepsilon} \left( w_1 \varepsilon + \frac{w_1}{b} + w_0 \right) \right]_{\varepsilon_i}^{\varepsilon_{i+1}}, \quad (3.31)$$

in the tabular interval  $[\varepsilon_i, \varepsilon_{i+1}]$  where  $\Omega$  is linear in  $\varepsilon$ .

One must also define over which energy grid the integral is to be performed. The interval averaged collision strength is expected to vary more smoothly than the distribution function, so the distribution should be tabulated more finely. The integral is then performed over the distribution function energy grid with the collision strength interpolated to these points.

The integrals of equations 3.19 and 3.20 are over the range  $[0, \infty)$  in final

electron energy and so extrapolation is certainly required to the high-energy limit and possibly to the low-energy limit, depending on the energy grid. It is common practice that the results of collision strength calculations come tabulated with the lowest value being that of the excitation threshold, so extrapolation to the low-energy limit is usually not of issue. However, for cases where the tabulation begins above threshold, extrapolation is required; two possibilities are allowed here. Excitation collision strengths are finite at threshold for electron collision with an ion and zero with a neutral atom. For extrapolation purposes, a simple straight line from 0 to the first point is used for collision with a neutral. For ions, the collision strength is assumed constant from threshold to the first point. This is safe if the tabulation does not begin too far from threshold.

Extrapolation to infinite energy is more complicated; transition type, as described in section 2.1.1, is taken into account. For type 1 transitions (see section 2.1.1) there is a logarithmic behaviour of the collision strength at high energy. This is expressed as,

$$\Omega = a \ln(X + b), \quad (3.32)$$

where  $a$  and  $b$  are determined from the last two collision strength tabulations; or by fitting a straight line in Burgess-Tully space from the last tabulated point to the infinite-energy limit value. Provided that the tabulation goes high enough in energy that the collision strength is beginning to follow the logarithmic behaviour then these approximations are similar. Examination of the collision strength may suggest that one expression fits the behaviour better than the other; it is left to the discretion of the modeller. One issue with the choice of fit is that equation 3.32 is only suitable if the collision strength is increasing with energy, while the Burgess-Tully fit is always applicable since only the last collision strength point is taken into account.

For a Maxwellian distribution, the fit of equation 3.32 makes the quadrature analytically integrable, while the integral is only analytic for the Burgess-Tully fit if the parameter  $C$  is chosen to equal  $e$ . However, neither the  $\kappa$  nor Druyvesteyn distributions can be integrated analytically with these fits. Instead, the trapezoidal rule is used from the last energy point over an energy step based on the energy difference between the last two points, continuing until the contribution to the integral meets a predefined tolerance. Since the distribution function falls off faster than the collision strength increases, convergence is met quickly.

Collision strengths of type 2 transitions follow a constant behaviour to infinite energy. Analogous to the situation with type 1 transitions, extrapolation to infinite energy is either by a straight line in Burgess-Tully space to the Born

limit, or by a functional fit of the last two tabulated values. Here, the fit used is,

$$\Omega = a + \frac{b}{X}, \quad (3.33)$$

which is only suitable should the last two values be such that  $a \geq 0$  and  $X > -b/a$ . For these fits, the Maxwellian distribution is again analytic, but now  $C$  may take any value. Also, the  $\kappa$  and Druyvesteyn distributions must be treated using the same trapezoidal approach as for type 1 transitions. It is pointed out, however, that the fit to  $\Omega$  here is a sum where contribution to the integral from the first term is indeed analytic; the integral is split, with the first part being treated analytically and the second using the trapezoidal rule. Convergence in this case is faster than that of type 1 as both terms of the integrand are decreasing with energy.

Extrapolation of type 3 transitions does not provide such a significant contribution to the effective collision strength since the collision strength falls off as  $1/X^2$ . This behaviour is fitted from the last two values according to,

$$\Omega = \frac{a}{(X + b)^2}, \quad (3.34)$$

provided the final collision strength value lies below the previous one.

Extrapolation to both low and high energy in the case of numerical distribution functions is further complicated by having to consider how the distribution function behaves in these extremes. The approach here, is to allow various analytic extrapolations of the distribution that are considered to match physical situations. Should these be unsatisfactory then there is always the possibility of extending the energy range of tabulation until the distribution becomes negligible or until one of the analytic representations is approached.

Low-energy behaviour of the distribution function can be represented by,

$$f(\varepsilon) = \varepsilon^{p_0}, \quad (3.35)$$

where  $p_0$  is a parameter chosen at the time of constructing the distribution that best fits the data. The fit is normalised to the first value of  $f(\varepsilon)$ . Alternatively, a simple cut-off below the lowest energy tabulation is allowed.

Beyond the ultimate tabulation of  $f(\varepsilon)$ , the distribution may take the follow-

ing forms:

$$f(\varepsilon) = \varepsilon^{-p_1} \quad (3.36)$$

$$f(\varepsilon) = \exp(-p_1\varepsilon) \quad (3.37)$$

$$f(\varepsilon) = \exp(-p_1\varepsilon^{p_2}), \quad (3.38)$$

where the fitting parameters  $p_1$  and  $p_2$  are chosen to best fit the high-energy form of the distribution. The fits are normalised to the last value of  $f(\varepsilon)$ . As with the low energy behaviour, a cut-off above the last energy point is also allowed. The power-law behaviour of equation 3.36 represents the high-energy form of the  $\kappa$  distribution, equation 3.37 has the exponential behaviour of the Maxwellian distribution, and equation 3.38 matches the high-energy behaviour of the Druyvesteyn distribution.

There are then a number of contributions to the effective collision strength integrals, of which each are dealt in turn. The energy points as tabulated for the collision strength are denoted  $\varepsilon_i^\Omega$ , where  $0 < i < m$ ; and for the distribution function are denoted  $\varepsilon_j^f$ , where  $0 < j < n$ .

- Contribution from threshold to first tabulated energy.

The threshold behaviour of both the distribution function and the collision strength is used, and the integral can take one of a number of forms based on these representations.

- Contribution from first point in distribution function tabulation to first point in collision strength tabulation, where  $\varepsilon_0^f < \varepsilon_0^\Omega$ .

In this region, the distribution is fitted to the form of equation 3.30 and the collision strength fitted with either constant or zero threshold behaviour depending on the charge state of the ion.

- Contribution from first point in collision strength tabulation to first point in distribution function tabulation, where  $\varepsilon_0^\Omega < \varepsilon_0^f$ .

Either a linear or quadratic fit to the collision strength is used, and the distribution function is fitted by equation 3.35. If the low-energy behaviour of the distribution is to cut off below the first tabulation then there is no contribution to the integral.

- Contribution from the greater of  $\varepsilon_0^\Omega$  and  $\varepsilon_0^f$  to the lesser of  $\varepsilon_m^\Omega$  and  $\varepsilon_n^f$ .

The collision strength is interpolated either linearly or quadratically to the distribution function energy grid and the distribution function follows the fit of equation 3.30.

- Contribution from last point in distribution function tabulation to last point in collision strength tabulation, where  $\varepsilon_n^f < \varepsilon_m^\Omega$ .

Here, the distribution function is fitted by one of equations 3.36, 3.37 or 3.38 and the collision strength is again fitted linearly or quadratically.

- Contribution from last point in collision strength tabulation to last point in distribution function tabulation, where  $\varepsilon_m^\Omega < \varepsilon_n^f$ .

The distribution function follows equation 3.30 and the collision strength is extrapolated to the distribution function energy grid using the transition type definitions of section 2.1.1.

- Contribution from last tabulated point to infinity.

Both the distribution function and the collision strength are extrapolated to the high-energy region. The collision strength behaviour is determined by the transition type and the distribution function is then fitted by equation 3.36, 3.37 or 3.38.

Results for  $\Upsilon$  and  $\mathcal{J}$  are illustrated for various transitions of neutral helium. Figure 3.10(a) shows  $\Upsilon$  for the  $1s^2\ ^1S - 1s2s\ ^3S$  transition, with figure 3.10(b) showing the equivalent  $\mathcal{J}$ . This example has been chosen in illustration of the effect the exponential factor of equation 3.19 can have on  $\Upsilon$ . This particular transition has a high transition energy,  $\Delta E_{ij} = 19.8$  eV. It is seen that, even for large values of  $\kappa$ , if one goes to low temperatures the exponential dominates and  $\Upsilon$  is several orders of magnitude larger than it would be if convoluted with a Maxwellian distribution. There is no such factor for the  $\mathcal{J}$  expression, and hence figure 3.10(b) shows no such behaviour at low effective temperature.

Figures 3.12(a) to 3.16(b) show the main features of  $\Upsilon$  and  $\mathcal{J}$  when the exponential factor is not dominant. Figures 3.12(a) and 3.12(b) show the dipole allowed, or type 1, transition  $1s2s\ ^3S - 1s2p\ ^3P$ , again from neutral helium, for different  $\kappa$  and Druyvesteyn distributions and the Maxwellian distribution. Figures 3.14(a) and 3.14(b) show the type 2 transition  $1s2s\ ^3S - 1s3s\ ^3S$ , and figures 3.16(a) and 3.16(b) show the type 3 transition  $1s2s\ ^3S - 1s2s\ ^1S$ . For each of these transitions, the collision strength used to calculate the effective collision strengths is also shown as Burgess–Tully plots with the ionisation threshold placed at 0.5 in reduced energy space (figures 3.2.1, 3.2.1, 3.2.1 and 3.2.1). It should be

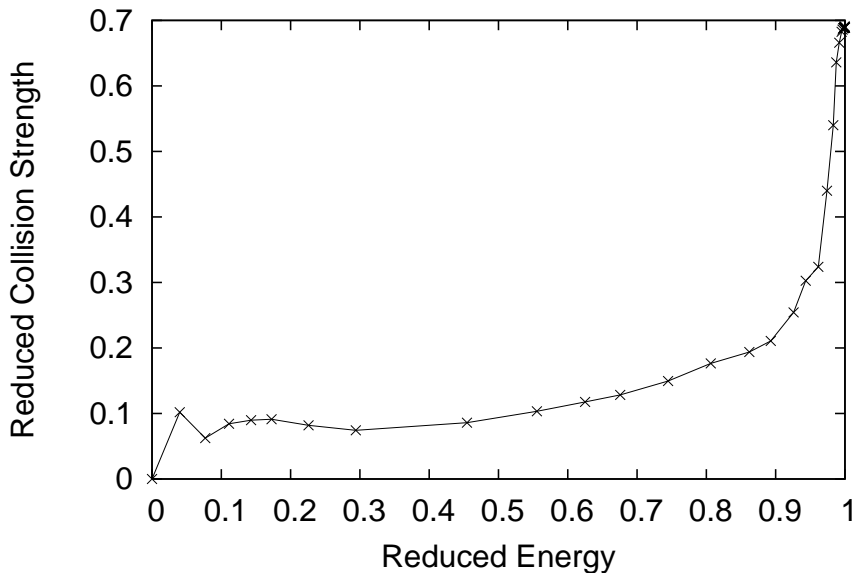


Figure 3.9: Reduced collision strength for the  $1s^2\ ^1S - 1s2s\ ^3S$  transition of  $\text{He}^0$  plotted in Burgess–Tully space with a reduced energy parameter of  $C = 0.24$  to place the ionisation threshold at 0.5 on the reduced energy scale.

noted that these are in fact averaged collision strengths so do not contain the full resonance structure of the original data (see section 2.1.1).

The deviation from Maxwellian is as expected. The  $\kappa$  distribution is characterised by an increased population of both low- and high-energy electrons over an equivalent Maxwellian distribution. This deviation is seen to be carried through to the effective collision strengths. The contrasting behaviour of the Druyvesteyn distribution is also observable in the effective collision strengths.

### 3.2.2 Radiative Recombination

Returning to the radiative recombination, photoionisation and stimulated recombination reactions of section 2.1.3 (equations 2.27, 2.28 and 2.29), one determines the corresponding non-Maxwellian rate coefficients by considering the Milne relations of equations 2.30 and 2.31 as in the Maxwellian argument. The recombination coefficient is then obtained as,

$$\alpha_i^{(r)}(T_{\text{eff}}) = \frac{32\alpha^4 c \pi a_0^2 z_1^4}{3\sqrt{3} \nu^3} \int_0^\infty \sqrt{\frac{I_{\text{H}}}{\varepsilon}} \frac{g^{\text{II}}}{\varepsilon/I_{\text{H}} + I_i/I_{\text{H}}} f(\varepsilon) d\varepsilon. \quad (3.39)$$

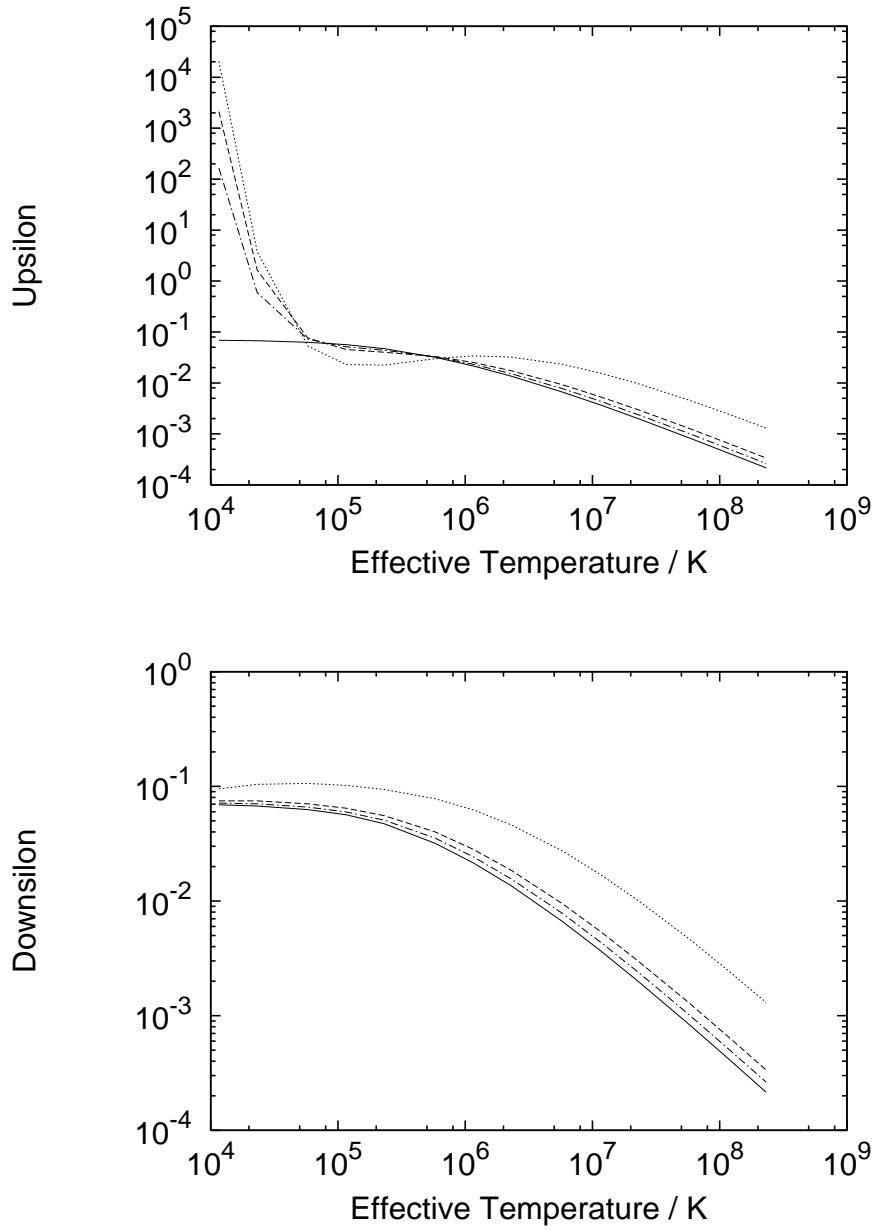


Figure 3.10: Effective collision strengths for the  $1s^2 \ ^1S - 1s2s \ ^3S$  transition of neutral helium. The upper figure shows excitation and the lower de-excitation. The solid curve shows the result of quadrature with a Maxwellian distribution; the dotted curve, a  $\kappa$  distribution with  $\kappa = 2$ ; the dashed curve,  $\kappa = 5$ ; and the dot-dashed curve,  $\kappa = 10$ .

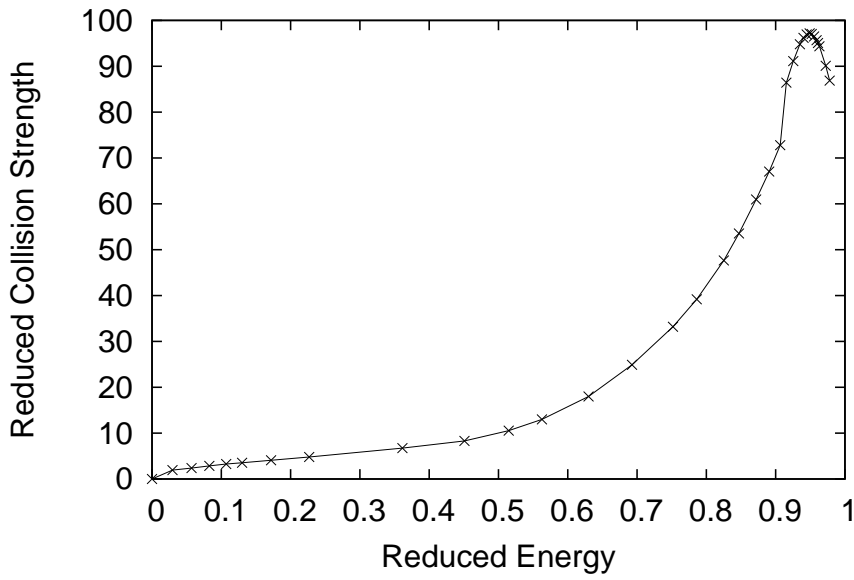


Figure 3.11: Reduced collision strength for the  $1s2s^3S - 1s2p^3P$  transition of  $\text{He}^0$  plotted in Burgess–Tully space with a reduced energy parameter of  $C = 1.29$  to place the ionisation threshold at 0.5 on the reduced energy scale.

For the  $\kappa$  distribution, equation 3.39 becomes,

$$\alpha_i^{(r),\kappa}(T_{\text{eff}}) = \frac{32\alpha^4 c\pi a_0^2 z_1^4}{3\sqrt{3}} \frac{1}{\nu^3} \left( \frac{I_{\text{H}}}{\kappa E_{\kappa}} \right)^{3/2} \frac{2}{\sqrt{\pi}} \frac{\Gamma(\kappa + 1)}{\Gamma(\kappa - 1/2)} \int_0^{\infty} \frac{g^{\text{II}}}{\varepsilon + I_i} \left( 1 + \frac{\varepsilon}{\kappa E_{\kappa}} \right)^{-(\kappa+1)} d\varepsilon, \quad (3.40)$$

and for the Druyvesteyn distribution,

$$\alpha_i^{(r),D}(T_{\text{eff}}) = \frac{32\alpha^4 c\pi a_0^2 z_1^4}{3\sqrt{3}} \frac{1}{\nu^3} \left( \frac{I_{\text{H}}}{\kappa E_{\kappa}} \right)^{3/2} x \frac{\Gamma(5/2x)^{3/2}}{\Gamma(3/2x)^{5/2}} \int_0^{\infty} \frac{g^{\text{II}}}{\varepsilon + I_i} \exp \left( - \left[ \frac{\varepsilon \Gamma(5/2x)}{E_x \Gamma(3/2x)} \right]^x \right) d\varepsilon. \quad (3.41)$$

Evaluation of these integrals requires evaluation of the free-bound Gaunt factor,  $g^{\text{II}}$ . A brief overview of  $g^{\text{II}}$  is given and we discuss the method implemented here in its calculation. There are, in fact, three Gaunt factors if one uses the notation of Menzel and Pekeris (1935): the bound-bound Gaunt factor,  $g^{\text{I}}$ ; the bound-free Gaunt factor,  $g^{\text{II}}$ , which is of interest here; and the free-free Gaunt factor,  $g^{\text{III}}$ . Of relevance here, is the work of Burgess and Summers (1976, 1987).

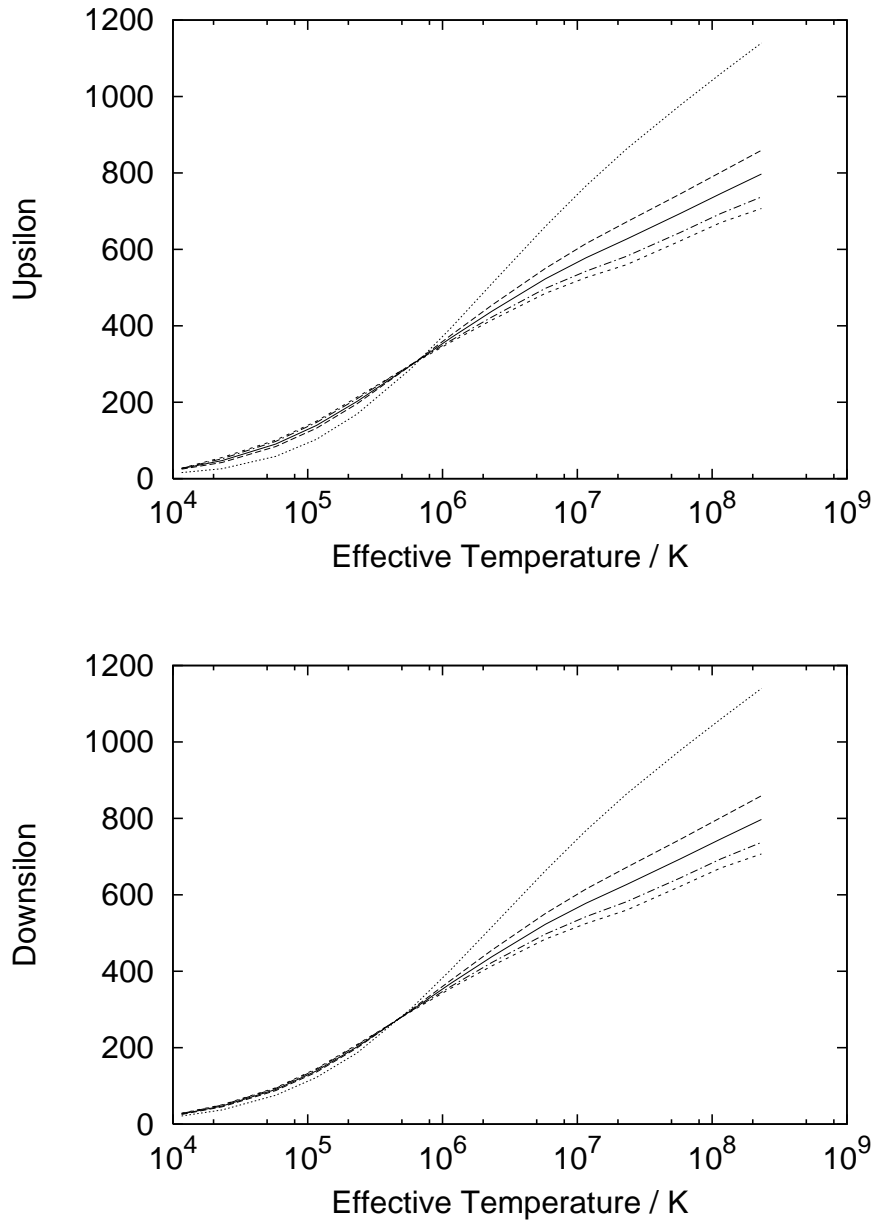


Figure 3.12: Effective collision strengths for the dipole allowed  $1s2s\ ^3S - 1s2p\ ^3P$  transition of neutral helium. The upper figure shows excitation and the lower de-excitation. The solid curve shows the result of quadrature with a Maxwellian distribution; the dotted curve, a  $\kappa$  distribution with  $\kappa = 2$ ; the long dashed curve,  $\kappa = 5$ ; the dot-dashed curve, a Druyvesteyn distribution with  $x = 2$ ; and the short dashed curve,  $x = 5$ .

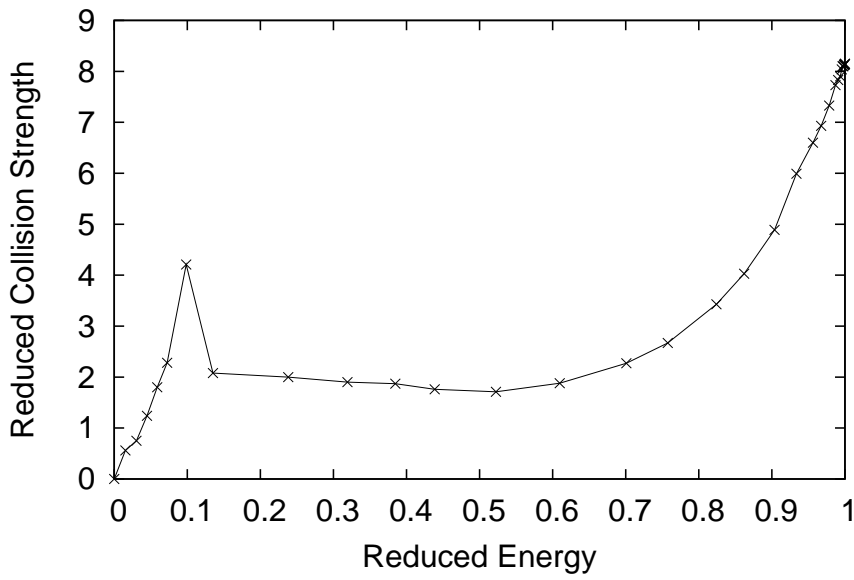


Figure 3.13: Reduced collision strength for the  $1s2s\ ^3S - 1s3s\ ^3S$  transition of  $\text{He}^0$  plotted in Burgess–Tully space with a reduced energy parameter of  $C = 0.64$  to place the ionisation threshold at 0.5 on the reduced energy scale.

It is convenient to introduce some notation before discussing the methods used to calculate the Gaunt factor. For an ion  $\mathcal{A}^{z+}$  with nuclear charge  $z_0$ , let  $z_1 = z + 1$ , and introduce  $\epsilon$ ,  $\epsilon'$ ,  $\kappa$  and  $\nu'$  defined as,

$$\epsilon = \kappa^2 = \frac{\epsilon}{z_1^2 I_{\text{H}}}, \quad (3.42)$$

and

$$\epsilon' = -\frac{1}{\nu'^2} = \frac{\epsilon'}{z_1^2 I_{\text{H}}}. \quad (3.43)$$

Then, in terms of the full level resolution, the free-bound Gaunt factor can be expressed in terms of quantum numbers  $S$ ,  $L$  and  $J$  as,

$$g_{ii'}^{\text{II}} = \frac{\sqrt{3}}{\pi 2^4} \left( \frac{\epsilon - \epsilon'}{z_1^2 I_{\text{H}}} \right)^4 \frac{1}{\omega_i} Q_{ii'} R_{ii'}^{\text{II}}(\kappa, \nu'). \quad (3.44)$$

The initial state,  $\gamma n l S L J$ , is denoted  $i$  and the final state,  $\gamma n' l' S L' J'$ , by  $i'$ . The angular factor,  $Q_{ii'}$ , is given by,

$$Q_{ii'} = (2J + 1)(2L + 1)(2J' + 1)(2L' + 1) \times \left\{ \begin{matrix} L' & 1 & L \\ J & S & J' \end{matrix} \right\}^2 \left\{ \begin{matrix} L' & 1 & L \\ l & L_p & l' \end{matrix} \right\}^2, \quad (3.45)$$

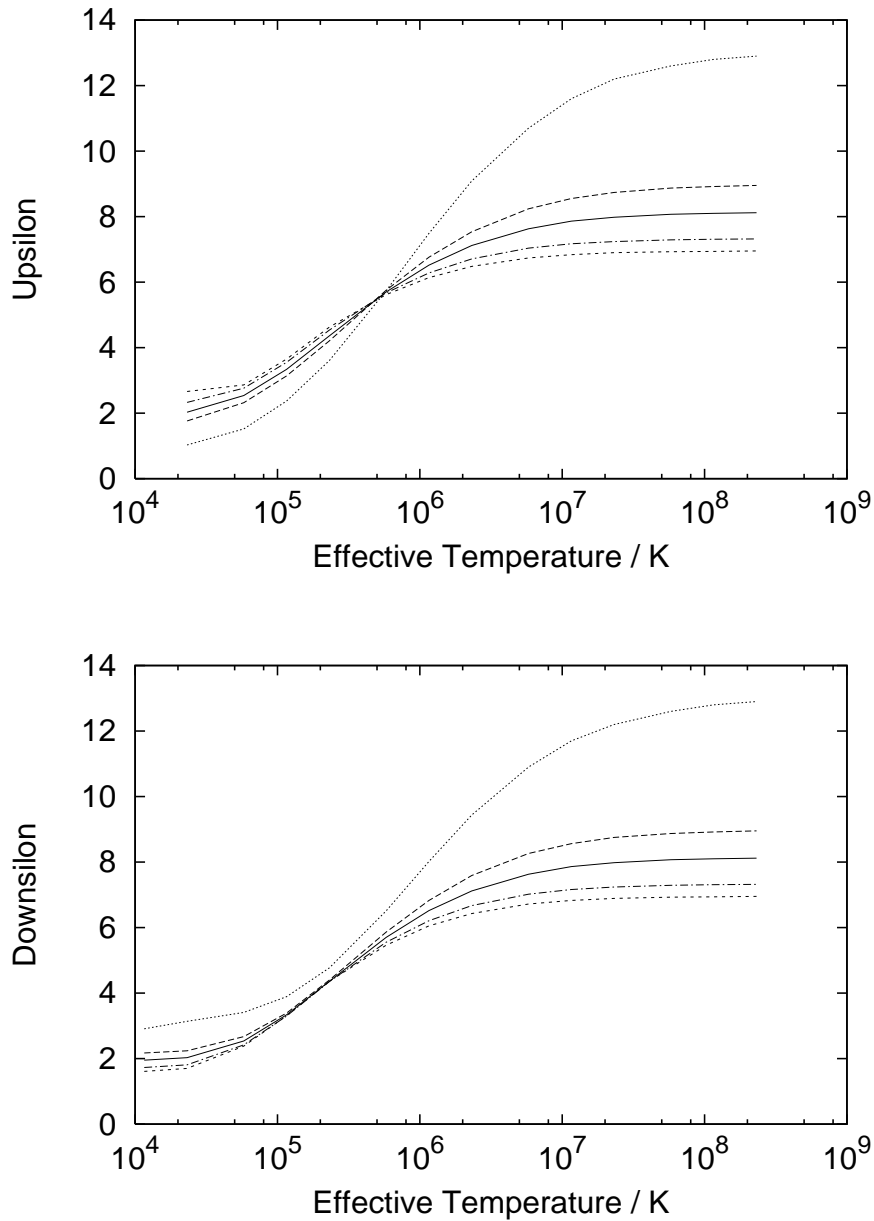


Figure 3.14: Effective collision strengths for the dipole forbidden  $1s2s^3S - 1s3s^3S$  transition of neutral helium. The upper figure shows excitation and the lower de-excitation. The solid curve shows the result of quadrature with a Maxwellian distribution; the dotted curve, a  $\kappa$  distribution with  $\kappa = 2$ ; the long dashed curve,  $\kappa = 5$ ; the dot-dashed curve, a Druyvesteyn distribution with  $x = 2$ ; and the short dashed curve,  $x = 5$ .

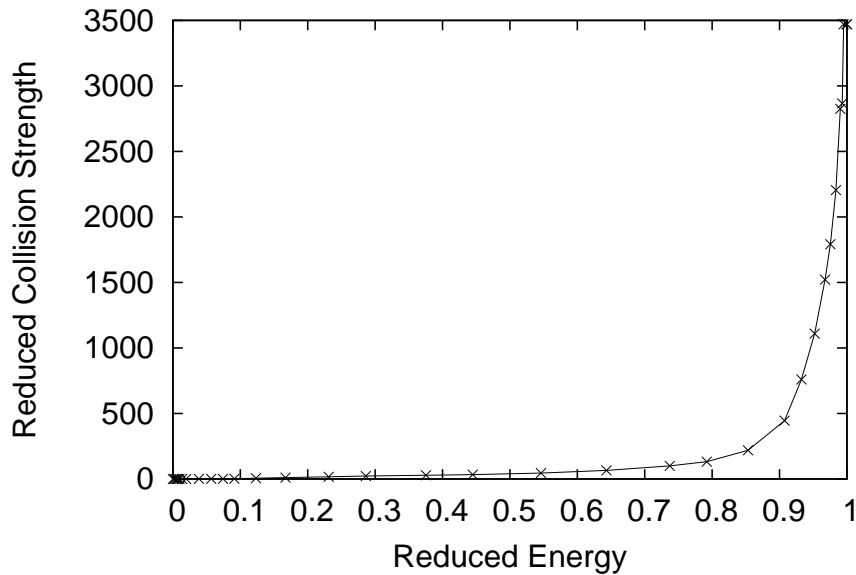


Figure 3.15: Reduced collision strength for the  $1s2s\ ^3S - 1s2s\ ^1S$  transition of  $\text{He}^0$  plotted in Burgess–Tully space with a reduced energy parameter of  $C = 5$  to place the ionisation threshold at 0.5 on the reduced energy scale. It should be noted that the asymptotic behaviour is not evident until higher values of  $X$  than shown here.

and the radial integral is,

$$R_{ii'}^{\text{H}}(\kappa, \nu') = \frac{\pi\nu'^3}{2} |\langle \kappa l | \rho | \nu' l' \rangle|^2. \quad (3.46)$$

The present treatment of the free-bound Gaunt factor is based on separating contributions coming from large and small  $l$  values and then summing. It is noted that for large  $l$ , the radial integrals are effectively hydrogenic, but at small  $l$ , quantum defects necessitate non-hydrogenic approximations. Calculation of hydrogenic radial integrals are rapid compared to non-hydrogenic integrals; it is desirable to perform elaborate non-hydrogenic calculations up to some value of  $l$  and revert to the hydrogenic approximation at higher  $l$ . The choice of the level of sophistication of the non-hydrogenic approximations will depend on the calculation time available, the level of data and a consideration of the application of the results.

A fit of the hydrogenic Gaunt factor (note H subscript) was given by Burgess

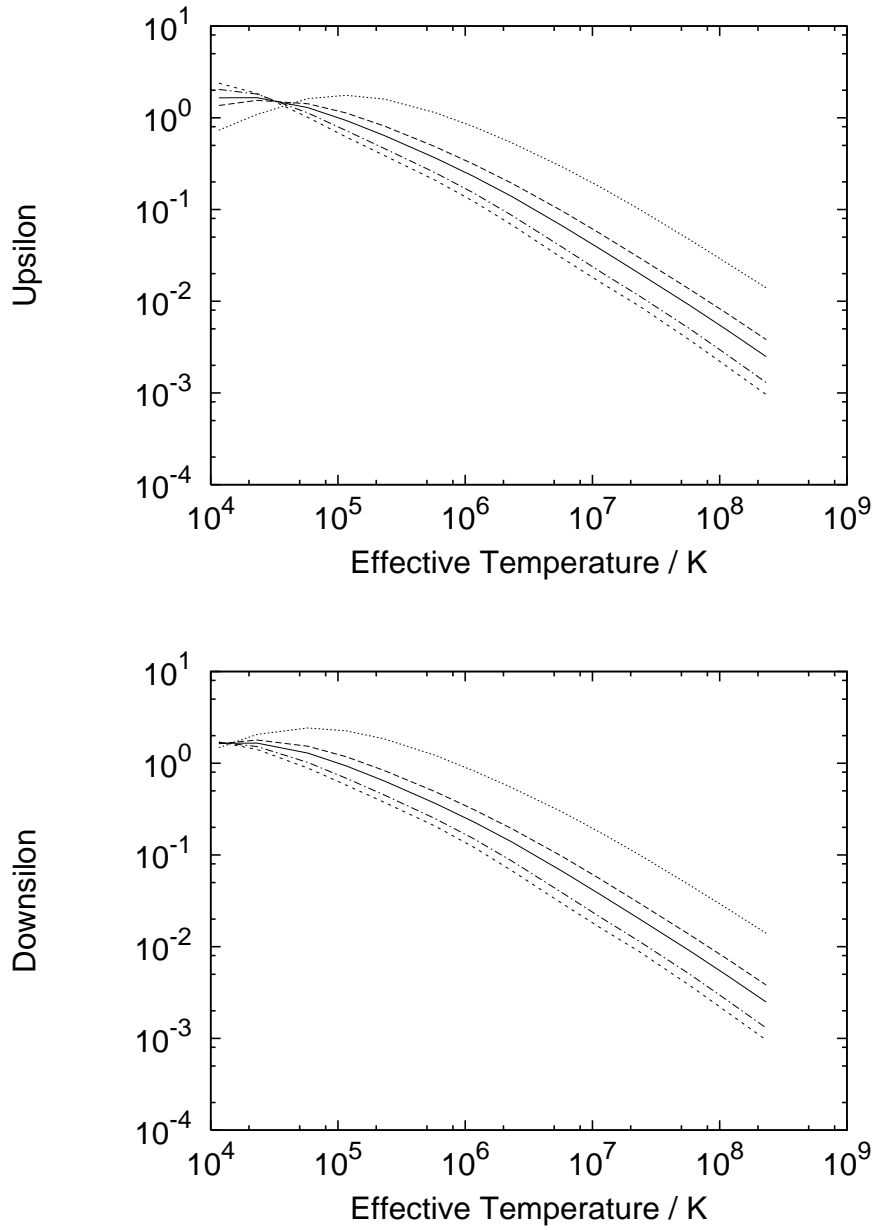


Figure 3.16: Effective collision strengths for the spin-changing  $1s2s\ ^3S - 1s2s\ ^1S$  transition of neutral helium. The upper figure shows excitation and the lower de-excitation. The solid curve shows the result of quadrature with a Maxwellian distribution; the dotted curve, a  $\kappa$  distribution with  $\kappa = 2$ ; the long dashed curve,  $\kappa = 5$ ; the dot-dashed curve, a Druyvesteyn distribution with  $x = 2$ ; and the short dashed curve,  $x = 5$ .

and Summers (1976) as,

$$g_{\text{H}}^{\text{II}}(\kappa, n') = \left\{ 1 - \frac{4 \cdot 0.1728(u-1)}{3 n'^{2/3}(u+1)^{2/3}} + \left[ \frac{28}{18} \left( \frac{0.1728(u-1)}{n'^{2/3}(u+1)^{2/3}} \right)^2 + \frac{4}{3} \left( \frac{0.0496(u^2 + 4u/3 + 1)}{n'^{4/3}(u+1)^{4/3}} \right) \right] \right\}^{-3/4}, \quad (3.47)$$

where  $u = n'^2 \kappa^2$ . It is accurate to  $\sim 0.5\%$  to the peak of  $g^{\text{II}}$  and is approximately correct for the asymptotic behaviour beyond this. The non-hydrogenic Gaunt factor is then approximated as,

$$g^{\text{II}}(\kappa, \nu') = \sum_{l, l' < l_0} g^{\text{II}}(\kappa l, \nu' l') + \sum_{l, l' \geq l_0} g_{\text{H}}^{\text{II}}(\kappa l, n' l'), \quad (3.48)$$

where the hydrogenic Gaunt factor is used at angular momentum values above  $l_0$ .

For a Maxwellian distribution, solution of the radiative recombination coefficient comes down to the integral of equation 2.32,

$$\int_{I_i/kT_e}^{\infty} \frac{g^{\text{II}} e^{-x}}{x} dx. \quad (3.49)$$

This integral is evaluated numerically by 8-point Gaussian quadrature. The exponential functional form of the integrals is lost when quadrature is with the  $\kappa$  or Druyvesteyn distributions; the integrals of equations 3.40 and 3.41 are evaluated using the trapezoidal method over a suitable number of points. Figure 3.17 shows how the radiative recombination coefficient is affected by differing degrees of deviation from Maxwellian form. For this example, recombination to the ground state of neutral helium, there is an increase in the coefficient for  $\kappa$  distributions and a decrease for Druyvesteyn distributions.

### 3.2.3 Dielectronic Recombination

Following from section 2.1.3, the dielectronic recombination process is generalised to a distribution function,  $f$ ,

$$\alpha_{\gamma \rightarrow i}^{(d)}(T_{\text{eff}}) = 2I_{\text{H}} \pi^2 a_0^3 \sum_k \frac{\omega_k}{\omega_{\gamma}} \frac{I_{\text{H}}}{E_c} f(E_c) \times \frac{\sum_l A_{k \rightarrow \gamma, E_c l}^a A_{k \rightarrow i}^r}{\sum_h A_{k \rightarrow h}^r + \sum_{m, l} A_{k \rightarrow m, E_c l}^a}. \quad (3.50)$$

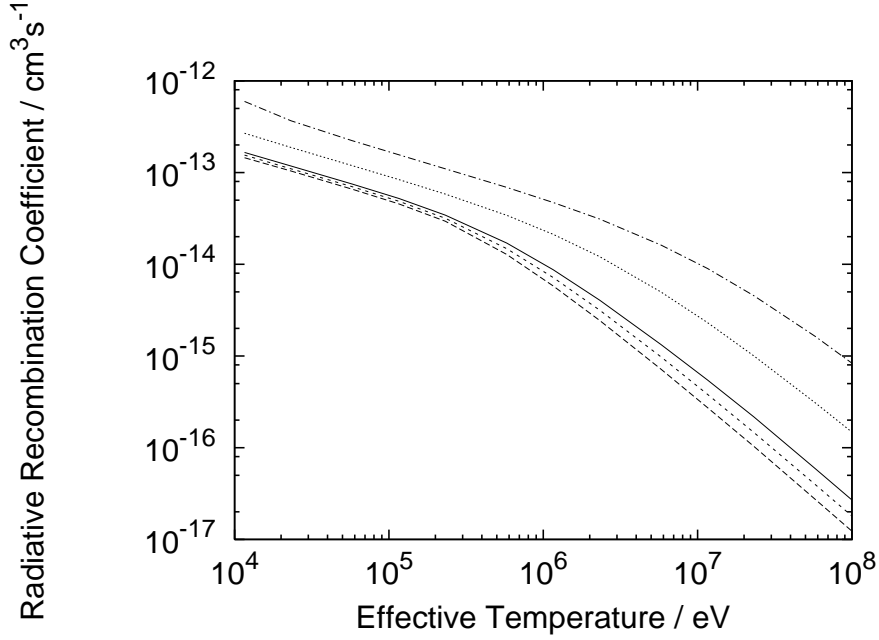


Figure 3.17: The radiative recombination coefficient for  $\kappa$ , Druyvesteyn and Maxwellian distributions for capture to the ground state of neutral helium. The curves are generated by numerical quadrature over the free-bound Gaunt factor and the distribution function. The solid curve denotes the Maxwellian distribution; the dot-dashed curve, a  $\kappa$  distribution with  $\kappa = 1.6$ ; the dotted curve, a  $\kappa$  distribution with  $\kappa = 2$ ; the short dashed curve, a Druyvesteyn distribution with  $x = 1.5$ ; and the long dashed curve, a Druyvesteyn distribution with  $x = 3$ .

In general, a summation over a manifold of nearly degenerate states belonging to a level, term or shell is required, with  $E_c$  representing the mean energy for the resonance manifold.

Since dielectronic recombination is a resonant process, one may use dielectronic recombination coefficient tabulations for Maxwellians as a function of temperature for the non-Maxwellian case by a simple conversion factor at the resonance energy. Thus the data following from the work of Badnell *et al.* (2003) remain applicable (see section 2.1.3). One first determines the resonance energy,  $E_c$ , from,

$$\alpha_{\gamma \rightarrow i}^{(d)}(T_e) = 4\pi^{3/2} a_0^3 \left( \frac{I_H}{kT_e} \right)^{3/2} \sum_k \frac{\omega_k}{2\omega_\gamma} e^{-E_c/kT_e} \times \frac{\sum_l A_{k \rightarrow \gamma, E_{cl}}^a A_{k \rightarrow i}^r}{\sum_h A_{k \rightarrow h}^r + \sum_{m,l} A_{k \rightarrow m, E_{cl}}^a}, \quad (3.51)$$

where  $\alpha_{\gamma \rightarrow i}^{(d)}(T_e)$  is the tabulated Maxwellian coefficient, and then converts to the non-Maxwellian coefficient using the ratio of the non-Maxwellian distribution at this energy to the Maxwellian distribution at the same effective temperature. The conversion factor is thus,

$$\frac{\sqrt{\pi} I_H}{2} \left( \frac{kT_e}{I_H} \right)^{3/2} \sqrt{\frac{I_H}{E_c}} e^{E_c/kT_e} f(E_c). \quad (3.52)$$

The above method assumes the Maxwellian dielectronic recombination data to have a single resonance corresponding to each  $n$ -shell and hence a precise energy of formation. This can be an oversimplification, however, as essentially, the dielectronic recombination coefficient can often display a second with the same outer-electron  $n$ -shell (for example, with both  $\Delta n = 0$  and  $\Delta n = 1$  parent transitions). Some account is taken of this by using

$$\alpha_{\gamma \rightarrow i}^{(d)}(T_e) \approx (kT_e)^{-3/2} e^{-E_c/kT_e} \quad (3.53)$$

to deduce the *local* mean resonance energy in every tabular interval. There remains a problem when the effective temperature being considered lies in between two resonances where the functional form of equation 3.53 does not fit either of the resonances. In practice, this fit will return a resonant energy somewhere between the two actual resonances, which is desirable, although a proper treatment would consider the contributions from each resonance individually.

Further error is introduced by this procedure due to outer electron stabilisa-

tion. There are some points to be noted. The large scale production of Maxwell averaged rate coefficients in the DR Project (Badnell *et al.* 2003) delivers data, according to a format (*adf09*) specified in the ADAS Project (Summers, 1993, 2004), separated according to different  $n$ - $n'$  sets of parent transition arrays. Thus, conversion to non-Maxwellian of such tabulations limits resonance energy uncertainty to within an  $n$ - $n'$  parent transition array. Parent  $\Delta n > 0$  transition arrays give dielectronic population of lower levels, but in this case the resonant energy uncertainty is low. Parent  $\Delta n = 0$  transition arrays populate high  $n$ -shells via dielectronic recombination with dipole dominance and predominantly outer-electron stabilisation. So again the error of non-Maxwellian conversion is limited.

For the present work, therefore, two strategies are adopted. The simple conversion (of each parent  $n$ - $n'$  set) is done for light element ions, for which  $n$ -shell separations are, in general, large, following equation 3.52. This is the case for the helium illustrations which follow. For ions of heavier elements, which can have parent ground states with  $n > 2$  configurations, the use of a support function, as introduced in section 2.1, is preferred. The Burgess–Bethe support function (BBGP), detailed in Badnell *et al.* (2003), is used. Studies indicate that this support function can represent  $nl$ -shell resolved,  $n$ -shell total and total zero-density dielectronic recombination coefficients to very high precision, depending on the completeness of the Bethe correction factors and the inclusion of non-dipole threshold collision strengths. BBGP handles alternative Auger channels correctly. A machinery has been established (Badnell *et al.* 2003) for the systematic preparation of the simple driver data for the BBGP support function in the general case. Since BBGP supplies the components of equation 3.51 (summed over outer quantum numbers within an  $nl$ -shell of the captured electron), it converts to non-Maxwellian directly. It is the preferred policy to form a ratio of the summed BBGP approximations over all levels at the effective temperature in Maxwellian approximation to that of the total zero-density value from the DR Project. This factor is then a multiplier on the level resolved BBGP non-Maxwellian coefficients. The BBGP support function has been used to extend GCR modelling to very high density by allowing inclusion of doubly-excited population redistribution (see also Summers *et al.* 2005). It can be used similarly in the non-Maxwellian case, although it is noted that an ion impact is the primary collisional redistribution mechanism within an  $n$ -shell of the doubly-excited system. Non-Maxwellian ion distributions are outside the scope of this thesis.

Figure 3.18 shows the dielectronic recombination coefficient for capture to the final  $1s2s\ ^1S$  state of neutral helium. For a given resonance, at low and high tem-

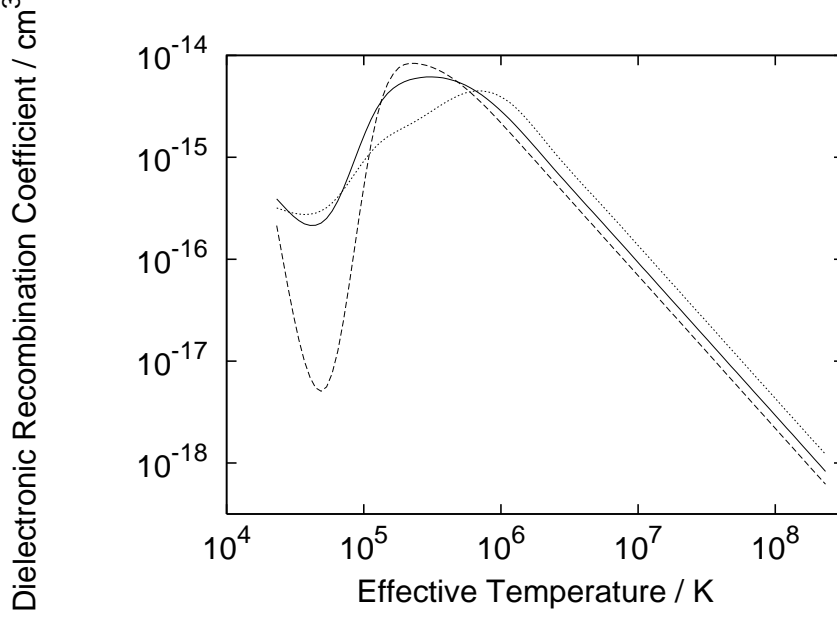


Figure 3.18: The dielectronic recombination coefficient for  $\kappa$ , Druyvesteyn and Maxwellian distributions for capture to the  $1s2s\ ^1S$  state of neutral helium. The solid curve denotes the Maxwellian distribution; the dotted curve, a  $\kappa$  distribution with  $\kappa = 2$ ; and the dashed curve, a Druyvesteyn distribution with  $x = 2$ .

peratures, the effect of dielectronic recombination is reduced for a Druyvesteyn distribution in comparison to a Maxwellian, and increased for a  $\kappa$  distribution. At intermediate temperatures, the opposite result is found. This is as expected from the form of the distribution functions. It is interesting to note that, for the example of figure 3.18, this intermediate region falls at the peak contribution of dielectronic recombination, so the primary effect of a non-Maxwellian distribution on dielectronic recombination may not be intuitive from the type of distribution. A further point of note, is that at low temperatures, it is the high-energy tail of the distribution function which contributes to the dielectronic rate coefficient, while at high temperatures, the low-energy region of the distribution contributes.

### 3.2.4 Collisional Ionisation and Three-Body Recombination

As discussed in section 2.1.3, three-body recombination is the inverse process of collisional ionisation, it is therefore advantageous to discuss them together. For a Maxwellian plasma, the three-body recombination rate is determined from the collisional ionisation rate, via equation 2.26, so no explicit formulation of the three-body recombination coefficient is necessary. The relation of equation 2.26

is not valid for a non-Maxwellian plasma so coefficients describing each reaction separately are required.

Some terminology must first be introduced in reference to reactions 2.18 and 2.25. The double differential cross-sections (in energy) are denoted by  $Q_{i \rightarrow \gamma^+}(\varepsilon; \varepsilon', \varepsilon'')$ , for ionisation, and  $Q_{\gamma^+ \rightarrow i}(\varepsilon', \varepsilon''; \varepsilon)$ , for recombination, with  $\varepsilon$  the incident electron energy,  $\varepsilon'$  the scattered incident electron energy, and  $\varepsilon''$  the ejected electron energy. Conservation of energy,

$$\varepsilon = \varepsilon' + \varepsilon'' + I_i, \quad (3.54)$$

dictates that both  $Q_{i \rightarrow \gamma^+}(\varepsilon; \varepsilon', \varepsilon'')$  and  $Q_{\gamma^+ \rightarrow i}(\varepsilon', \varepsilon''; \varepsilon)$  contain the delta function,

$$\delta(\varepsilon - \varepsilon' - \varepsilon'' - I_i), \quad (3.55)$$

as a factor. The Fowler relation for these cross-sections in terms of the statistical weights of the initial and final states of the ion is,

$$\omega_i \varepsilon Q_{i \rightarrow \gamma^+}(\varepsilon; \varepsilon', \varepsilon'') = \frac{16\pi m}{h^3} \omega_\gamma \varepsilon' \varepsilon'' Q_{\gamma^+ \rightarrow i}(\varepsilon', \varepsilon''; \varepsilon). \quad (3.56)$$

The rate coefficients are then given by integrating the corresponding cross-sections with the electron distribution functions. The ionisation rate coefficient is,

$$q_{i \rightarrow \gamma^+} = \int_{I_i}^{\infty} \int_0^{\varepsilon - I_i} \int_0^{\varepsilon - \varepsilon' - I_i} \sqrt{\frac{2\varepsilon}{m}} Q_{i \rightarrow \gamma^+}(\varepsilon; \varepsilon', \varepsilon'') f(\varepsilon) d\varepsilon'' d\varepsilon' d\varepsilon, \quad (3.57)$$

and the three-body recombination coefficient,

$$\begin{aligned} \alpha_{\gamma^+ \rightarrow i}^{(3)} = & \int_{I_i}^{\infty} \int_0^{\varepsilon - I_i} \int_0^{\varepsilon - \varepsilon' - I_i} Q_{\gamma^+ \rightarrow i}(\varepsilon', \varepsilon''; \varepsilon) \sqrt{\frac{2\varepsilon'}{m}} f(\varepsilon') \\ & \times \sqrt{\frac{2\varepsilon''}{m}} f(\varepsilon'') d\varepsilon'' d\varepsilon' d\varepsilon. \end{aligned} \quad (3.58)$$

It is convenient to write the latter in terms of the ionisation cross-section. Using the Fowler relation (equation 3.56), and introducing the effective temperature,

the three-body recombination coefficient can be expressed as,

$$\begin{aligned} \alpha_{\gamma^+ \rightarrow i}^{(3)}(T_{\text{eff}}) &= 8 \left( \frac{\pi a_0^2 I_H}{k T_{\text{eff}}} \right)^{3/2} \frac{\omega_i}{2\omega_\gamma} e^{I_i/kT_{\text{eff}}} \\ &\times \int_{I_i}^{\infty} \int_0^{\varepsilon - I_i} \int_0^{\varepsilon - \varepsilon' - I_i} \sqrt{\frac{2\varepsilon}{m}} Q_{i \rightarrow \gamma^+}(\varepsilon; \varepsilon', \varepsilon'') f(\varepsilon) \\ &\times \left[ \frac{\sqrt{\pi}}{2} (k T_{\text{eff}})^{3/2} e^{-I_i/kT_{\text{eff}}} \sqrt{\frac{\varepsilon}{\varepsilon' \varepsilon''}} \frac{f(\varepsilon') f(\varepsilon'')}{f(\varepsilon)} \right] d\varepsilon'' d\varepsilon' d\varepsilon. \end{aligned} \quad (3.59)$$

As the distribution tends to a Maxwellian,  $T_{\text{eff}} \rightarrow T_e$ , the term in square brackets tends to unity.

Using an analytic form of the differential cross-section, such as that due to Thomson (1912), can give simplified approximate results for the Maxwellian rate coefficients. The differential form of the Thomson cross-section (c.f. equation 2.21) is,

$$Q_{i \rightarrow \gamma^+}(\varepsilon; \varepsilon', \varepsilon'') = 4\pi a_0^2 \zeta I_H^2 \frac{1}{\varepsilon \varepsilon'^2} \delta(\varepsilon - \varepsilon' - \varepsilon'' - I_i). \quad (3.60)$$

In the Maxwellian case,

$$q_{i \rightarrow \gamma^+}(T_e) = 8\sqrt{\pi} \alpha c a_0^2 \zeta \frac{I_H}{I_i} \frac{I_H}{k T_e} e^{-I_i/kT_e} \left[ 1 - \frac{I_i}{k T_e} e^{I_i/kT_e} E_1(I_i/kT_e) \right], \quad (3.61)$$

and

$$\alpha_{\gamma^+ \rightarrow i}^{(3)}(T_e) = 8 \left( \frac{\pi a_0^2 I_H}{k T_e} \right)^{3/2} \frac{\omega_i}{2\omega_\gamma} e^{I_i/kT_e} q_{i \rightarrow \gamma^+}(T_e), \quad (3.62)$$

where  $E_1$  is the first exponential integral.

Even for the relatively simple Thomson representation of the cross-section, analytic solutions to equations 3.57 and 3.59 do not exist for  $\kappa$  and Druyvesteyn distributions. In any case, one would generally like to implement more accurate approximations for the cross-section, so numerical quadrature is necessary even in the case of Maxwellian distributions. It is generally the case that double differential cross-sections are not available, the total cross-section being the quantity usually measured or calculated. The total cross-section for collisional ionisation,  $\sigma_{i \rightarrow \gamma^+}(\varepsilon)$ , is related to the double differential cross-section by,

$$\sigma_{i \rightarrow \gamma^+}(\varepsilon) = \iint Q_{i \rightarrow \gamma^+}(\varepsilon; \varepsilon', \varepsilon'') d\varepsilon' d\varepsilon''. \quad (3.63)$$

However, the triple integral of equation 3.59 has a dependency on  $\varepsilon'$  and  $\varepsilon''$  outwith  $Q_{i \rightarrow \gamma^+}(\varepsilon; \varepsilon', \varepsilon'')$ , unlike equation 3.57, so equation 3.63 cannot be applied.

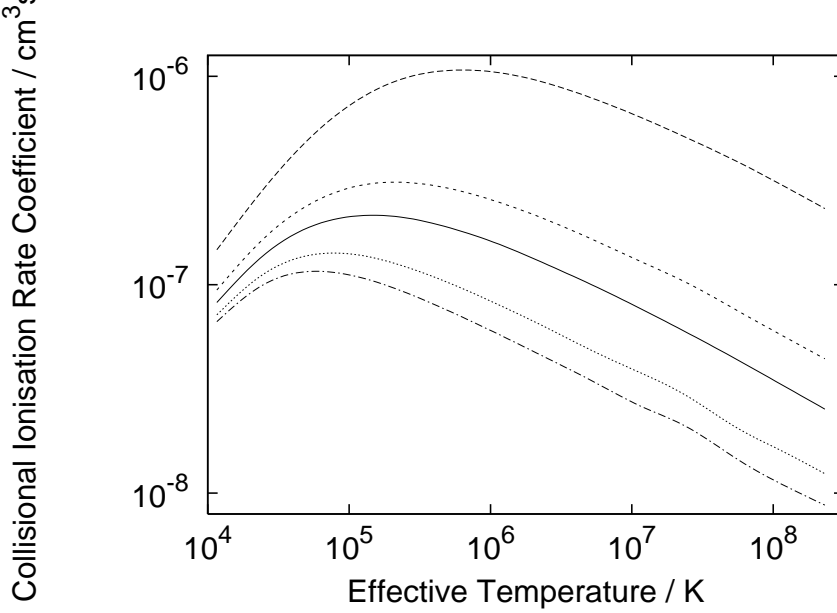


Figure 3.19: Collisional ionisation rate coefficient from  $1s2p^3P$  of neutral helium for various electron distribution functions. The solid curve shows a Maxwellian distribution; the long dashed curve, a  $\kappa$  distribution with  $\kappa = 2$ ; the short dashed curve, a  $\kappa$  distribution with  $\kappa = 5$ ; the dotted curve, a Druyvesteyn distribution with  $x = 2$ ; and the dash-dotted curve, a Druyvesteyn distribution with  $x = 5$ .

For non-Maxwellian plasmas,  $\alpha_{\gamma^+ \rightarrow i}^{(3)}(T_{\text{eff}})$  cannot be determined from  $q_{i \rightarrow \gamma^+}(T_{\text{eff}})$  as in the Maxwellian case (equation 3.62); a simplifying assumption must then be made if only total cross-sections are available. The method used here is to perform the integrals with respect to  $\varepsilon'$  and  $\varepsilon''$  using the Thomson differential cross-section, and introduce an  $\varepsilon$ -dependent correction factor,

$$g(\varepsilon) = \sigma_{i \rightarrow \gamma^+}(\varepsilon) / \sigma_{i \rightarrow \gamma^+}^{\text{Thomson}}(\varepsilon), \quad (3.64)$$

in the final integral over  $\varepsilon$ .

Similar arguments to those related to the excitation and de-excitation rates (section 3.2.1) follow for the quadratures here. Figure 3.19 shows the collisional ionisation rate coefficient from the  $1s2p^3P$  state of neutral helium, and figure 3.20 shows the equivalent three-body recombination rate coefficient.

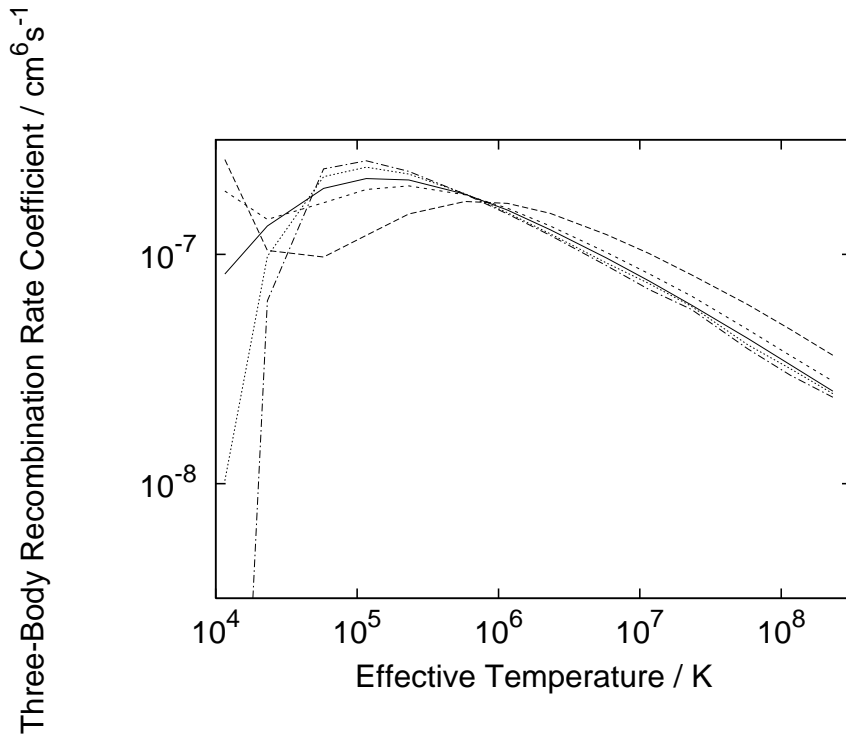


Figure 3.20: Three-body recombination rate coefficient to  $1s2p\ ^3P$  of neutral helium for various electron distribution functions. The quadrature is performed using a correction factor based on the Thomson cross-section. The solid curve shows a Maxwellian distribution; the long dashed curve, a  $\kappa$  distribution with  $\kappa = 2$ ; the short dashed curve, a  $\kappa$  distribution with  $\kappa = 5$ ; the dotted curve, a Druyvesteyn distribution with  $x = 2$ ; and the dot-dashed curve, a Druyvesteyn distribution with  $x = 5$ .

# Chapter 4

## Diagnostic Application

### 4.1 Methodology

The non-Maxwellian rate coefficients, as defined and calculated in section 3.2, may show deviation from their Maxwellian counterparts, but in order to analyse how the non-Maxwellian nature of the free electron distribution will affect the spectroscopically observable features of a plasma, one must utilise the rate coefficients within the GCR context of section 2.2. It is, thus, necessary to compute not only the equilibrium level populations, but also the effective coefficients for line emission, ionisation and recombination ‘driven’ by the various metastables of the different ionisation stages of an element. These effective coefficients are functions of electron temperature,  $T_e$ , and electron density,  $N_e$ , in the Maxwellian case, extending to a further dependence on a non-Maxwellian parameter (see section 3.1) in the present case.

From the discussions of chapter 2 it is noted that GCR modelling of a finite density plasma requires attention to very highly-excited states. This is of particular importance when dielectronic recombination is present due to the combined effect of stabilisation onto many such states. Modern calculations (Badnell *et al.* 2003) consider states with principal quantum number as high as 1000. Computationally, a collisional-radiative treatment of all levels as fully resolved is unattainable and not justified physically; the approach taken here is to define some critical principal quantum shell,  $n_c$ , and treat the levels either side of  $n_c$  separately and differently. Adequate modelling requires  $n_c$  to be high enough that all observed spectral lines are included in the lower lying levels, while diagnostic spectroscopy demands high precision rate coefficients for these transitions. The higher lying levels, those above  $n_c$ , require less precision in their rate coefficients and lower substate resolution and can be approximated as being in quasi-static

equilibrium with respect to the low level group in the collisional-radiative sense.

High quality cross-section data, as calculated by the methods of section 2.1, is held for the low-level group and the techniques of section 3.2 are used to create the appropriate non-Maxwellian rate coefficients. The high levels are treated using simpler analytic approximations for the various rate coefficients. The influence of these highly excited populations on the low levels is computed by the method of condensation and projection matrices (Summers *et al.* 2005). The high-level projection is thus approximated using a Maxwellian treatment at the effective temperature of the non-Maxwellian distribution used for the low levels. This simplification allows an economical focus on the primary effects of the non-Maxwellian distribution on spectral emission while retaining the GCR completeness, with only a small reduction in precision, but with the most substantial error for dielectronic recombination. This is because the summation over the high levels is a main contribution to the overall GCR effective recombination coefficient. State selective dielectronic recombination for the high levels in the non-Maxwellian case is allowed for by using the same conversion factor technique as for the low levels.

## 4.2 Computational Implementation

The mathematical description of non-Maxwellian rate coefficient calculations is outlined in detail in section 3.2, but it is useful to describe the implementation of these methods computationally. Figure 4.1 shows a schematic representation of the files and codes involved, the work being performed within the context of the ADAS project (Atomic Data and Analysis Structure; Summers, 1993, 2004).

The first stage of the modelling is to define the free-electron distribution function. As described in section 3.1.1, it is often the case that the distribution can be represented by an analytic formalism described by a non-Maxwellian parameter; allowed here, are the  $\kappa$  and Druyvesteyn distributions. Selection of such a distribution is simple, with an effective temperature and a value of the non-Maxwellian parameter (the  $\kappa$  of equation 3.4 or the  $x$  of equation 3.7) all that is required.

Should either of these analytic representations be inappropriate, and a numerically tabulated distribution function thus required, definition is less simple. Creation of the distribution function is the first requirement. Section 3.1.2 describes distribution functions as generated by Fokker-Planck and PIC codes, although the present work is by no means limited to such codes. Experimental measurements of distribution functions or analytic representations not covered

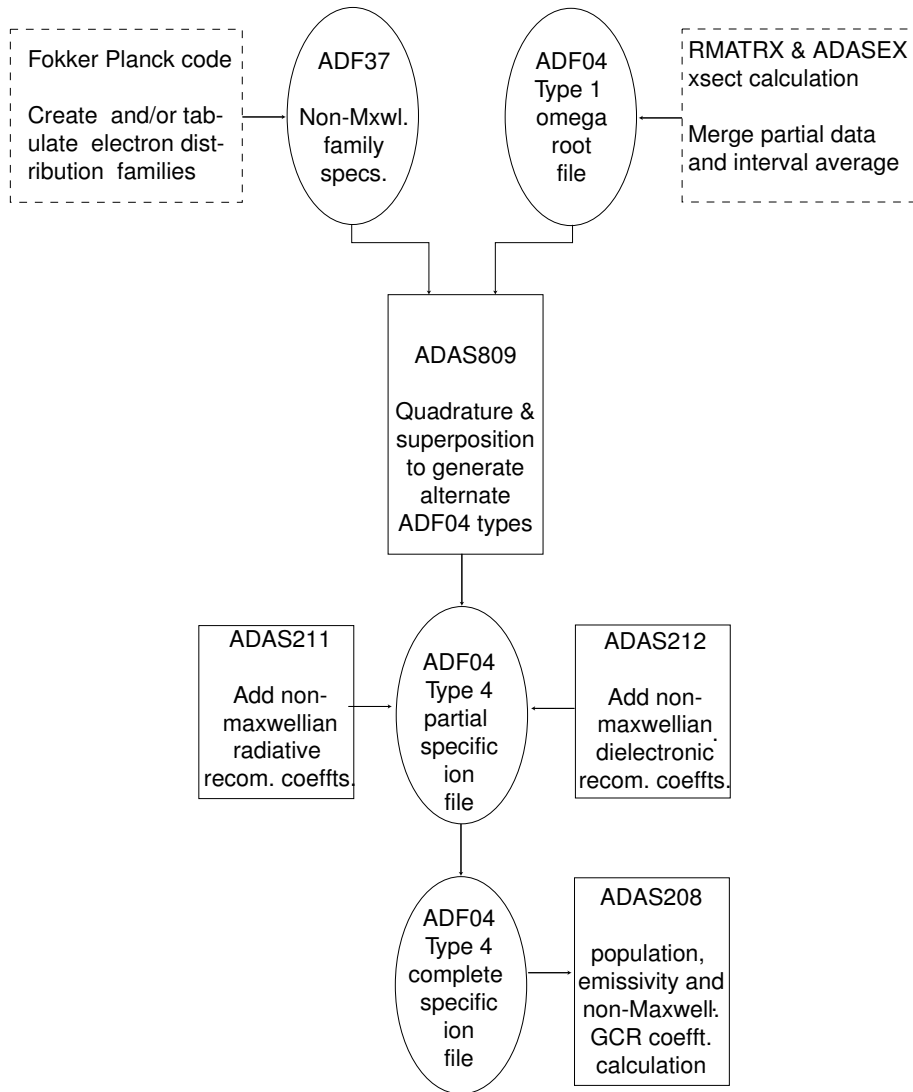


Figure 4.1: Flow chart showing the steps used to create distribution-averaged collision strengths and the subsequent calculations to produce the final populations, emissivities and GCR coefficients.

here can be tabulated and used as input to the processing. Methods of arriving at the distribution function lie outside the scope of ADAS, the file containing the tabulated distribution being the first level of involvement in terms of ADAS specification. The specific organisation of the distribution function files, assigned the ADAS format *adf37*, as well as the other file types mentioned here, can be found in Summers (2004).

Appertaining to the fundamental atomic data, the *adf04* data format has been used for many years in the ADAS project and has become one of the common formats for delivery of the results of fundamental electron-ion collision and atomic structure calculations. Prior to the present development, virtually all *adf04* files composed of Maxwell-averaged rate coefficients (held as  $\Upsilon$ ) given the sub-categorisation of *type 3*. These files cannot be applied to the non-Maxwellian case (see section 3.2.1), and the new *type 1* version is introduced, composed of cross-sections (held as collision strength,  $\Omega$ ). The latter are generally interval averaged (see Paton, 2005) for compactness (bearing in mind the arguments of section 2.1.1 concerning acceptability of scale length) but are unaveraged over a distribution function. *R*-matrix and associated structure codes (in particular, AUTOSTRUCTURE Badnell, 1986; Badnell and Pindzola, 1989; Badnell, 1997) are indicated as RMATRX in figure 4.1. Griffin *et al.* (1998) prepared a post-processing code, ADASEX, which assembled raw *R*-matrix outputs, executed Maxwell averaging and delivered a fully formed *adf04 - type 3* data set. ADASEX has been extended, with inclusion of interval averaging, so as to deliver an *adf04 - type 1* data set. The collisional data in this file type includes only electron impact excitation and ionisation.

The code ADAS809 converts from collision strengths, as held in *adf04 - type 1* files, to distribution-averaged collision strengths; section 3.2.1 describes the detail behind this. The common *adf04 - type 3* file type remains if the collision strength is averaged over a Maxwellian distribution, and a further class of *adf04* is introduced for non-Maxwell averaging, namely *type 4*. The organisation of *type 4* files adheres closely to that of *type 3* but must take account of the asymmetry introduced by the non-Maxwellian distribution; whereas *type 3* files hold the Maxwell-averaged  $\Upsilon$ , *type 4* files contain both  $\Upsilon$  and  $\mathcal{J}$  of the non-Maxwellian distribution. The specific analytic  $\kappa$  and Druyvesteyn families are internally generated within ADAS809, while true numerical distribution function families and superposition families are supplied in the data format *adf37*. ADAS809 will also convert from ionisation cross-sections to rate coefficients (see section 3.2.4); the ionisation data being held in *adf04* files in a similar manner to the excitation

data. Analogous to the separate parameters for excitation and de-excitation, there is a requirement for both ionisation and 3-body recombination reaction rate coefficients as one cannot be derived from the other in the non-Maxwellian case.

Additional collisional reactions must be added to the *adf04* file for complete GCR modelling. Extensions to existing codes ADAS211 and ADAS212 facilitate the inclusion of radiative recombination and dielectronic recombination. Quadratures over the free-bound Gaunt factor are performed within ADAS211 as described in section 3.2.2, and the conversion from Maxwellian dielectronic recombination to the non-Maxwellian equivalent via the methods of section 3.2.3 are performed within ADAS212. These rate coefficients are added to the existing *adf04* file to give a full *type 4* file for the ion in question.

Organisation of the *adf04 - type 4* file is such that each file contains data of a single ion for a single distribution function. Multiple runs using an assembly of *adf04* files is the usual procedure when investigating the influence of the degree of deviation from Maxwellian. Results of such an analysis can be found in section 4.3.

Generation of population structure, effective ionisation and recombination coefficients and line emissivities is carried out using ADAS208, with the procedures detailed in Summers *et al.* (2005). This code has been extended to recognise and pair the excitation/de-excitation and ionisation/recombination transitions from the *adf04 - type 4* data sets and process them as required. The influence of very high levels (above  $n_c$ ) is included by ADAS208 accessing preprepared projection matrices of ADAS format *adf17*. These matrices are the product of a separate collisional-radiative population calculation designed for many  $n$ -shells (called ADAS204) in the ADAS project. The projection matrices used here include the non-Maxwellian dielectronic recombination adjustment. The remainder of this chapter will discuss how such derived data can be used to diagnose non-Maxwellian plasmas.

## 4.3 Illustrative Results

Before application to actual experimental observations is performed, an investigation into the general use of non-Maxwellian distributions in predictive modelling and deductive spectral analysis is presented. For illustrative purposes, neutral helium is chosen to highlight the general principles, following from the rate coefficients generated in section 3.2.

Since the first order effect of a non-Maxwellian parameter is a mean energy shift, separation of a non-Maxwellian parameter from the effective temperature is expected to prove problematical when measuring line emission. This weak orthogonality is countered by the differential variation of dipole, non-dipole and spin change collision strengths with energy, and, as pointed out in section 3.2.1, the variation of the excitation and de-excitation rate coefficients with non-Maxwellian parameter is not proportional to the effective temperature. Figures 4.2(a) and 4.2(b) show the excited populations of neutral helium at an electron density of  $10^{12} \text{ cm}^{-3}$ . The differential variation of the collision strengths with energy is seen at this electron density in the relative populations of the terms. At the effective temperature of 3 eV, the fractional populations of some terms are increased and some decreased. This implies that some insight may be gained by the observation of transitions between these levels. Ratios of line intensities are thus examined as a function of non-Maxwellian parameter.

Diagnoses of electron density and temperature from a Maxwellian plasma from neutral helium use measurements of ratios of strong emission lines. Density is deduced from a measurement of a ratio of singlet to singlet transitions, generally  $(1s2p^1P - 1s3d^1D)/(1s2p^1P - 1s3s^1S)$  or  $(1s2p^1P - 1s3d^1D)/(1s2s^1S - 1s3p^1P)$ . These line ratios are considered a measure of the electron density due to collisional redistribution of the  $l$ -shell populations. Temperature is deduced from  $(1s2p^1P - 1s3s^1S)/(1s2p^3P - 1s3s^3S)$  or  $(1s2s^1S - 1s3p^1P)/(1s2s^3S - 1s3p^3P)$ . The singlet to singlet transition has an effective collision strength that tends to a constant with high-temperature, while the spin changing transition has an effective collision strength that reduces with temperature. This differential variation allows the ratio of these lines to be used a measure of electron temperature.

A similar technique is sought in which a non-Maxwellian parameter can be determined from a measurement of line ratios. For the  $\kappa$  distribution family, the following line ratios are examined:  $(1s2p^1P - 1s3s^1S)/(1s2s^1S - 1s3p^1P)$  and  $(1s2p^3P - 1s3d^3D)/(1s2s^1S - 1s3p^1P)$ . Figures 4.3(a) and 4.3(b) show, for a fixed electron density of  $10^{12} \text{ cm}^{-3}$ , contour plots of the line ratios as a function of effective electron temperature and  $\kappa$ . This is merely a demonstration of principle, and falls short of establishing a working diagnostic methodology for non-Maxwellians. The primary difficulty is that some insight into the distribution form is required before such an analysis can be fruitful.

The effect of the non-Maxwellian parameter on the collisional-radiative ionisation and recombination coefficients (see section 2.2) is shown in figures 4.4, 4.5, 4.6 and 4.7.

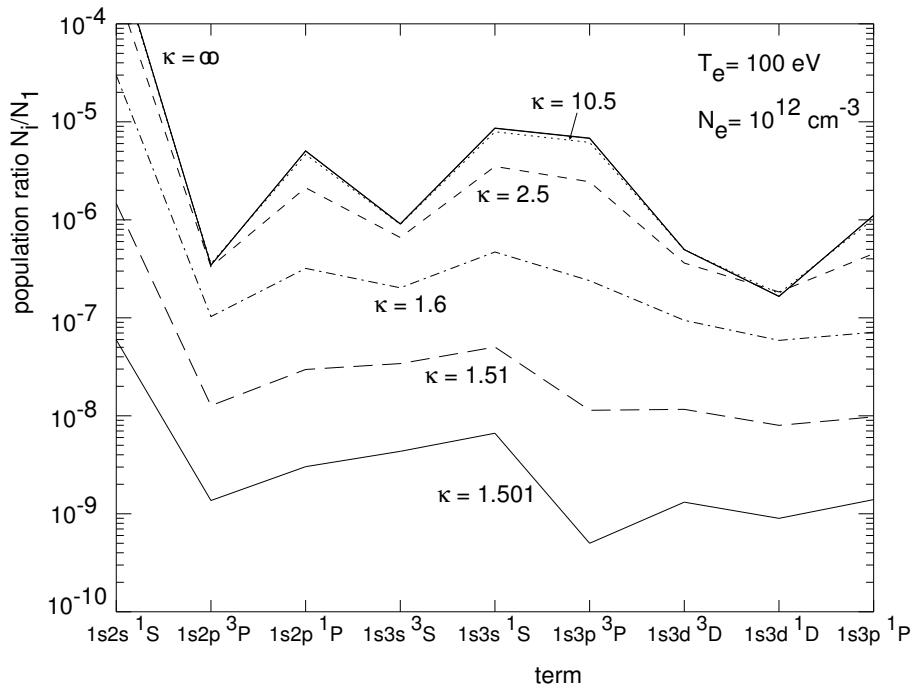
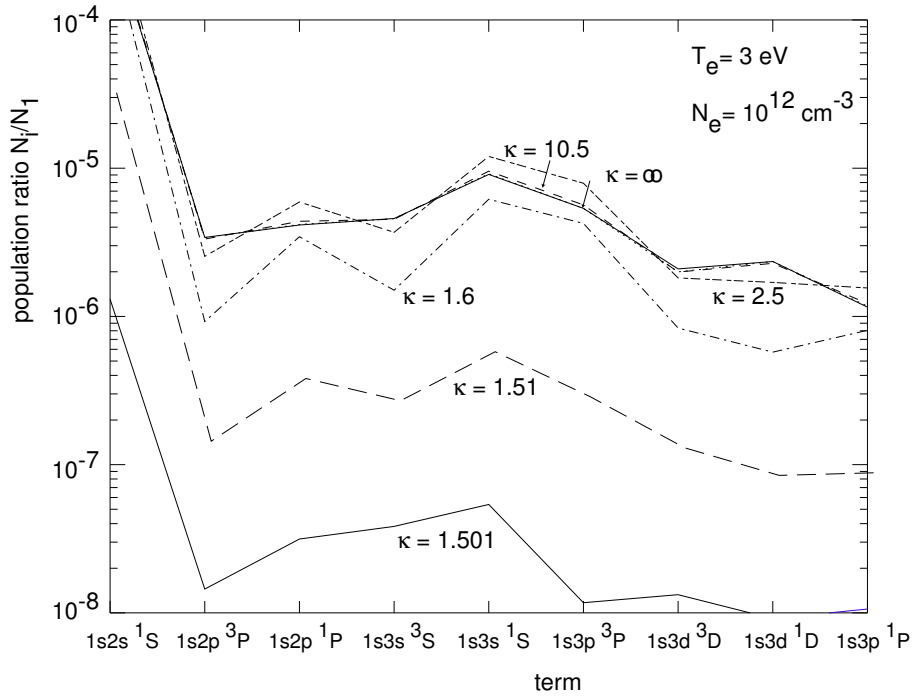


Figure 4.2: Variation of neutral helium populations with electron temperature and  $\kappa$ . Note that, at an electron temperature of 3 eV, some fractional populations are increased and some decreased. At the fixed electron density of  $10^{12} \text{ cm}^{-3}$ , there is only partial redistribution amongst the  $n = 3$   $l$ -substates.

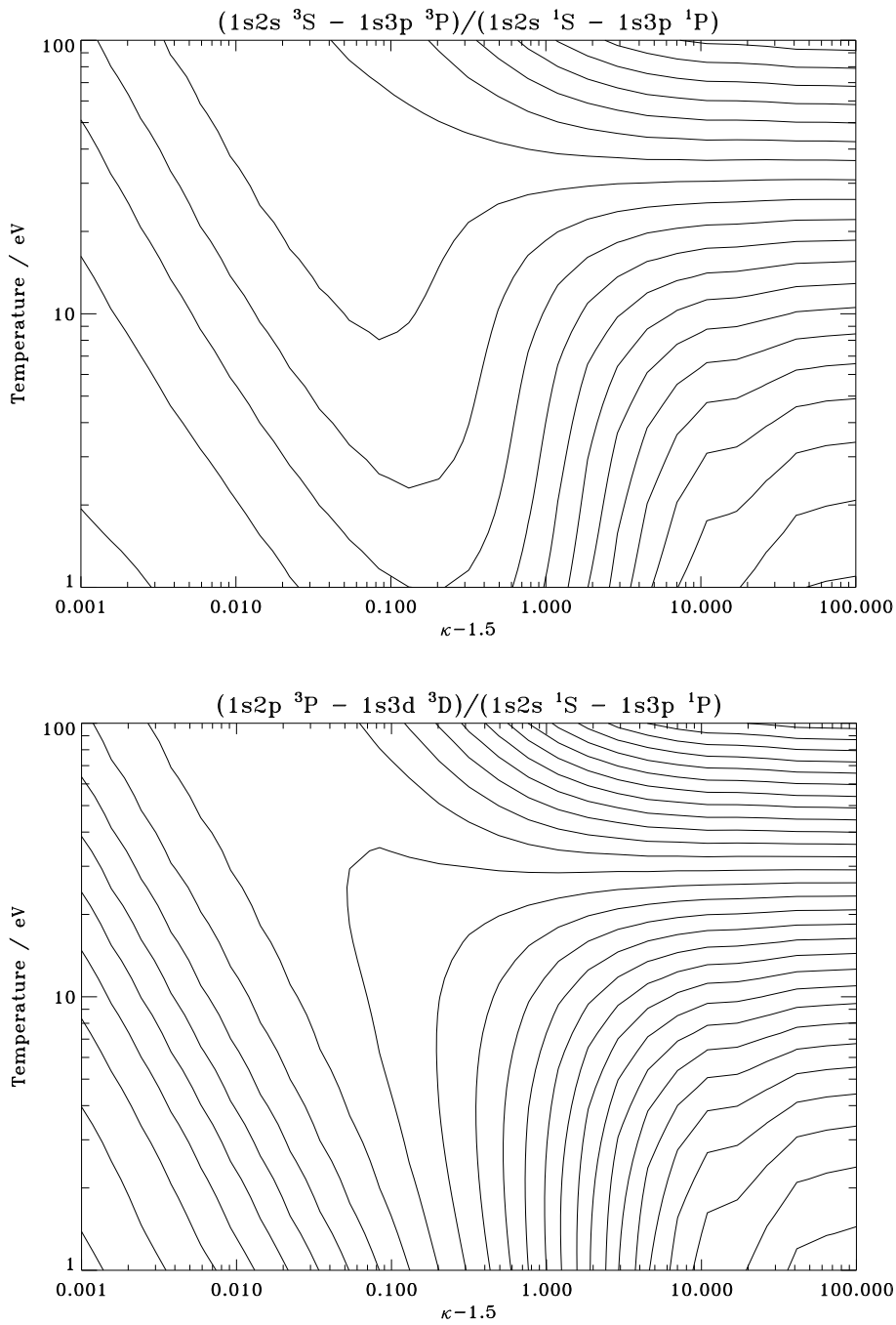


Figure 4.3: Neutral helium line ratios as a function of electron temperature and  $\kappa$  at a fixed electron density of  $10^{12} \text{ cm}^{-3}$ . (a)  $(1s2s^3S - 1s3p^3P)/(1s2s^1S - 1s3p^1P)$ . (b)  $(1s2p^3P - 1s3d^3D)/(1s2s^1S - 1s3p^1P)$ . The difference between the two surfaces indicate that  $T_{\text{eff}}$  and  $\kappa$  may be extracted from line ratio observations, although insight into the appropriate non-Maxwellian family is required.

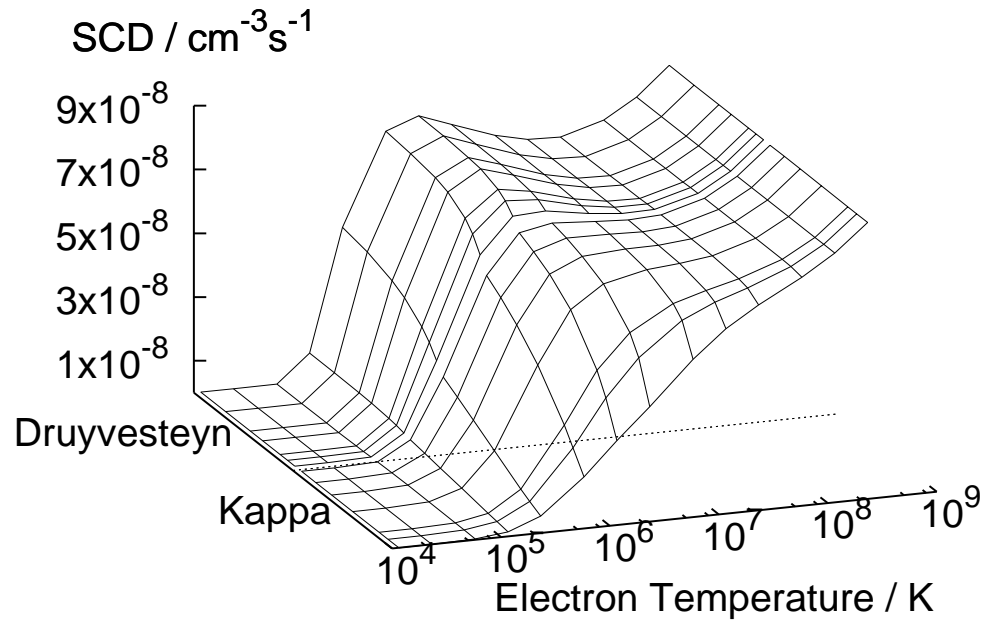


Figure 4.4: GCR ionisation coefficient for neutral helium at an electron density of  $10^9 \text{ cm}^{-3}$  as a function of non-Maxwellian parameter and electron temperature. The dotted line along the temperature axis indicates the Maxwellian, with Druyvesteyn and  $\kappa$  distributions deviating further from Maxwellian on moving away from this line. The Druyvesteyn distribution ranges from  $x = 1$  at the Maxwellian to  $x = 5$ , and the  $\kappa$  distribution ranges from  $\kappa \rightarrow \infty$  at the Maxwellian to  $\kappa = 1.6$ .

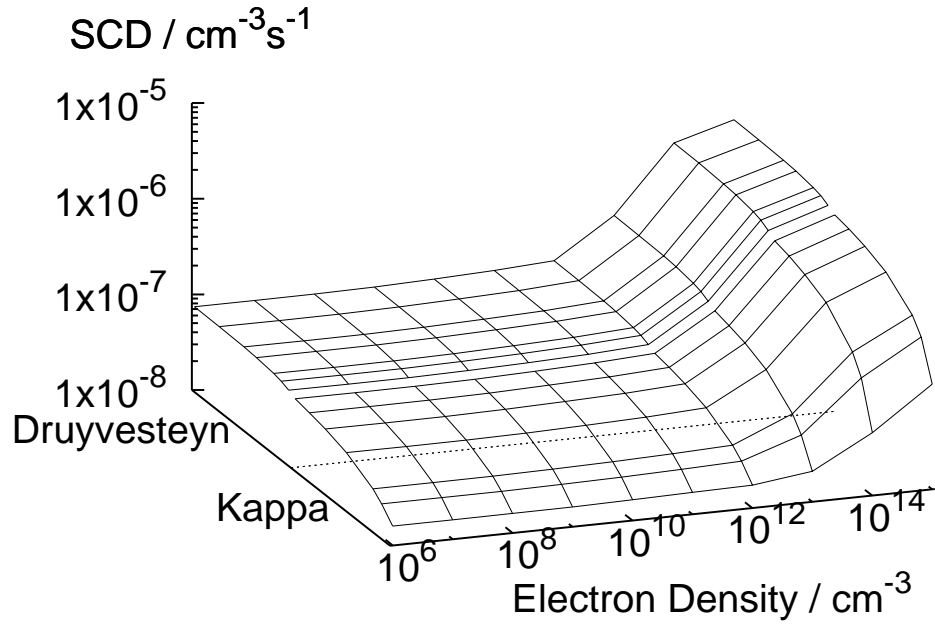


Figure 4.5: GCR ionisation coefficient for neutral helium at an electron temperature of  $10^6\text{K}$  as a function of non-Maxwellian parameter and electron density. The dotted line along the density axis indicates the Maxwellian, with Druyvesteyn and  $\kappa$  distributions deviating further from Maxwellian on moving away from this line. The Druyvesteyn distribution ranges from  $x = 1$  at the Maxwellian to  $x = 5$ , and the  $\kappa$  distribution ranges from  $\kappa \rightarrow \infty$  at the Maxwellian to  $\kappa = 1.6$ .

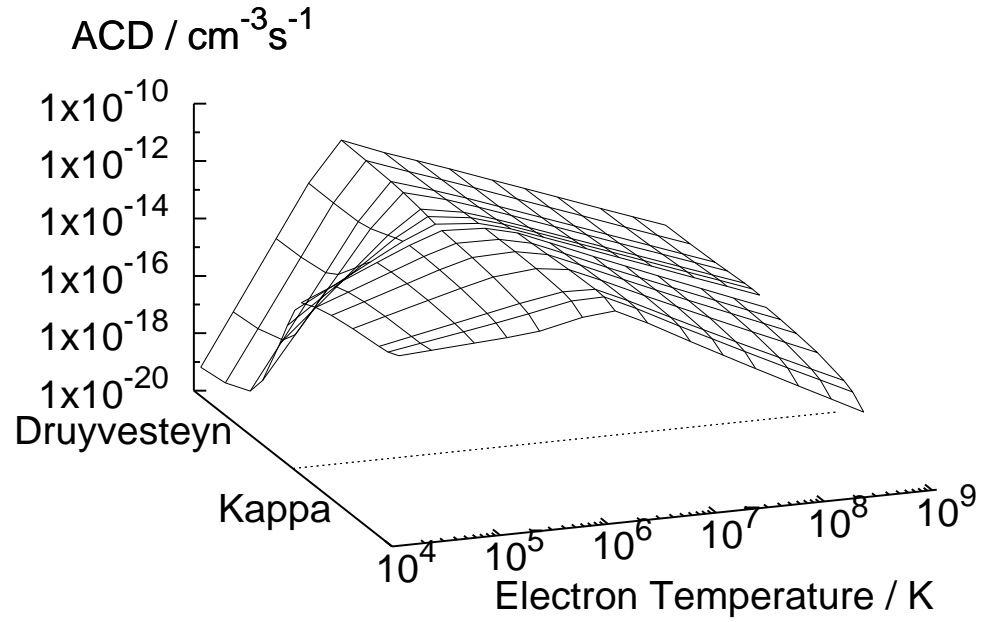


Figure 4.6: GCR recombination coefficient for neutral helium at an electron density of  $10^9 \text{ cm}^{-3}$  as a function of non-Maxwellian parameter and electron temperature. The dotted line along the temperature axis indicates the Maxwellian, with Druyvesteyn and  $\kappa$  distributions deviating further from Maxwellian on moving away from this line. The Druyvesteyn distribution ranges from  $x = 1$  at the Maxwellian to  $x = 5$ , and the  $\kappa$  distribution ranges from  $\kappa \rightarrow \infty$  at the Maxwellian to  $\kappa = 1.6$ .

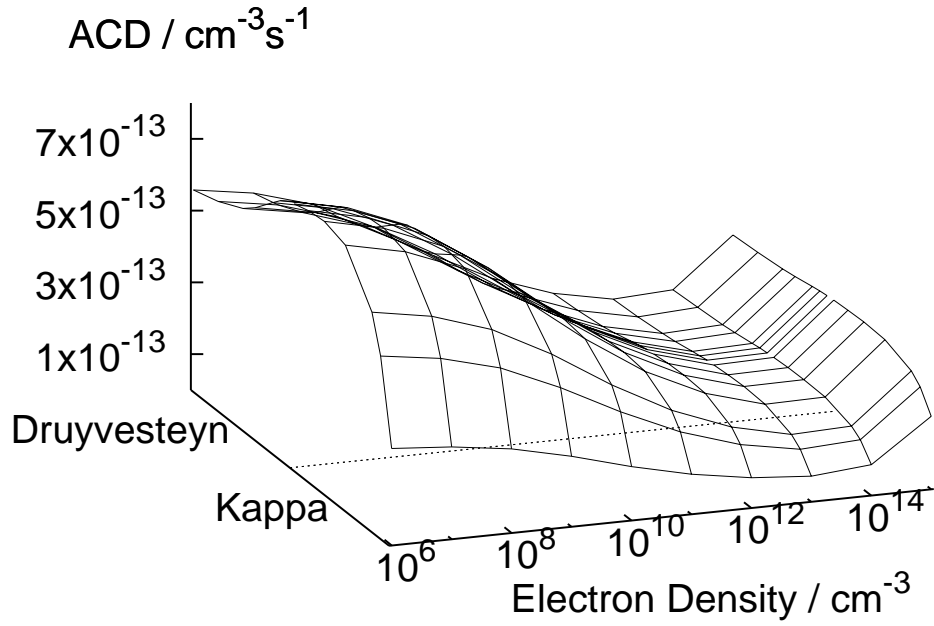


Figure 4.7: GCR recombination coefficient for neutral helium at an electron temperature of  $10^6$  K as a function of non-Maxwellian parameter and electron density. The dotted line along the density axis indicates the Maxwellian, with Druyvesteyn and  $\kappa$  distributions deviating further from Maxwellian on moving away from this line. The Druyvesteyn distribution ranges from  $x = 1$  at the Maxwellian to  $x = 5$ , and the  $\kappa$  distribution ranges from  $\kappa \rightarrow \infty$  at the Maxwellian to  $\kappa = 1.6$ .

The ionisation balance is sensitive to temperature and  $\kappa$  (as pointed out by Doyle *et al.* 2003), however, so unambiguous detection from ionisation state alone is particularly difficult. In addition to this, it is generally the case that electron impact ionisation coefficients are less accurate than excitation rate coefficients.

# Chapter 5

## Conclusions and Future Work

The effects of the free-electron energy distribution on the spectral emission of plasmas has been addressed, with consideration of the distribution functions and fundamental collisional cross-sections through to the observable line intensities.

The introduction of ‘families’ of distribution function (section 3.1) is an important concept in the diagnostic measurement of the non-Maxwellian character of a plasma. Figure 4.3 demonstrates that, by a measurement of line intensity ratios, a non-Maxwellian parameter can be discerned. Analysis of this kind, however, requires some prior insight into the nature of the distribution.

The vast majority of atomic modelling of plasmas considers only free-electrons of Maxwellian form, and atomic data have reflected this. For instance, electron-impact excitation data are usually provided in the form of Maxwell-averaged collision strengths, rather than the more general cross-sections (or collision strengths) which are required to produce non-Maxwellian reaction rates. This was thought necessary when disc space for storage was an issue and the large volume of cross-section data could be reduced in size by averaging over a Maxwellian distribution. This argument is less valid today, with the cost of computer storage rapidly decreasing. A further consequence of the tabulation of Maxwell-averaged collision strengths over cross-sections is that the data are not open to the same level of scrutiny; non-physical characteristics, such as the oscillations produced by the RMPS method (see figure 2.1), are lost to the smoothing process. Whatever the reason for the lack of tabulation of cross-sections in their elemental form, a proper examination of non-Maxwellian plasmas is only possible through their consideration.

These fundamental atomic data on electron-impact reactions demand attention; it is important that the data properly represent the resonant nature of the excitation, excitation-autoionisation and dielectronic recombination reactions. It

is demonstrated in figure 2.5 that a reduced tabulation of the excitation cross-section, which smooths through the resonance region, can be unsafe when quadrature of the cross-section with the electron distribution function is performed. While the reduced dataset is found to be compatible with quadrature over a Maxwellian, this is not so in the case of a  $\kappa$  distribution of equivalent effective temperature.

Following from these considerations, the thesis provides a complete framework for atomic modelling of non-Maxwellian plasmas from the fundamental electron-impact cross-section data to final spectral characteristics through a unified generalised collisional-radiative picture. The methods and computational implementation are general and suitable for any ion. The product of the computation is derived emission and GCR data appropriate both for plasma modelling and spectral analysis.

Perhaps the main reason for a lack of non-Maxwellian modelling of plasmas heretofore, is the difficulty in determining, unambiguously, the effects consequent of the electron distribution. Section 2.3 presents the results of an investigation into the spectral emission from dynamic regions of the solar atmosphere. It has been postulated (Doyle *et al.* 2003) that discrepant line intensities from UV explosive events can be the result of non-Maxwellian electron distributions. Section 2.3.2, however, demonstrates that the discrepancy between emission from Li- and Be-like ions can also be explained by consideration of the density dependence of the ionisation fractional abundance. It is clear that, particularly in the non-intrusive environment of astrophysics, it is not always possible to determine whether effects attributed to a non-Maxwellian distribution of free-electrons could not also have some other cause.

Nonetheless, taking the case of neutral helium as an example, and from a theoretical perspective, in section 4.3 of this thesis, it has been demonstrated that there is potential for the separation of effective temperature and non-Maxwellian parameter by the measurement of emission line ratios.

Application to actual experimental observations is beyond the scope of the thesis, but is the subject of planned future work. In the fusion regime, non-Maxwellian electrons occur in the core plasma as energised high-energy tails. More importantly for ITER (International Thermonuclear Experimental Reactor) and current large scale fusion machines is the expectation of non-Maxwellian behaviour in the divertor region. The output of this thesis is tuned for incorporation in the primary 1- and 2-dimensional transport models used for description of divertor and scrape-off-layers of tokamaks. Discrepancies between Langmuir

probe and spectral inferences of electron and ion temperature are expected to be the observable non-Maxwellian consequences.

As discussed earlier, spectral emission suggestive of non-Maxwellian behaviour is found in low-pressure arc and radio-frequency discharges in helium and in line ratios of helium observed from the solar atmosphere. These observations were one reason for using helium as a main vehicle for illustration in the non-Maxwellian GCR development. Both types of plasma have added complexity. The spectral emission by the laboratory discharges in helium are markedly influenced by the  $1s2s\ ^3S$  metastable population largely uncoupled from the ground population in the plasma. This additional free parameter makes the establishment of the non-Maxwellian character subtle. The derived data and models from this thesis are in use at Augsburg University in exploration of these effects.

Helium line formation and line ratios in the solar atmosphere are strongly affected by optical thickness in the resonance lines. This is a complex addition and necessitates incorporation of the non-Maxwellian effects in a multi-level radiative transfer and population model. Also, it might be expected that deviations from Maxwellian would decrease with increasing density at the deeper layers of the atmosphere. This is an important case for analysis using the methods and data of the thesis in light of the earlier studies of Smith (2003). Work is in progress on the solar atmosphere modelling in collaboration with Catania University and Observatory.

## References

- Anderson S W, Raymond J C and Ballegooijen A V 1996 *Astrophys. J.* **457** 939
- Armstrong T P, Paonessa M T, Bell E V and Krimigis S M 1983 *J. Geophys. Res.* **88** 8893
- Badnell N R 1986 *J. Phys. B: At. Mol. Phys.* **19** 3827
- Badnell N R 1997 *J. Phys. B: At. Mol. Opt. Phys.* **30** 1
- Badnell N R, O'Mullane M G, Summers H P, Altun Z, Bautista M A, Colgan J, Gorczyca T W, Mitnik D M, Pindzola M S and Zatsarinny O 2003 *Astronomy and Astrophysics* **406** 1151
- Badnell N R and Pindzola M S 1989 *Phys. Rev. A* **39** 1685
- Ballance C P 2003 private communication
- Bame S J, McComas D J, Barraclough B L, Phillips J L, Sofaly K J, Chavez J C, Goldstein B E and Sakurai R K 1992 *Astron. Astrophys. Suppl. Ser.* **92** 237
- Bar-Shalom A, Klapisch M and Oreg J 1988 *Phys. Rev. A* **38** 1773
- Bartschat K, Hudson E T, Scott M P, Burke P G and Burke V M 1996 *J. Phys. B: At. Mol. Opt. Phys.* **29** 115
- Bates D R, Kingston A E and McWhirter R W P 1962 *Proc. Roy. Soc.* **A267** 297
- Behringer K and Fantz U 1994 *J. Phys. D: Appl. Phys.* **27** 2128
- Behringer K and Fantz U 2000 *New J. Phys.* **2** 23
- Bethe H 1930 *Ann. Phys. Lpz* **5** 325
- Bingham R, Bryant D A and Hall D S 1984 *Geophys. Res. Lett.* **11** 327
- Bingham R, Bryant D A and Hall D S 1988 *Ann. Geophys.* **6** 159
- Bingham R, Dawson J M, Shapiro V D, Mendis D A and Kellett B J 1997 *Science* **275** 49
- Bingham R, Kellett B J, Bryans P, Summers H P, Torney M, Shapiro V D, Spicer D S and O'Brien M 2004 *Astrophys. J.* **601** 896

- Birdsall C K and Langdon A B 1985 *Plasma Physics via Computer Simulation* (New York, McGraw-Hill)
- Bleeker J A M, Willingale R, van der Hayden K, Dennerl K, Kaastra J S, Aschenbach B and Vink J 2001 *Astronomy and Astrophysics* **365** L225
- Bray I 2002 *Phys. Rev. Lett.* **89** 273201
- Bray I and Stelbovics A T 1993 *Phys. Rev. Lett.* **70** 746
- Browning P K 1991 *Plasma Phys. Control. Fusion* **33** 539
- Brueckner G E and Bartoe J-D F 1983 *Astrophys. J.* **272** 329
- Bryans P, Quest K B, Shapiro V D, Bingham R and Torney M 2003 *American Physical Society, 45th Annual Meeting of the Division of Plasma Physics, Albuquerque, New Mexico* DPP03 GP1.136APS
- Bryant D A 1992 *Ann. Geophys.* **10** 333
- Bryant D A 1996 *J. Plasma Physics* **56** 87
- Bryant D A, Hall D S and Bingham R 1991 *Auroral Physics* ed. Meng C-I, Rycroft M J and Frank L A (Cambridge University Press, New York) 119
- Burgess A 1964 *Proc. Symp. Atomic Collision Processes in Plasmas*, Culham AERE Rep. **4818** 63
- Burgess A and Chidichimo M C 1983 *Mon. Not. R. Astron. Soc.* **203** 1269
- Burgess A and Summers H P 1969 *Astrophys. J.* **157** 1007
- Burgess A and Summers H P 1976 *Mon. Not. R. Astron. Soc.* **174** 345
- Burgess A and Summers H P 1987 *Mon. Not. R. Astron. Soc.* **226** 257
- Burgess A, Summers H P, Cochrane D M and McWhirter R W P 1977 *Mon. Not. R. Astron. Soc.* **179** 275
- Burgess A and Tully J A 1978 *J. Phys. B: At. Mol. Phys.* **11** 4271
- Burgess A and Tully J A 1992 *Astronomy and Astrophysics* **254** 436
- Burke P G and Robb W D 1975 *Adv. At. Mol. Phys.* **11** 143
- Busnardo-Neto J, Pritchett P L, Lin A T and Dawson J M 1977 *J. Compt. Phys.* **23** 300

- Capitelli M, Gorse C and Longo S 1993 *Microwave Discharges, Fundamentals and Applications, NATO ASI Series B: Physics* ed. Ferreira C M and Moisan M **302** 379
- Chae J, Wang H, Lee C Y, Goode P R and Schühle U 1998 *Astrophys. J.* **497** L109
- Christon S P, Mitchell D G, Williams D J, Frank L A, Huang C Y and Eastman T E 1988 *J. Geophys. Res.* **93** 2562
- Cloutier P A, Kramer L and Taylor H A Jr 1993 *Geophys. Res. Lett.* **20** 2731
- Colgan J, Loch S D, Pindzola M S, Ballance C P and Giffin D C 2003 *Phys. Rev. A* **68** 032712
- Colgan J, Pindzola M S, Mitnik D M, Griffin D C and Bray I 2001 *Phys. Rev. Lett.* **87** 213201
- Cowan R D 1981 *The Theory of Atomic Structure and Spectra* (Berkeley: University of California Press)
- Cravens T E 1997 *Geophys. Res. Lett.* **24** 1105
- Darwin C G 1920 *Phil. Mag.* **39** 446
- Dawson J M 1962 *Phys. Fluids* **5** 445
- Dawson J M, Bingham R and Shapiro V D 1997 *Plasma Phys. Control. Fusion* **39** A185
- Del Zanna G, Landini M and Mason H E 2002 *Astronomy and Astrophysics* **385** 968
- Dendy R O, Harvey B M, O'Brien M and Bingham R 1995 *J. Geophys. Res.* **100** 21973
- Dennerl K 2002 *Astronomy and Astrophysics* **394** 1119
- Dennerl K, Burwitz V, Englhauser J, Lisse C and Wolk S 2002 *Astronomy and Astrophysics* **386** 319
- Dere K P 1994 *Adv. Space Res.* **14** 13
- Dere K P, Bartoe J-D F and Brueckner G E 1989 *Solar Phys.* **123** 41

- Dobé Z, Quest K B, Shapiro V D, Szegő K and Huba J D 1999 *Phys. Rev. Lett.* **83** 260
- Dolder K T and Peart B 1976 *Rep. Prog. Phys.* **39** 1278
- Domingo V, Fleck B and Poland A I 1995 *Solar Phys.* **162** 1
- Doyle J G, Ishak B, Ugarte-Urra I, Bryans P and Summers H P 2005a *Astronomy and Astrophysics* submitted
- Doyle J G, Dzifčáková E and Madjarska M S 2003 *Solar Phys.* **218** 79
- Doyle J G and Raymond J C 1984 *Solar Phys.* **90** 97
- Doyle J G, Summers H P and Bryans P 2005b *Astronomy and Astrophysics* **430** L29
- Druyvesteyn M J 1930 *Physica* **10** 61
- Dubinin E M, Sauer K, Baumgärtel K and Lundin R 1997 *Adv. Space Res.* **20** 149
- Dzifčáková E 1992 *Solar Phys.* **140** 247
- Dzifčáková E 2002 *Solar Phys.* **208** 91
- Dzifčáková E and Kulinová A 2003 *Solar Phys.* **218** 41
- Falk R A, Stefani G, Camilloni R, Dunn G H, Phaneuf R A, Gregory D C and Crandall D H 1983 *Phys. Rev. A* **28** 91
- Fisch N J 1978 *Phys. Rev. Lett.* **41** 873
- Fisch N J and Boozer A H 1980 *Phys. Rev. Lett.* **45** 720
- Fogle M, Eklow N, Lindroth E, Mohamed T, Schuch R and Tokman M 2003 *J. Phys. B: At. Mol. Opt. Phys.* **36** 2563
- Goett S J and Sampson D H 1983 *Atomic Data and Nucl. Data Tables* **29** 535
- Gorczyca T W and Badnell N R 1997 *J. Phys. B: At. Mol. Opt. Phys.* **30** 3897
- Gu M F 2003 *Astrophys. J.* **582** 1241
- Gudmundsson J T 2001 *Plasma Sources Sci. Technol.* **10** 76

- Gudmundsson J T, Kimura T and Leiberman M A 1999 *Plasma Sources Sci. Technol.* **8** 22
- Gudmundsson J T, Marakhtanov A M Patel K K, Gopinath V P and Leiberman M A 2000 *J. Phys. D: Appl. Phys.* **33** 1323
- Griffin D C, Badnell N R and Pindzola M S 1998 *J. Phys. B: At. Mol. Opt. Phys.* **31** 3713
- Gringauz K I and Verigin M I 1990 *Comet Halley: Investigations, Results, Interpretations. Vol. 1 - Organization, Plasma, Gas.* ed. Mason J W (New Jersey: Ellis Horwood/Prentice-Hall) p. 147
- Häberli R M, Gombosi T I, de Zeeuw D L, Combi M R and Powell K G 1997 *Science* **276** 939
- Haefl A V 1949 *Proceedings of IRE* **37** 4
- Hamdan M, Birkinshaw K and Hasted J B 1978 *J. Phys. B: At. Mol. Phys.* **11** 331
- Handy B N, Acton L W, Kankelborg C C, Wolfson C J, Akin D J, Bruner M E, Carvalho R, Catura R C, Chevalier R, Duncan D W, Edwards C G, Feinstein C N, Freeland S L, Friedlaender F M, Hoffmann C H, Hurlburt N E, Jurcevich B K, Katz N L, Kelly G A, Lemen J R, Levay M, Lindgren R W, Mathur D P, Meyer S B, Morrison S J, Morrison M D, Nightingale R W, Pope T P, Rehse R A, Schrijver C J, Shine R A, Shing L, Strong K T, Tarbell T D, Title A M, Torgerson D D, Golub L, Bookbinder J A, Caldwell D, Cheimets P N, Davis W N, Deluca E E, McMullen R A, Warren H P, Amato D, Fisher R, Maldonado H, Parkinson C 1999 *Solar Phys.* **187** 229
- Harrison M F A 1968 *Methods in Experimental Physics* ed. Fite W F and Bederson B (Academic, New York) **7a** 95
- Harrison R A, Sawyer E C, Carter M K, Cruise A M, Cutler R M, Fludra A, Hayes R W, Kent B J, Lang J, Parker D J, Payne J, Pike C D, Peskett S C, Richards A G, Culhane J L, Norman K, Breeveld A A, Breeveld E R, Janabi K F Al, McCalden A J, Parkinson J H, Self D G, Thomas P D, Poland A I, Thomas R J, Thompson W T, Kjeldseth-Moe O, Brekke P, Karud J, Maltby P, Aschenbach B, Brauningner H, Kuhne M, Hollandt J, Siegmund O H W, Huber M C E, Gabriel A H, Mason H E and Bromage B J I 1995 *Solar Phys.* **162**, 233

- Hartnagel H 1964 *Proc. Inst. Elec. Eng.* **111** 1821
- Hartnagel H 1965 *Int. J. Electron.* **18** 43148
- Hartnagel H 1966 *Int. J. Electron.* **21** 277
- Hasted J B and Awad G L 1972 *J. Phys. B: At. Mol. Phys.* **5** 1719
- Hasegawa A, Mima K and Duong-van M 1985 *Phys. Rev. Lett.* **54** 2608
- Hebb M H and Menzel D H 1940 *Astrophys. J.* **92** 408
- Hewett D W 1985 *Space Sci. Rev.* **42** 29
- Hewett D W and Nielson 1978 *J. Compt. Phys.* **29** 219
- Hockney R W 1965 *J. Assoc. Compt. Mach.* **12** 95
- Hockney R W 1966 *Phys. Fluids* **9** 1826
- Hoshino M, Arons J, Gallant Y A and Langdon A B 1992 *Astrophys. J.* **390** 454
- Innes D E, Brekke P, Germerott D and Wilhelm K 1997 *Solar Phys.* **175** 341
- Kaufman A N and Rostler P S 1971 *Phys. Fluids* **14** 446
- Krasnopolsky V A 1975 *Icarus* **24** 28
- Laming J M 2001 *Astrophys. J.* **563** 828
- Landi E and Landini M 1999 *Astronomy and Astrophysics* **347** 401
- Lanzafame A C, Brooks D H, Lang J, Summers H P, Thomas R J and Thompson A M 2002 *Astronomy and Astrophysics* **384** 242
- Leubner M P 1982 *J. Geophys. Res.* **87** 6335
- Leubner M P 2001 *Phys. Chem. Earth* **26** 61
- Linkemann J, Müller A, Kenntner J, Habs D, Schwalm D, Wolf A, Badnell N R and Pindzola M S 1995 *Phys. Rev. Lett.* **74** 21
- Loch S D, Pindzola M S, Ballance C P, Griffin D C, Mitnik D M, Badnell N R, O'Mullane M G, Summers H P and Whiteford A D 2002 *Phys. Rev. A* **66** 052708
- Loch S D, Witthoeft M, Pindzola M S, Bray I, Fursa D V, Fogle M, Schuch R, Glans P, Ballance C P and Griffin D C 2005 *Phys. Rev. A* **71** 012716

- Lotz W 1968 *Z. Phys.* **216** 241
- Loureiro J and Ferreira C M 1986 *J. Phys. D: Appl. Phys.* **19** 17
- Loureiro J and Ferreira C M 1989 *J. Phys. D: Appl. Phys.* **22** 67
- Lui A T Y and Krimigis S M 1981 *Geophys. Res. Lett.* **8** 527
- MacNeice P, Fontenla J and Ljepojevic N N 1991 *Astrophys. J.* **369** 544
- Madjarska M S and Doyle J G 2002 *Astronomy and Astrophysics* **382** 319
- Maksimovic M, Pierrard V and Riley P 1997 *Geophys. Res. Lett.* **24** 1151
- McBride J B, Ott E, Boris J P and Orens J H 1972 *Phys. Fluids* **15** 2367
- Menzel D H and Pekeris C L 1935 *Mon. Not. R. Astron. Soc.* **96** 77
- Merts A L, Mann J B, Robb W D and Magee N H Jr 1980 *Los Alamos Report* LA-8267-MS
- Mihalas D and Stone M E 1968 *Astrophys. J.* **151** 293
- Moisan M, Barbeau C, Claude R, Ferreira C M, Margot J, Paraszczak J, Sá A B, Sauv  G and Wertheimer M R 1991 *J. Vac. Sci. Technol. B* **9** 8
- Moses D and Cook J W 1994 *Space Sci. Rev.* **70** 81
- Mott N F and Massey H S W 1949 *The Theory of Atomic Collisions* 2nd ed. (Oxford, Clarendon Press)
- Mozer F S, Cattell C A, Hudson M K, Lysak R L, Temerin M and Torbet R B 1980 *Space Sci. Rev.* **27** 155
- M ller A, Teng H, Hofmann G, Phaneuf R A and Salzborn E 2000 *Phys. Rev. A* **62** 062720
- Narain U and Ulmschneider P 1990 *Space Sci. Rev.* **54** 377
- Neilson C W and Lewis H R 1976 *Methods in Computational Physics* (Academic Press, New York) **16** 367
- Nighan W 1970 *Phys. Rev. A* **2** 1989
- Ochkur V I 1964 *Sov. Phys. JETP* **18** 503
- Owocki S P and Scudder J D 1983 *Astrophys. J.* **270** 758

- Paton I D 2005 *On Neutral Helium for Diagnostic Application*, PhD Thesis, University of Strathclyde
- Pérez M E, Doyle J G, Erdélyi R and Sarro L M 1999 *Astronomy and Astrophysics* **342** 279
- Pierce J R 1948 *J. Appl. Phys.* **19** 231
- Pindzola M S, Badnell N R and Griffin D C 1992 *Phys. Rev. A* **46** 5725
- Pindzola M S, Griffin D C, and Bottcher C 1986a *Atomic Processes in Electron-Ion and Ion-Ion Collisions*, NATO Advanced Study Institute, Series B: **145** Physics, ed Brouillard (Plenum, New York) 75
- Pindzola M S, Griffin D C, and Bottcher C 1986b *Phys. Rev. A* **33** 3787
- Pindzola M S and Robicheaux F 1996 *Phys. Rev. A* **54** 2142
- Porter L J, Klimchuk J A and Sturrock P A 1994a *Astrophys. J.* **435** 482
- Porter L J, Klimchuk J A and Sturrock P A 1994b *Astrophys. J.* **435** 502
- Pottelette R, Treumann R A and Dubouloz N 1992 *J. Geophys. Res.* **97** 12029
- Quest K B, Shapiro V D, Szegő K and Dobé Z 1997 *Geophys. Res. Lett.* **24** 301
- Raymond J C and Doyle J G 1981 *Astrophys. J.* **245** 1141
- Retterer J M, Chang T and Jasperse J R 1986 *J. Geophys. Res.* **91** 1609
- Richtmyer R D and Morton K W 1967 *Difference Methods for Initial-Value Problems* (Interscience)
- Ryutova M P and Tarbell T D 2000 *Astrophys. J.* **541** L29
- Sagdeev R Z, Shapiro V D, Shevchenko V I, Zacharov A, Kiraly P, Szegő K, Nagy A F and Grard R S L 1990 *Geophys. Res. Lett.* **17** 893
- Sagdeev R Z and Zakharov A V 1989 *Nature* **341** 581
- Sampson D H 1986 *Phys. Rev. A* **34** 986
- Sampson D H, Goett S J, Petrou G V, Zhang H and Clark R E H 1985a *Atomic Data and Nucl. Data Tables* **32** 343
- Sampson D H, Petrou G V, Goett S J and Clark R E H 1985b *Atomic Data and Nucl. Data Tables* **32** 403

- Scherrer P H, Bogart R S, Bush R I, Hoeksema J T, Kosovichev A G, Schou J, Rosenberg W, Springer L, Tarbell T D, Title A, Wolfson C J, Zayer I and MDI Engineering Team 1995 *Solar Phys.* **162** 129
- Schweitzer J, Brandenburg R, Bray I, Hoekstra R, Autmayr F, Janev R K and Winter H P 1999 *Atomic Data and Nucl. Data Tables* **72** 239
- Scudder J D 1992a *Astrophys. J.* **398** 299
- Scudder J D 1992b *Astrophys. J.* **398** 319
- Scudder J D 1994 *Astrophys. J.* **427** 446
- Shapiro V D, Bingham R, Dawson J M, Dobé Z, Kellett B J and Mendis D A 1998 *Physica Scripta* **T75** 39
- Shapiro V D, Bingham R, Dawson J M, Dobé Z, Kellett B J and Mendis D A 1999 *J. Geophys. Res.* **104** 2537
- Shapiro V D, Szegő K, Ride S K, Nagy A F and Shevchenko V I 1995 *J. Geophys. Res.* **100** 21289
- Smith G R 2003 *Mon. Not. R. Astron. Soc.* **341** 143
- Spenner K, Knudsen W C and Lotze W 1995 *J. Geophys. Res.* **100** 14499
- Spenner K, Knudsen W C, Miller K L, Novak V, Russell C T and Elphic R C 1980 *J. Geophys. Res.* **85** 7655
- Spicer D S, Clark R W and Maran S P 1990 *Astrophys. J.* **356** 549
- Spitzer L Jr 1956 *Physics of Fully Ionized Gases* Interscience Publishers
- Summers H P 1993 *JET Joint Undertaking Report* JET-IR(93)07
- Summers H P 2004 *The ADAS User Manual, version 2.6*  
<http://adas.phys.strath.ac.uk>
- Summers H P, Dickson W J, O'Mullane M G, Badnell N R, Whiteford A D, Brooks D H, Lang J, Loch S D and Griffin D C 2005 *Plasma Phys. Control. Fusion* submitted
- Summers H P and Hooper M B 1983 *Plasma Physics* **25** 1311
- Szegő K, Dobé Z, Knudsen W C, Nagy A F and Shapiro V D 1997 *J. Geophys. Res.* **102** 2175

- Teriaca L, Banerjee D, Falchi A, Doyle J G and Madjarska M S 2004 *Astronomy and Astrophysics* **427** 1065
- Teriaca L, Madjarska M S and Doyle J G 2001 *Solar Phys.* **200** 91
- Thomas V and Birdsall C K 1980 *Proc. Ninth Conf. Num. Sim. Plasmas* Northwestern Univ., Evanston, Illinois, PB6
- Thomson J J 1912 *Phil. Mag.* **23** 449
- Tu C-Y and Marsch E 1997 *Solar Phys.* **171** 363
- Vasyliunas V M 1968 *J. Geophys. Res.* **73** 2839
- Vernazza J E and Raymond J C 1979 *Astrophys. J.* **228** L89
- Viñas A F, Wong H K and Klimas A J 2000 *Astrophys. J.* **528** 509
- Wegmann R, Schmidt H U, Lisse C M, Dennerl K and Englhauser J 1998 *Planet. Space Sci.* **46** 603
- Wilhelm K, Curdt W, Marsch E, Schuhle U, Lemaire P, Gabriel A, Vial J-C, Grewing M, Huber M C E, Jordan S D, Poland A I, Thomas R J, Kuhne M, Timothy J G, Hassler D M and Siegmund O H W 1995 *Solar Phys.* **162** 189
- Williams D J, Mitchell D G and Christon S P 1988 *Geophys. Res. Lett.* **15** 303
- Winkler B 1993 *Microwave Discharges, Fundamentals and Applications, NATO ASI Series B: Physics* ed. Ferreira C M and Moisan M **302** 339
- Winkler B and Pfau S 1973 *Beitr. Plasmaphys.* **5** 273
- Whiteford A D, Badnell N R, Ballance C P, Loch S D, O'Mullane M G and Summers H P 2002 *J. Phys. B: At. Mol. Opt. Phys.* **35** 3729
- Woodruff P R, Hublet M-C, Harrison M F A and Brook E 1978 *J. Phys. B: At. Mol. Phys.* **11** 679
- Young P R, Del Zanna G, Landi E, Dere K P, Mason H E and Landini M 2003 *Astrophys. J. Suppl. Ser.* **144** 135
- Yu S P, Kooyers G P and Buuneman O 1965 *J. Appl. Phys.* **36** 2550
- Zhang H L, Sampson D H and Clark R E H 1986 *Phys. Rev. A* **35** 267

Zhang H L, Sampson D H and Fontes C J 1990 *Atomic Data and Nucl. Data Tables* **44** 31

Zirker J B 1993 *Solar Phys.* **148** 43